NORTHWESTERN UNIVERSITY

Characterizing and Modeling Transient Photoconductivity in Amorphous In-Ga-Zn-O Thin Films

A DISSERTATION

SUBMITTED TO THE GRADUATE SCHOOL
IN PARTIAL FULFILLMENT OF THE REQUIREMENTS

for the degree

DOCTOR OF PHILOSOPHY

Field of Electrical Engineering

By

Jiajun Luo

EVANSTON, ILLINOIS

December 2016

ABSTRACT

Characterizing and Modeling Transient Photoconductivity
in Amorphous In-Ga-Zn-O Thin Films

Jiajun Luo

Amorphous In-Ga-Zn-O (a-IGZO) and other amorphous oxide semiconductors are attracting increasing attention from the display industry for their high electron mobility, ease of large-area manufacture, and potential for future flexible electronics. However, such amorphous materials often show instability under gate voltage bias, temperature, and illumination stress, with extremely slow relaxation times. Previous research has focused on empirical solutions to the instability problem, such as laser-assisted annealing and passivation to reduce device degradation. But a complete characterization of the degradation process is still lacking, and understanding of the underlying physical mechanism is still limited.

This work focuses on the transient photoresponse of a-IGZO thin films. By measuring the basic electrical properties of the thin films under photo-excitation and dark relaxation, it is confirmed that the conductivity photoresponse is mostly due to the creation and trapping of free electrons, while electron mobility remains mostly constant. However,

transient photoresponse in a-IGZO does not follow the simple exponential behavior typically observed crystalline materials. It shows a faster transient at short time scales and slower transient at long time scales comparing to a simple exponential response.

Proper characterization of such a photoresponse requires improvements to the conventional van der Pauw and Hall measurement methods. To make fast and accurate Hall measurements, a heterodyne Hall method is developed using simple analog signal processing. This method not only enables continuous measurement of the carrier density transient at a single magnetic field, but also extends the lowest mobility that can be measured by Hall effects. For the non-exponential photoresponse in a-IGZO with fast initial transient and extremely slow long-term transient, a modulated time-division multiplexing apparatus is also introduced to measure several samples in parallel while capturing the initial transients in all samples with high time-resolution.

While many previous reports analyzed non-exponential transients by assuming the transients to follow certain function forms, this work introduces a distributed time constant analysis that can be applied to any relaxation response. By transferring the transient response as a function of log-scale time, any relaxation response can be represented as the convolution of a time constant distribution. Therefore, the minimum measurement duration to correctly characterize the response is identified as the inflection point on a semi-log plot versus log-scale time. With the visual features on the semi-log plot, a method to estimate the entire distribution spectrum is also introduced. This allows reasonable estimation of the asymptotic response value, which cannot be directly measured in systems involving large time constants.

In the a-IGZO system, the transient photoresponse fits best to a stretched exponential function. This work discusses the applications and properties of the stretched exponential function. Two contrasting physical explanations to the stretched exponential behavior, the distributed activation energy model and the continuous-time random walk model, are discussed. While the distributed activation energy model fails to explain why an asymmetric activation energy distribution appears universally in many distinct systems, the continuous-time random walk model explains the stretched exponential behavior as arising from an exponential tail of activation energies, which fits the disordered nature of amorphous materials. Based on the continuous-time random walk model, a microscopic photoresponse mechanism compatible with the observed stretched exponential transient is proposed for the a-IGZO system.

Acknowledgements

Before going into technical details, I would like to express my sincere gratitude to everyone who have helped me during my study at Northwestern.

First and foremost, I would like to thank my advisor, Prof. Matthew Grayson, for his patient guidance and insightful advices in all aspects of research. I would also like to thank Prof. Robert Chang, Prof. Tobin Marks, Prof. Julia Medvedeva, Prof. Bruce Wessels, and Prof. Thomas Mason for serving on my thesis and prospectus committees.

I was luck enough to work with many excellent collaborators in the Materials Research Center at Northwestern. This work would not be possible without their expertise. In particular, Alex Adler and Stephanie Moffitt of the Mason group contributed significantly to my understanding of amorphous oxide materials, and D. Bruce Buchholz of the Chang group provided many inspiring research suggestions far more than thin film deposition.

Special thanks to everyone in the Grayson group, working with them everyday in the past few years will be my most cherished memory. Also to my friends outside the lab, who may not understand my research, yet always encouraged me to work hard and move forward. I could not finish this journey without them on my side.

Last but not least, to my parents and my wife. Thank you for everything.

Table of Contents

ABSTRACT 3

Acknowledgements 6

List of Tables 10

List of Figures 11

Chapter 1. Introduction 31

1.1. Amorphous oxide semiconductors and a-IGZO 31

1.2. Electronic structure of a-IGZO 33

1.3. Instability under illumination 36

1.4. Thesis outline 39

Chapter 2. General properties and transients of a-IGZO 41

2.1. Thin film growth 41

2.2. Sample preparation 44

2.3. Measurement setup 47

2.4. Electrical properties 53

2.5. Characteristics of photoresponse and photo-instability 60

2.6. Summary 66

Chapter 3. Novel methods for measuring transients 67

3.1. Need for new measurement methods 67
3.2. Frequency modulated non-switching van der Pauw method 69
3.3. Heterodyne method for van der Pauw and Hall measurements 77
3.4. Modular time division multiplexer for efficient simultaneous characterization of fast and slow transients in multiple samples 96
3.5. Second round: Transient photoconductivity for a-IGZO thin films 100

Chapter 4. Mathematical Analysis of General Transient Response 104
4.1. Generalized transient response with distributed time constants 105
4.2. Fitting methods for transients with distributed time constants 111
4.3. Semi-log transient plot and log-scale derivative 125
4.4. Introducing the skew normal: Best estimation of time constant distribution 130
4.5. Analysis of long term transient photoresponse in a-IGZO 135

Chapter 5. Physical Mechanisms for Transient Photoresponse in a-IGZO 140
5.1. Stretched exponential fit for transient photoresponse in a-IGZO 140
5.2. Time constant distribution of the stretched exponential transients 144
5.3. Distributed activation energy model 148
5.4. Continuous-time random walk model 152
5.5. Microscopic CTRW mechanism for a-Si:H band tail electron relaxation: Hydrogen diffusion 159
5.6. Candidate mechanisms for photoconductivity in a-IGZO 162
5.7. Microscopic CTRW mechanism for a-IGZO photoconductivity relaxation: Introducing the metallic bond diffusion model 167

References 171

Appendix A. Circuit schematic of a MTDM unit 184

Appendix. Vita 185

List of Tables

5.1 Comparison of different stretched-exponential systems with the generic CTRW model. 158

List of Figures

1.1 Schematic illustration of the conduction mechanism of traditional covalent semiconductor and ionic oxide semiconductor in crystal and amorphous phases. Figure reproduced from reference [**4**]. 32

1.2 A schematic illustration of the AOS band structure. Figure reproduced from reference [**10**]. This band diagram plots segments of the density of state (DOS) distribution measured by different experiments in a single graph. Thus the density at the same energy level measured from different experiments may not be consistent with each other. 34

1.3 (a) Hall mobility in a-IGZO measured as a function of carrier concentration. (b) Schematic illustration of the electron percolation process. The arrows indicate electron conduction paths. Bottom part is the cross-section of the potential distribution, where E_{F} is the Fermi level, and E_{th} is the threshold energy above which electrons move freely. Figures adapted from reference [**4**] and [**21**] by Hosono *et al.* 36

1.4 (a) I-V curve as a function of negative-bias stress (NBS) time in an a-IGZO based TFT. (b) I-V curve as a function of negative-bias illumination stress (NBIS) time in an a-IGZO based TFT illuminated by white light. There is only a small threshold voltage shift under

NBS in (a) and a very large threshold voltage shift under NBIS in (b). (c) Transient photoconductivity data obtained by 3.1 eV photo excitation on an unannealed a-IGZO thin film. Inset shows an zoom-in view of the initial transient under illumination. Note the illumination was stopped before reaching the saturation conductivity. (d) Density of trap states associated with the slow photo response in a-IGZO thin films assuming a distributed activation energy model. Panels (a) and (b) are adapted from reference [**29**], and panels (c) and (d) from reference [**20**]. 38

2.1 Electrical properties in the $In_2O_3-Ga_2O_3-ZnO$ ternary system as measured by Nomura *et al.* [**45**] (a) Carrier concentration as a function of oxygen partial pressure during PLD deposition in amorphous InZnO (a-IZO) thin films and a-IGZO thin films. (b) Electron mobilities and concentrations measured from the Hall effects for PLD-grown amorphous thin films in the $In_2O_3-Ga_2O_3-ZnO$ ternary system. The values in (b) denote the electron Hall mobility (cm^2/Vs) with density (10^{18} cm^3) in parentheses. 43

2.2 Procedure to encapsulate a thin film sample. Scotch tape covers part of the substrate during the deposition to provide the desired film pattern. The tape is removed after the deposition, then the sample is covered with quartz slide on top and sealed with epoxy on the cover edges to isolate the film at the center area from ambient air. The left column shows the schematics and the right column shows the sample

pictures at each corresponding step. A metal film test sample is used to better show the film area since a-IGZO is transparent. 46

2.3 Contact configurations for the two 4-point resistances in a van der Pauw measurement. In the left configuration, by applying current I_{AB} through pin A to B and measuring voltage V_{DC} between pin D and C, 4-point resistance $R_{AB,DC}$ is measured. Similarly, in the right configuration, by applying current I_{CB} through pin C to B and measuring voltage V_{DA} between pin D and A, 4-point resistance $R_{CB,DA}$ is measured. 48

2.4 A typical Hall measurement setup (left) and measurement result for an n-type semiconductor. The magnetic field B perpendicular to the thin film is swept during the measurement. By applying a current I_{AC} through pin A to C and measuring the voltage V_{BD} between two pins B and D, the transverse resistance R_{xy} defined as $R_{xy} = R_{AC,BD} = V_{BD}/I_{AC}$ is recorded during the sweep. Carrier density and mobility are extracted using the linear fit (red line in the right panel) of R_{xy} as a function of B. 49

2.5 Experiment setup for the illumination and annealing measurements. (a) Schematic setup of illuminating and annealing a sample. The sample is illuminated with a UV LED placed on top, and annealed with a temperature controller unit thermally attached to the sample through a copper stripe. The sample is electrically contacted using the van der Pauw configuration for electrical measurements. (b) Setup

during the first round of measurements. A through-hole UV LED is used as light source. Temperature is controlled with a heater resistor and monitored with a thermistor. (c) Sample chamber used in the second round or measurements, with 1. a high-power UV LED to illuminate the sample, 2. a sample holder directly under the LED and thermally attached to the aluminum box, and 3. an aluminum heat sink to dissipate LED heat. 52

2.6 Electrical properties of pristine a-IGZO thin films right after PLD deposition. (a) Dependence of carrier densities n as a function of oxygen pressure P_{O_2} during deposition. (b) Dependence of initial electron mobility μ as a function of initial carrier density n for pristine samples deposited at different oxygen pressure P_{O_2}. Note that mobility μ is only increasing linearly by less than 25% when carrier density n increases exponentially by two orders of magnitude. 54

2.7 (a) Gate voltage V_{g} dependence of the drain-source current I_{DS} with the drain-source voltage $V_{\mathrm{DS}} = 1$ V and 10 V. The inset shows the same transfer characteristic with log-scale current. The sweep rate for gate voltage V_{g} is 20 V/min. (b) Gate voltage V_{g} dependence of thin film conductivity σ. $V_{\mathrm{DS}} = 0.1$ V was used to ensure the device was operating in the linear region. The sweep rate for gate voltage V_{g} is 4 V/min. The sweep directions are labeled by the arrows in both panels. Hysteresis between the up-sweep and down-sweep is observed in both measurements indicating bias-stress instability. 55

2.8 (a) Gate voltage V_g dependence of the thin film capacitance C with sweep rate of 6, 4, 2, and 1 V/min. The hysteresis increased with decreasing sweep rate. (b) Gate voltage V_g dependence of thin film conductivity σ, measured on the same sample in three different dates. The gate sweep rate was 4 V/min. The entire transfer curve shifted over days without bias stress. 56

2.9 Conductivity transient during and after 80 ℃ annealing on desktop in a dark environment for 200 nm a-IGZO thin films. The samples were deposited by PLD at P_{O_2} = (a) 5 mTorr, (b) 10 mTorr, and (c) 15 mTorr. Even though the samples showed different transients during annealing, all samples had decreased conductivity after about a day of annealing. 58

2.10 In-situ resistivity change in a 100 nm a-InZnO thin film during 200 ℃ annealing, as measured by Lee et al. [**57**] The resistivity was increasing initially and started to decrease after $\sim$ hours of annealing. 59

2.11 Wavelength dependence of photoresponse in a 140 nm P_{O_2} = 15 mTorr a-IGZO thin film sample. Conductivity σ versus time t under illumination with (a) 630 nm red LED, (b) 565 nm green LED, (c) 430 nm blue LED, and (d) 405 nm UV LED are shown. The areas with white backgrounds indicate the time under illumination, and the areas with gray backgrounds indicate the time in dark. Red and green LEDs show no dependence on illumination, with the same decay with

time as under dark conditions. Blue and UV LEDs show an order of magnitude increase in conductivity after illumination. 61

2.12 Comparison of photo-excitation and dark relaxation conductivity σ (left axis) over time t for thin films deposited at oxygen pressure P_{O_2} = 5, 10, and 15 mTorr for panels (a), (b), and (c), respectively. All measurements were conducted at room temperature in a He-flow cryostat. The conductivity measurement was briefly interrupted and the Hall mobility was measured at discrete time points, as shown by the green squares (right axis) in each graph. All samples showed approximately constant mobility μ during photo-excitation and dark relaxation. 62

2.13 Comparison of the photoresponses under as-grown, anneal, and post-anneal states in a-IGZO thin films. The left column (a), (c), and (e) are LED illumination transients and the right column (b), (d), and (f) are dark relaxation transients. The first row (a) and (b) are the transients in the P_{O_2} = 5 mTorr sample, the second row (c) and (d) are the transients in the 10 mTorr sample, are the third row (e) and (f) are the transients in the 15 mTorr sample. The transients of the conductivity $\sigma(t)$ was measured, and the relative conductivity $\Delta\sigma(t) = \sigma(t) - \sigma(t = 0)$ is plotted. The initial conductivity $\sigma(t = 0)$ was measured right before the LED was turned on or off. For all samples, enhanced photoresponses were observed during 350 K

annealing, and decreased photoresponses were observed at 300 K post-anneal. 65

3.1 Schematic illustration of combining two van der Pauw measurement circuits of different contact configurations into a single frequency-modulated non-switching van der Pauw circuit. Note the current ground contact labeled B is shared by both frequencies. 71

3.2 Magnetoresistance measurement results in a test GaAs quantum well sample measured by the standard van der Pauw method (thick black curves) and the frequency-modulated non-switching van der Pauw method (thin colored curves). The results shown are (a) $R_{\mathrm{xx1}} = R_{13-14,12-15}$, (b) $R_{\mathrm{xx2}} = R_{15-14,12-13}$, and (c) sheet resistivity ρ_{xx} during magnetic sweeps between -5 T and 5 T. The inset of (a) shows the contact geometry. 72

3.3 Noise level of the frequency modulated non-switching van der Pauw method measured with (a) f_1 = 13, 29, 73, 113 Hz and f_2 = 17 Hz, (b) f_1 = 17 Hz and f_2 = 13, 29, 73, 113 Hz, (c) f_1 = 73, 89, 133, 173 Hz and f_2 = 77 Hz, (d) f_1 = 29 or 73 Hz and f_2 = 17 Hz, using contact # 12, 13, 14, and 15 alternately as the ground contact. From panels (a-c), the noise level appears to depend mostly on the frequency difference $f_1 - f_2$. Panel (d) shows that the choice of the ground contact also affects the interference noise level. The contact geometry is shown as the inset of Fig. 3.2(a). 74

3.4 Comparison of the transients for 4-point resistances and the sheet conductivity. (a) Measured dark relaxation of longitudinal resistances R_{xx1} and R_{xx2} in a 50nm PLD-grown 10 mTorr a-IGZO thin film after UV LED illumination. (b) Calculated sheet resistance R_{sheet} and geometry factors $R_{\mathrm{sheet}}/R_{\mathrm{xx1}}$ and $R_{\mathrm{sheet}}/R_{\mathrm{xx2}}$ during the relaxation transient. The geometry factors were almost constant during the relaxation. (c) Calculated conductivity σ and the error ϵ when σ is estimated using only R_{xx1} or R_{xx2} assuming constant geometry factors. With conductivity changing by more than 10 %, the error caused by assuming an illumination-independent geometry factors was less than 1 %. 76

3.5 Circuit design for the heterodyne van der Pauw method. The current source circuit (a) provides the driving current I_a at frequency ω_a from contact A to B, and I_b at frequency ω_b from contact C to B. The voltage heterodyne circuit (b) generates a single output voltage $V_{\mathrm{O}} = \frac{V_{DC}(t)V_b(t)+V_{DA}(t)V_a(t)}{V_R}$ through analog adders and multipliers. 78

3.6 Circuit design of the heterodyne Hall method. The current source circuit (a) provides current I_a at frequency ω_a from contact A to C, and current I_b at frequency ω_b from contact D to B. The voltage heterodyne circuit (b) generates a single output voltage $V_{\mathrm{O}} = \frac{V_{BD}(t)V_b(t)-V_{AC}(t)V_a(t)}{V_R}$ through analog adders and multipliers. A calibration potentiometer R_P is included to match the amplitude of V_a and $-V_b$. 84

3.7 Measurement results of R_{xy} using the conventional Hall method on the 200 nm 5 mTorr PLD-grown a-IGZO test sample. 86

3.8 Magnetic field sweep results using the heterodyne Hall method on the 200 nm 5 mTorr PLD-grown a-IGZO test sample. (a) Directly measured amplitude and phase of output signal V_{out} as a function of time t. A linear drift of V_{out} phase can be observed. (b) The amplitude and phase of V_{out} after synchronicity correction plotted as a function of magnetic field B. The results for the up-sweep and down-sweep now align well with each other. Note the $|V_{\text{out}}|$ still does not reach 0 at $B = 0$ even after synchronicity correction. (c) The real and imaginary part of V_{out} after synchronicity correction plotted as a function of magnetic field B. Note the real part depends linearly on B, and there is a constant non-zero offset in the imaginary part. 87

3.9 Schematic illustration of the components that added up to produce the measured output V_{out}. (left) V_{out} decomposed as the sum of the multiplier outputs in an ideal circuit. V_{out} is 0 at $B = 0$, and changes linearly with B. (right) V_{out} decomposed as the sum of multiplier outputs in a real circuit, where the phase misalignment causes non-zero V_{offset} at $B = 0$. V_{out} measured in a real circuit can be decompose as the vector sum of V_{Hall} and V_{offset}, where V_{Hall} changes linearly with B and V_{offset} remains constant. 90

3.10 Measurement results of $|V_{\text{out}}|$ using the heterodyne Hall method on the 200 nm 5 mTorr PLD-grown a-IGZO test sample with maximum

field of only $B_{\max} = \pm$ 0.1 T. The calibration potentiometer R_P was intentionally off-calibrated to have $|V_{\text{out}}| \gg |V_{\text{offset}}|$ at $B = 0$. The sweep was repeated several times to check reproductivity of the results. 91

3.11 Carrier density transient measured using the heterodyne Hall method on the 50 nm 15 mTorr capped PLD-grown a-IGZO thin film sample. The magnetic field was kept at 5 T during the measurement. The sample was illuminated by a 385 nm UV LED operating at 10 mA constant current. The time range with LED on is indicated by the white background. The sample was kept in dark when not illuminated, as indicated by the gray background. 93

3.12 System design of the modular time division multiplexer (MTDM) unit. Solid lines symbolize the dedicated mode connections. Dashed lines represent the multiplexed mode connections. The hollow lines are data bus signals to and from the computer. A two-layer hierarchy with 4 channels in each layer is shown. The slave MTDM units have the same internal design as the master MTDM unit. At the top of the figure, the measurement instruments are used for the dedicated mode and the multiplexed mode respectively. The rotary switch is in position 1 indicating that the $k = 1$ sample is in the dedicated mode. 98

3.13 Second round of conductivity transients measurement results for the a-IGZO thin film samples. (a) Transient conductivity change of pristine a-IGZO thin film samples after PLD deposition. (b) Transient

photoconductivity of a-IGZO thin films under UV LED illumination. (c) Transient photoconductivity of a-IGZO thin films during dark relaxation after prolonged UV LED illumination. 101

4.1 Transient photoconductivity of a-IGZO compared to simple exponential fits in (a) photo-illumination and (b) dark relaxation of the 5 mTorr capped sample, and (c) photo-illumination and (d) dark relaxation of the 10 mTorr capped sample. The measured transient photoconductivity is plotted as the thick red curves for the 5 mTorr sample, and the thick green curves for the 10 mTorr sample. The best simple exponential fit to the initial 1/3 of each curve is plotted as a dotted gray line, and the best simple exponential fit to the final 1/3 of each curve is plotted as a dashed gray line. Note the best simple exponential fits at short time scales do not match those at long time scales. 106

4.2 (a) Simulated log-scale transient response $F(x)$ (thick gray line) assuming Gaussian distributed spectrum and (b) simulated transient response $F(x)$ (thick gray line) assuming stretched exponential transient, and the fitting results using the continuum multi-exponential (CME) fit (red solid line), the Gaussian distribution fit (blue dashed line), and the stretched exponential (SE) fit (green dotted line). (c) and (d) Decay spectra $G(u)$ corresponding to the fitted responses in (a) and (b), respectively. The model Gaussian

spectrum is plotted as the light blue area, and the model SE spectrum is plotted as the light green area. 120

4.3 (a) Plot of a simulated Gaussian distributed spectrum (light blue area), and (b) of a simulated spectrum associated with the stretched exponential (SE) model (light green area), with curves indicating the decay spectra corresponding to the Gaussian predictive method (blue dashed lines), stretched exponential (SE) predictive method (green dotted lines), and continuum multi-exponential (CME) descriptive method (red lines). Three measurement durations $t_{\text{meas}} = 0.1\ \tau_0$, τ_0, $10\ \tau_0$ are displayed as white windows from left to right in each panel. When the predictive lineshape matches the simulated data lineshape, the measurement duration can be quite short, only 1/10 of the τ_0 time scale. However, if the predictive lineshape does *not* match the simulated data lineshape, the convergence is poor. The CME method, on the other hand always converges well, but requires a measurement of 10 times τ_0. 122

4.4 Convergence plots: The convergence trend of the decay spectrum shape from the Gaussian predictive method (blue), the stretched exponential (SE) predictive method (green), and the continuum multi-exponential (CME) descriptive model (red) as a function of measurement duration t_{meas} when applied to (a) a transient generated assuming a Gaussian distributed spectrum, and (b) a stretched exponential transient. Lineshape accuracy is identified by the spectral

peak position u_p, the linewidth Δu, the integrated area A, and the RMS error ε. 123

4.5 Plots of (a) simple exponential decay function $h(t, \tau_0)$, (b) unit decay response $H(x)$ as a function of log-time x, and (c) derivative of unit decay response $-H'(x)$. The derivative peak maximum $x_{H,p}$ is indicated with the solid circle and the vertical line. The width at half maximum is indicated with the horizontal line. 126

4.6 (a) Transient responses $f(t)$ following simple exponential (red solid line), Gaussian distributed multi-exponential (blue dashed line), and stretched exponential (green dotted line) in linear time scale t. (b) Transient responses $F(x)$ in (a) plotted in log-time $x = \ln(t/\tau_0)$. (c) The derivative $-F'(x)$ with respect to log-time x. Inflection points x_p in the original semi-log plot appear as maxima in the derivatives in panel (c) and are indicated with solid circles and vertical lines. Full width at half-maximum Δx are indicated with horizontal lines. (d) Time constant distribution spectrum $G(u)$ in log time-constant scale $u = \ln(\tau/\tau_0)$ for transient responses in panels (a) and (b). The solid circles and vertical lines in panel (d) indicate the maxima $u_{0,p}$ in the decay spectra, and the horizontal lines indicate the half-maximum width Δu_0 of the each spectrum. 128

4.7 (a-c) Comparison of the skew normal (SN) distribution spectra with the Gaussian distributed spectra with the width parameter $s = 1.003$, 1.729, and 5.042 respectively. (d-f) Comparison of the skew normal

(SN) distribution spectra with the Gaussian distribution spectra with the SE shape parameter $\beta = 0.7$, 0.5, and 0.2 respectively. The semi-log response $F(x)$, semi-log derivative $-F'(x)$, and log-scale spectrum $G(u)$ of the model Gaussian spectrum transients are plotted as the blue lines, and those of the model stretched exponential transients are plotted as the green lines. All corresponding skew normal fits are plotted as the light gray lines and in general show the ability to provide excellent fits to both the Gaussian and stretched exponential lineshapes. 136

4.8 (a) Semi-log plot of measured transient photoconductivity of the 5 mTorr capped sample during photo-illumination (thick red line) and the transient photoconductivity corresponding to the estimated skew normal decay spectrum (thin orange line). (b) Semi-log plot of transient photoconductivity of the 5 mTorr capped sample during dark relaxation. (c) Derivative of the semi-log photo-excitation transient plots in (a). Both the measured derivative (thick red line) and the derivative from the estimated skew normal decay spectrum (thin orange line) are plotted. The maximum derivative point in the measured derivative is indicated by the solid circle and the vertical line. The half-maximum derivative points are indicated by the horizontal line. (d) Derivative of the semi-log dark relaxation transient plot in (b). (e) Skew normal decay spectrum of the photo-excitation transient plot in (a), estimated using the empirical Eq. (4.19). 139

5.1 The stretched exponential responses for $\beta = 1$, 0.75, 0.50, and 0.25, respectively. The transient responses are plotted versus linear time t in (a) and log-scale time x in (b). Note that the stretched exponential curves in (b) have the same shape as the simple exponential curve with $\beta = 0$, except linearly stretched by a factor of $1/\beta$. 142

5.2 Stretched exponential fit for transient responses measured in the 50 nm capped 5 mTorr sample. Panel (a) shows the photo-excitation transient, and panel (b) shows the dark relaxation transient. The measured transient photoconductivities are plotted as the red squares, and the stretched exponential fittings are plotted as the gray lines. 144

5.3 (a) Log-scale time constant distribution $G(u)$ corresponding to stretched exponential responses with different β values. The left-right arrow indicates the full-width at half-maximum linewidth Δu. (b) Dependence of Δu on the β values for stretched exponential responses. Squares are calculated directly using inverse Laplace transform and the solid line is the empirical relation in Eq. (5.4). The inset shows how well the empirical fit matches the calculated spectrum linewidths on a log-log scale. 145

5.4 Log-scale decay spectra $G(u)$ for the stretched exponential fittings to transient photoconductivity during (a) photo-excitation and (b) dark relaxation in the 50 nm capped 5 mTorr a-IGZO sample. The decay spectra are deduced from inverse Laplace transforms of stretched exponential fittings. The dark red segments of the curves correspond

to the time scales with directly measured responses, and the red segments correspond to an extrapolation following the stretched exponential function beyond the measured time scales. 146

5.5 Assuming the distributed activation model, one can plot the density of state (DOS) distributions $D(E)$ for the stretched exponential fittings to the transient photoconductivities in the capped $P_{O_2} = 5$ mTorr sample. E indicates binding energy below the mobility gap, such that states to the right would be more deeply bound. Panel (a) shows the DOS for photo-excitation and panel (b) for dark relaxation. The segments with dark red color indicate energy ranges with time constants that were directly measured. The DOS distributions are derived assuming the attempt-to-escape frequency $\nu = 10^{13}$ Hz. 149

5.6 Normalized decay curves for photo-induced defect density in a carbon-doped a-Si:H sample at various annealing temperatures T_A as measured by Stutzman *et al.* [**113**] Following the distributed activation energy model, the decay curves are plotted as a function of activation energy E assuming the attempt-to-escape frequency to be (a) $\nu = 10^{10}$ s^{-1}, and (b) $\nu = 10^{6}$ s^{-1}. On those plots, the activation energy distributions $D(E)$ are the derivatives of the decay curves with respect to E. With $\nu = 10^{6}$ s^{-1}, all annealing temperatures yield the same decay curve, indicating a correct choice of frequency scale ν. 151

5.7 Schematics of the continuous-time random walk process. (a) Illustration of the random walk path of a mobile defect moving from

position 1 to position 2 on a two-dimensional lattice from the work of Metzler. [**117**] The defect has equal probability to "walk" to a nearest neighboring site in each step. The circle diameters at each visited site symbolizes the waiting time t that the defect stays in the site before making the next step. (b) Illustration of a frozen dipole waiting to be relaxed by mobile defects from the work of Shlesinger. [**118**] The X in the center represents the dipole. The circle represent neighboring defects. The relaxation happens when any one of the defects visits the dipole for the first time. 154

5.8 (a) Schematic illustrations of a defect diffusing through a 1-D lattice with distributed activation energies, where a deeply bound activation energy well Δ corresponds to a longer expected waiting time t at the site, and vise-versa. (b) An exponential tail distribution $f(\Delta) \propto \exp(-\Delta/k_B T_0)$ for the activation energies Δ. The characteristic energy scale (average energetic distribution width) for the exponential tail is $k_B T_0$. Such an exponential activation energy distribution $f(\Delta)$ will result in a power-law waiting time distribution $\psi(t) \sim t^{-1-\frac{T}{T_0}}$ provided that $T < T_0$. 155

5.9 Illustration of stretched exponential relaxations and temperature dependence in the a-Si:H system as measured by Kakalios *et al.* [**89**] (a) Time dependence for the shallow occupied band-tail state density n_{BT} plotted versus log-time. The solid circles are the experimental results, and the solid lines are the stretched exponential fitting results

determining the β values at each temperature. (b) Temperature dependence of exponent β. The solid circles are obtained from the stretched exponential fitting in (a) to the n_{BT} relaxation. The open circles are obtained from the power-law fitting to hydrogen diffusion coefficient transient (not shown) in p-type samples, and the open square from the n-type samples. The β values obtained from different experiments and different samples follow the same linear temperature dependence, as indicated by the line. 160

5.10 Successive steps illustrating a microscopic model for dangling bonds created by hydrogen diffusion in a-Si:H from the work of Morigaki. [**122**] At step (1) there are no dangling bonds. A spontaneous thermally generated anti-bonding of a pair of neighboring Si atoms is shown in step (2). Steps (3) to (5) show the Si-H bond switching associated with H diffusion. In the final step (6), two separate dangling bonds are created. 161

5.11 Transient photoconductivity after steady UV illumination in capped (dark red, dark green) and uncapped (light red, light green) a-IGZO samples. Results for 50 nm PLD-grown samples deposited at 5 mTorr and 10 mTorr are shown. Both capped samples showed the conductivity decreasing monotonically with decreasing rate, while both uncapped samples showed irregular step-like conductivity change at long time scales. 164

5.12 Schematic band diagrams showing the likelihood of hole trapping at the IGZO/dielectric interfaces adapted from the work of Jeong. [**24**] (a) Band diagram of the IGZO/SiN_x interface. The valence band maximum of the SiN_x layer is higher than that of the a-IGZO layer, so holes can be trapped at the IGZO/SiN_x interface, causing device instability. (b) Band diagram of the IGZO/SiO_2 interface. The valence band maximum of the SiO_2 layer is much lower than that of the a-IGZO layer. The large hole energy barrier prevents holes from being trapped at the interface. 165

5.13 Molecular dynamics simulation results from Medvedeva showing the metastable under-coordinated metallic bonds M-M where M = {In,Ga,Zn}. [**127**] Such bonds fit the description of an "oxygen vacancies" since the local coordination number with oxygen atoms is reduced. (a) Local structure surrounding an under-coordinated In-Zn metallic bond with In atoms pink, Zn atoms gray, Ga atoms green, and O atoms red. The areas with yellow color indicate high electron probability densities. (b) The same region of the sample but now the local structure reveals an undercoordinated In-In metallic bond. Note that when transitioning from the In-Zn bond to the In-In bond, there is also a change in oxygen positions. The binding energy of the In-Zn bond is shallower ($\sim$ 0.8 eV; lower local electron density 0.66 e^-) than the binding energy of the In-In bond ($\sim$ 1.2 eV; higher local electron density 1.06 e^-). (c) The metal-metal distance d_{M-M}

between neighboring cations, showing the In-In pair (purple trace) and a neighboring In-Zn pair (orange trace) during the molecular dynamics quench from high temperature (left) to low (right). At high temperatures, higher-energy configurations of the under-coordinated cations such as the In-Zn metallic bond can be identified, such as the In-Zn bond that was observed at 1300 K when the In-Zn bond distance showed a dip and the In-In bond distance simultaneously showed a peak. 168

A.1 The circuit schematic of a MTDM unit for measuring the transient photoconductivity of a-IGZO samples. $V_{D;in}$ and $V_{M;in}$ are voltage inputs to the current sources for the dedicated mode and the multiplexed mode, respectively. The difference between V_D+ and V_D- is the four-point voltage across the sample that is being measured in the dedicated mode. The difference between V_M+ and V_M- is the voltage across the sample in the multiplexed mode that is indexed by the two multiplexers. A computer program written in Python indexes the multiplexers using pins $V_{\mathrm{MUX}}0$ through $V_{\mathrm{MUX}}3$. 184

CHAPTER 1

Introduction

1.1. Amorphous oxide semiconductors and a-IGZO

Although crystalline silicon-based traditional semiconductor devices have been successfully scaling down for decades, they cannot be easily adapted in large-area electronics such as display devices. Instead, silicon in the amorphous form (a-Si) has been widely used for making the thin films transistor (TFT) circuits that control the pixels in display devices. However, the amorphous structure significantly affects the electrical performance for a-Si. Compared to single-crystal silicon with electron mobility of 1400 cm^2/Vs at room temperature, a-Si only has electron mobility below 1 cm^2/Vs. For next generation displays with faster refresh rates and increased pixel densities, each pixel has to respond much faster, thus requiring the controlling TFTs to have higher mobilities. For example, a 4K display device with resolution of 3840 $\times$ 2160 operating at a refresh of 120 Hz requires TFTs with minimum mobility $\sim$ 3 cm^2/Vs. [**1**] Such a mobility value is higher than that can be achieved with a-Si. New amorphous materials with higher mobilities are therefore needed.

In 1996, Hosono *et al.* proposed that amorphous ionic oxides with large, spherical s orbitals around the metal ions will maintain a high mobility even in the amorphous phase. [**2**, **3**] Fig. 1.1 compares the schematic structure of conventional covalent semiconductors and ionic oxide semiconductors. In covalent semiconductors such as silicon, carrier

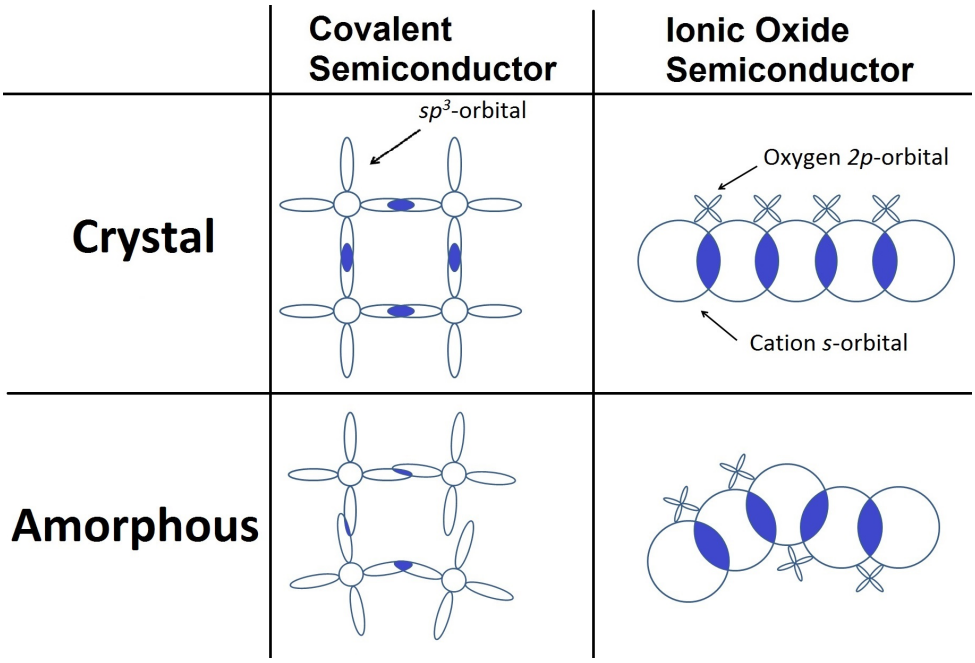

Figure 1.1. Schematic illustration of the conduction mechanism of traditional covalent semiconductor and ionic oxide semiconductor in crystal and amorphous phases. Figure reproduced from reference [**4**].

transport is conducted through the strongly directional tetragonally oriented sp^3 orbitals. The overlap of neighboring orbitals decreases drastically in amorphous phase, leading to much lower mobility in amorphous silicon than in crystalline and poly-crystalline silicon. On the other hand, in ionic oxides with s orbital cations, electron transport is through the overlap of the spherical s orbits. Since the overlap has little directional dependence, the mobility is not as strongly reduced in the amorphous phase.

Based on the theory of electron conduction through s orbital overlap, it is further predicted that In, Ga, Zn, and Sn are the best candidate elements for cations that have low toxicity, high earth abundance, and large s-orbital overlaps. [**5**] In 2004, Hosono's group demonstrated the first amorphous In-Ga-Zn-O (a-IGZO) based transparent flexible

thin film transistor (TFT) fabricated at room temperature. [**4**] Those films showed Hall mobility around 10 cm^2/Vs, significantly large than that of a-Si (< 1 cm^2/Vs), and comparable with single-crystalline IGZO. [**6**] Since then, amorphous oxide semiconductors (AOSs), especially a-IGZO, received increasing attention, and were later adapted by the display industry as one of the most widely used alternates for a-Si since 2012. [**1**, **7**, **8**]

Besides high electron mobility, a-IGZO has several advantages over traditional a-Si and high mobility poly-crystalline silicon. It generally has a large band gap (larger than 3 eV), and is thus mostly transparent to visible light. This transparency nature makes it the ideal material for the electrodes and controlling circuits in solar cells and augmented reality devices. [**1**, **7**, **9**] Due to their amorphous nature, deposition of a-IGZO thin films is more cost-efficient, uniform, scalable, and can be processed entirely at room temperature, making a-IGZO compatible with flexible electronics on organic substrates. [**1**, **4**, **10**, **11**]

1.2. Electronic structure of a-IGZO

Unlike crystalline materials, there is no well-defined band-gap in amorphous materials. Instead, the band structure in amorphous materials are usually defined by their mobility edges, analogous to the conduction band minimum and valence band maximum in crystalline semiconductors. [**12**] The electron mobility edge is defined as the minimum energy level at which electrons can hop around in the material for a given operating temperature, while electrons below the mobility edge are localized. Thus the states below the electron mobility edge are categorized as localized, or trap states. Similarly for the hole mobility edge, holes below it are free to move and holes above it are localized.

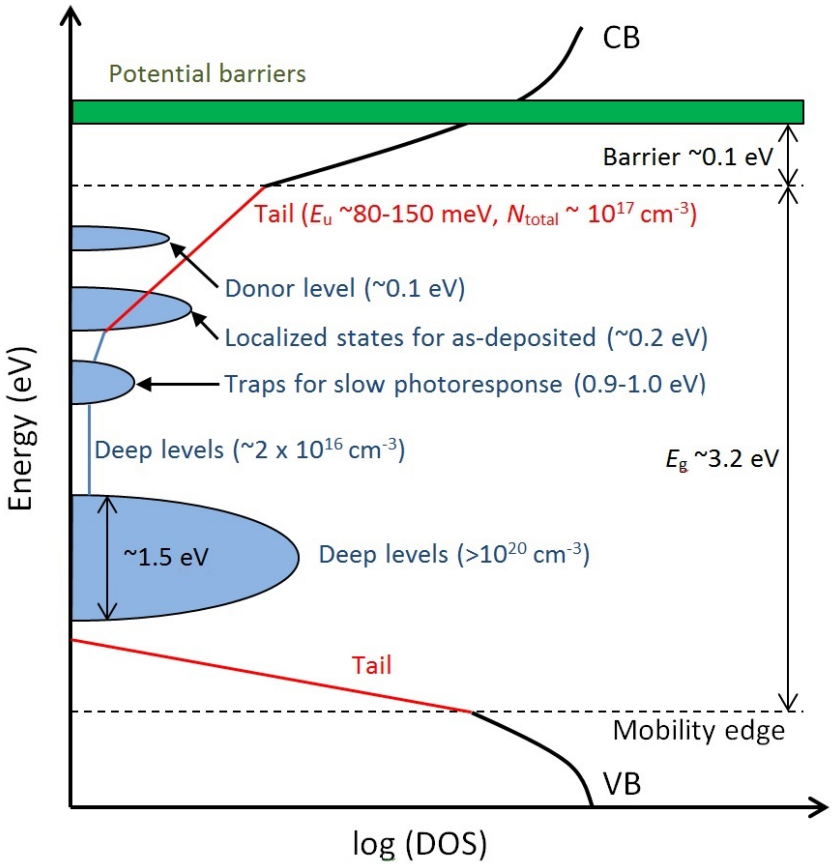

Figure 1.2. A schematic illustration of the AOS band structure. Figure reproduced from reference [**10**]. This band diagram plots segments of the density of state (DOS) distribution measured by different experiments in a single graph. Thus the density at the same energy level measured from different experiments may not be consistent with each other.

Similar to crystalline semiconductors, the states between mobility edges have significant influence on the electrical and optical properties of amorphous oxides. Combining density of states (DOS) segments measured from optical absorption, X-ray photoemission spectroscopy and C-V analysis on the same plot, Kamiya *et. al.* proposed a model for the electronic structure of a-IGZO as shown in Fig. 1.2. [**10**, **13**–**15**] In Fig. 1.2, the mobility edges are shown as dashed line. The red curves are the tail states below electron

mobility edge and above hole mobility edge. Tails states near the mobility edges, also called Urbach tails, are commonly observed in amorphous materials, and often modeled to have an exponential distribution. [**16**–**18**] The states close to the electron mobility edge were proposed to be the donor levels. And they were suggested to originate from oxygen vacancies in the oxide structure. [**19**] The states $\sim$ 0.2 eV below the mobility edge were not observed after annealing. They were reported responsible for the hysteresis observed in the C-V and TFT characteristics. [**15**] The traps states $\sim$ 1 eV below conduction band were associated by Hosono *et al.* with the slow photoresponse, [**20**] which will be further investigated in this work. The deep level traps near the valence band were found to have very high density. This might explain why a-IGZO based transistors cannot operate in the p-channel mode. [**13**] The states between the mobility edges also depends heavily on the fabrication processes. [**14**]

The band structure proposed in Fig. 1.2 provides a quick summary of many different effects observed in a-IGZO. However, it assumes that a unified density of state (DOS) distribution governs all those properties in a-IGZO, and each experiment separately tests a segment of the entire DOS distribution. Before making such assumptions, the measurement methods and results need to be carefully examined and alternate models explored, lest the interpretation as sub-gap DOS distribution peaks be too hastily adopted.

Electron transport in amorphous IGZO is also very different from that in crystalline semiconductors. It is observed that the electron mobility increases with increasing electron doping density in a-IGZO, [**4**] as shown in Fig. 1.3(a), whereas the electron mobility decreases with doping density in crystalline silicone. This observations suggests that the electron transport in a-IGZO should be described as percolation in a random distribution

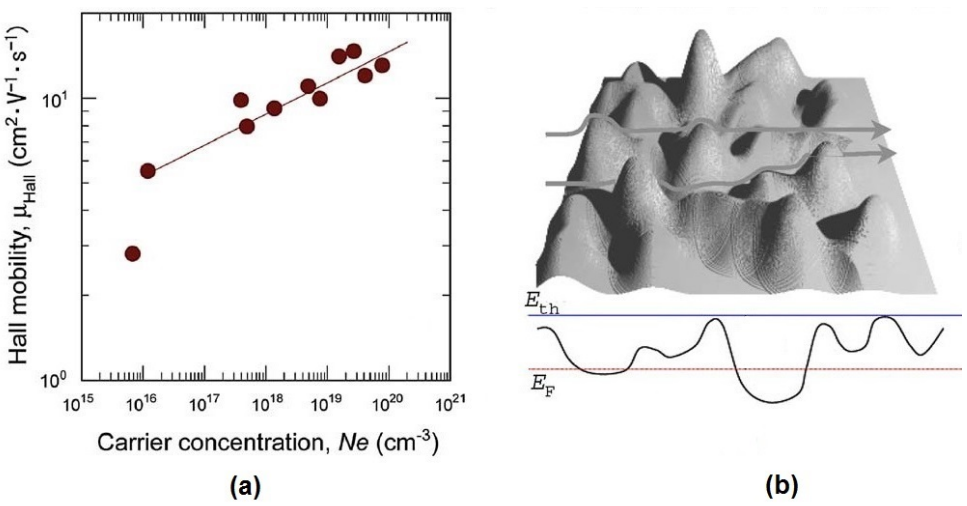

Figure 1.3. (a) Hall mobility in a-IGZO measured as a function of carrier concentration. (b) Schematic illustration of the electron percolation process. The arrows indicate electron conduction paths. Bottom part is the cross-section of the potential distribution, where E_{F} is the Fermi level, and E_{th} is the threshold energy above which electrons move freely. Figures adapted from reference [**4**] and [**21**] by Hosono *et al.*

of potential barriers, [**21**] as illustrated in Fig. 1.3(b). The potential barriers described by the percolation model typically have barrier heights about 0.1 eV above the conduction band mobility edge, shown as the green band in Fig. 1.2.

1.3. Instability under illumination

The biggest challenge currently for a-IGZO and other AOSs is their instability under stress. [**7**, **8**, **22**, **23**] Bias-, thermal-, and illumination-stress are all observed to induce a shift in the turn-on threshold for transistor devices, and the shift is not static, but relaxes with a slow relaxation time. [**20**, **23**–**26**] Such instability can result in increased power consumption, performance degradation, or even device failure. As of 2016, as reported at the Gordon Research Conference on Hybrid Electronic and Photonic Materials and

Phenomena, illumination induced instability remains one of the major unsolved problems in a-IGZO community. [**27**] In this work, we will focus on the transient behavior of illumination induced instability, as being representative of the general problem. Instability under thermal stress and electrical fields are expected to have similar kinetics. [**28**]

In a flat panel device, the a-IGZO channel is constantly under simultaneous stress from negative bias and back-light illumination. Thus the negative bias illumination stress (NBIS) instability is the most widely studies instability in the a-IGZO system. [**24**] As shown in Fig. 1.4(a) and (b), there is a large and slow shift of the threshold voltage under NBIS, and illumination is required to induce the instability. [**29**] Several possible mechanisms have been proposed to explain NBIS instability, including surface interaction with ambient air, [**30**,**31**] photo-ionization inducing oxygen vacancies in the thin film, [**26**, **32**] and carrier trapping at the interface. [**33**] The overall response might be a combination of all those mechanisms. [**24**]

Though many works have tried to reduce NBIS instability using empirical methods such as annealing and passivation, [**20**, **24**, **33**–**36**] the photoresponse remains an intrinsic property of the a-IGZO thin film. Lee *et. al.* measured the transient photoresponse in a-IGZO thin films for around one day, then fitted the transient with three time constants, which was interpreted as being caused by the existence of three discrete transition energy levels. [**20**] The transient response and the fitted energy distributions are shown in Fig. 1.4(c) and (d). However, those conclusions cannot be fully supported by their experimental data for the following reasons. Firstly, the report simply assumed the dark conductivity to be the initial conductivity, and stopped the measurement before the transient curve reached an asymptotic behavior. The photoconductivity amplitude under such

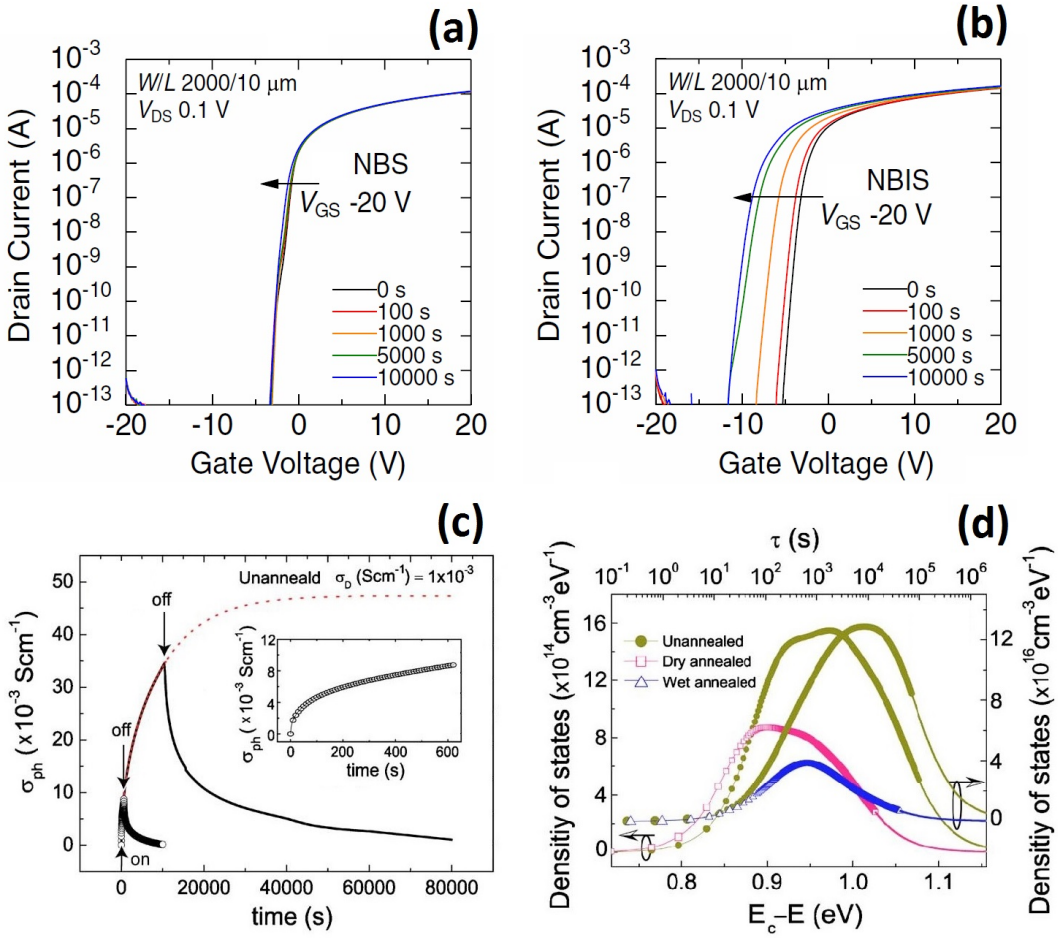

Figure 1.4. (a) I-V curve as a function of negative-bias stress (NBS) time in an a-IGZO based TFT. (b) I-V curve as a function of negative-bias illumination stress (NBIS) time in an a-IGZO based TFT illuminated by white light. There is only a small threshold voltage shift under NBS in (a) and a very large threshold voltage shift under NBIS in (b). (c) Transient photoconductivity data obtained by 3.1 eV photo excitation on an unannealed a-IGZO thin film. Inset shows an zoom-in view of the initial transient under illumination. Note the illumination was stopped before reaching the saturation conductivity. (d) Density of trap states associated with the slow photo response in a-IGZO thin films assuming a distributed activation energy model. Panels (a) and (b) are adapted from reference [**29**], and panels (c) and (d) from reference [**20**].

an incomplete dataset can be significantly underestimated. Secondly, the fitting with 3 discrete time constants was tentatively argued as being cause by three different defect complexes, one at each energy. However, a continuous time constant distribution is expected in amorphous systems, and if there are any discrete energy scales, they would be significantly broadened by inhomogeneities. Thirdly, the proposed time constants were directly related to the assumption of a standard activation energy model for trap states. This assumption of a distributed activation energy model, is not the only possibility, and it is exactly what will be re-examined for the case of the a-IGZO system in the present work.

This work will discuss transient photoresponse in a-IGZO thin films, focusing on how it can be fully characterized and modeled. A complete description of the overall photoresponse will help to identify an alternate candidate for the underlying physical mechanism, and may inspire new approaches to eventually solve the longstanding instability problem.

1.4. Thesis outline

In Chapter 2, the standard experimental methods for a-IGZO sample preparation and characterization will be reviewed, and experimental results of instability due to gate bias, thermal stress, and illumination will be presented. Based on the observed transient photoresponse features, several improvements to the standard measurement methods are presented in Chapter 3. Notably, a heterodyne Hall circuit is invented for fast and accurate Hall measurements. It allows the transient of carrier density to be measured in a-IGZO for the first time, to our knowledge, permitting the transient mobility to be separated from the transient carrier density in transient photoconductivity. This method also extends

the lower limit of the measurable mobility of the Hall effect. A modular time division multiplexer is also designed and built, allowing simultaneous transient photoconductivity measurements in several a-IGZO thin films over a time scale from $\sim$ 30 ms to 4 months, much wider than any previous reports. Chapter 4 introduces a mathematical method to analyze general non-exponential transients. By plotting the response transients on a semi-log plot, the transients are shown to be the convolution of the time constant distributions and a simple exponential decay. Therefore, the minimum measurement duration needed to accurately characterize a transient is identified as the inflection point on the semi-log plot. An empirical way to estimate the time constant distribution directly from the semi-log plot is also introduced. Chapter 5 will discuss the stretched exponential function that provides the best fitting to transient photoresponses in a-IGZO. Two possible physical models – the distributed activation energy model and the continuous time random walk model – that can explain the stretched exponential transients are reviewed and compared. A possible microscopic mechanism to explain stretched exponential responses in a-IGZO will also be developed.

CHAPTER 2

General properties and transients of a-IGZO

This chapter discusses general properties of the amorphous In-Ga-Zn-O thin films. Section 2.1 explains how a-IGZO thin films are prepared, and Section 2.2 shows how the samples are patterned and encapsulated for electrical measurements. Section 2.3 reviews the traditional measurement methods for electrical properties such as conductivity, carrier density, and mobility. The measurement results using those methods are shown in Section 2.4. For a-IGZO thin films, transient responses due to gate bias, thermal stress, and illumination have been observed. Section 2.5 focuses on illumination-induced transients, and shows our first round of transient photoresponse results using methods discussed in Section 2.3. Based on the observed photoresponse features, several improvements to the traditional measurement methods will be presented in Chapter 3.

2.1. Thin film growth

The first step for a-IGZO study is thin film growth. The most common growth methods are pulsed laser deposition (PLD) and sputtering. Both PLD and sputtering are physical deposition methods that use one or more pre-made precursor targets of a given stoichiometry to deposit a-IGZO thin films on the substrates. PLD is commonly used for prototyping a-IGZO and other AOS materials in research labs. [**4**, **14**, **37**] This method hits the target with high energy laser pulses, and the ejected target material is deposited as a thin film on the substrates. Oxides with multiple cations can be deposited using

multiple targets, where different desired stoichiometry can be easily obtained by changing the number of pulses on each target during each deposition cycle. [**38**,**39**] The pulse power is typically chosen to deposit less than one monolayer of atoms in one cycle to ensure film uniformity. Also, PLD can be conducted with the substrates at room temperature or even lower temperatures, which helps the oxides materials such as In_2O_3 to maintain an amorphous state. [**40**] For industrial fabrication, radio frequency (RF) [**41**, **42**] or direct current (DC) [**43**] magnetron sputtering is used instead. Instead of using a laser beam as in PLD, magnetron sputtering ejects the target material with energetic ions generated in a glow discharge plasma. A magnetic field is applied to confine secondary electrons near the target surface, which increases the overall deposition rate. [**44**] Magnetron sputtering allows film deposition over a large area. Uniform deposition of a-IGZO thin films over a 2.14×2.40 m^2 area using magnetron sputtering has been reported. [**1**]

When applied as the channel material in thin film transistor (TFT) devices, the thin amorphous oxide films should also have a known initial carrier density. This doping can be achieved by tuning the oxygen partial pressure P_{O_2} during PLD deposition or sputtering. [**21**, **46**] As shown in Fig. 2.1(a), carrier concentration drops with increasing P_{O_2} for PLD deposited samples. [**21**] A similar trend is also observed in sputtered thin films, [**46**] and can be attributed to suppression of oxygen vacancies with increasing P_{O_2}, since oxygen vacancies are attributed to electron generation in a-IGZO. [**19**] The stoichiometry of the target, thus the thin films, also alters the film properties. As shown in Fig. 2.1(b), In-rich samples (bottom right corner) tend to have higher carrier density and mobility, while Ga-rich samples (top corner) tend to have lower carrier density and mobility. [**10**, **21**]

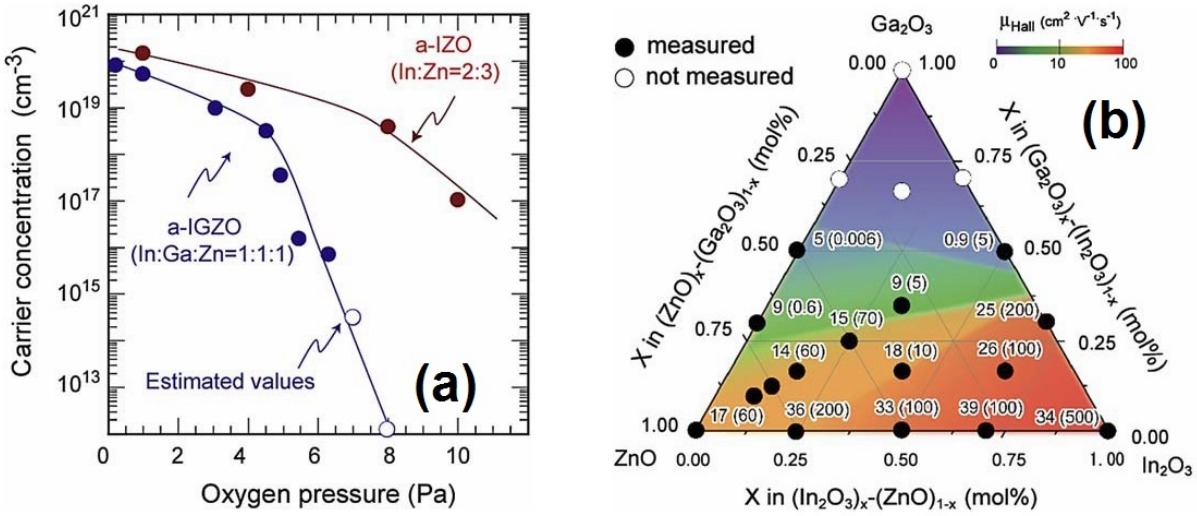

Figure 2.1. Electrical properties in the In_2O_3−Ga_2O_3−ZnO ternary system as measured by Nomura *et al.* [**45**] (a) Carrier concentration as a function of oxygen partial pressure during PLD deposition in amorphous InZnO (a-IZO) thin films and a-IGZO thin films. (b) Electron mobilities and concentrations measured from the Hall effects for PLD-grown amorphous thin films in the In_2O_3−Ga_2O_3−ZnO ternary system. The values in (b) denote the electron Hall mobility (cm^2/Vs) with density (10^{18} cm^3) in parentheses.

In recent years, solution-processed amorphous oxide thin films are receiving increased attention for their potential in cost-efficient, large-scale fabrication. By spin-coating precursor solutions on the substrates and annealing at 400 ℃, amorphous oxide thin films were successfully formed as reported by Kim *et al.* [**47**] To be compatible with flexible organic substrates, the annealing temperature can be lowered to only 250 ℃ by adding "fuels" in the precursor solutions to trigger a self-heating combustion reaction. [**48**] Yu *et al.* further optimized the combustion process by spraying the precursor solutions on heated substrates. [**49**] Such a spray process can readily adapted to high-throughput roll-to-roll fabrications. And amorphous oxides based thin film transistors prepared by the

spray combustion synthesis have already achieved performance as good as those fabricated by optimized magnetron sputtering. [**49**]

2.2. Sample preparation

In this work, we will be focusing on PLD-grown a-IGZO thin films. PLD-grown thin films used in this work are provided by D. Bruce Buchholz and Woongkyu Lee from Prof. Chang's group at Northwestern University. During PLD deposition, a 248 nm KrF excimer-laser with a 25 ns duration, operated at 2 Hz and a beam energy set to 200 mJ/pulse is used. The beam is focused to a 1 mm $\times$ 2 mm spot on the target material. For consistency, a dense, hot-pressed, ceramic $InGaO_3(ZnO)_2$ (In:Ga:Zn = 1:1:2) target is used in all following experiments. To prevent localized heating, the target is rotated at 5 rpm and the laser beam is rastered. The substrates used are either fused quartz slides, or Si slides with 300 nm SiO_2 on top. The target-substrate separation is fixed at 10 cm. Thickness is controlled by the total number of deposition cycles, and measured using a spectral reflectometer (Filmetrics F20).

For electrical property measurements, the thin films are connected to measurement instruments through wires contacted by a cold-pressed drop of indium (In). In is used to ensure good ohmic contacts with a-IGZO, because its work function, $W_{\mathrm{In}} = 4.08$ eV, is slightly lower than the electron affinity in a-IGZO, which is $\chi_{\mathrm{a-IGZO}} = 4.2 \sim 4.3$ eV. [**50**, **51**] Common metals like gold ($W_{\mathrm{Au}} = 5.10$ eV), nickel ($W_{\mathrm{Ni}} = 5.24$ eV), and chromium ($W_{\mathrm{Cr}} = 4.60$ eV) all have work function that is too high to form good Ohmic contacts with a-IGZO. For fabrications that involve patterning of the electrodes, deposited aluminum ($W_{\mathrm{Al}} = 4.28$ eV) can form good Ohmic contacts, [**52**] though it will be easily

oxidized when exposed to air. Previous reports also used highly conductive AOSs such as amorphous InSnO (a-ITO) [**4**] and amorphous InZnO (a-IZO) [**42**] to make Ohmic contacts with a-IGZO.

To separate the effects that originate from a-IGZO itself and those caused by exposure to ambient air, some samples are also encapsulated immediately after the PLD deposition, by putting quartz slides on top and sealing the surrounding edges with epoxy. The encapsulated samples will labeled as "capped", while those not encapsulated will be labeled as "uncapped". During electrical measurements, the four corners of each capped sample need to remain accessible to make electrical contacts. Thus the thin films are patterned to the shape shown in Fig. 2.2 using Scotch tape. The tape is pasted on the substrates before the deposition to form a shadow mask. After the deposition, the tape is removed and the thin films with the desired shape are left on the substrates. Then, the top surfaces of the films are covered by UV-transparent fused quartz slides and the edges are sealed by air-tight Loctite Quick Set epoxy. Fig. 2.2 shows the schematics of the encapsulation procedure as well as the pictures of a metal film test sample. The test sample uses metal film instead of a-IGZO thin film to better illustrate the film area (since a-IGZO is itself transparent) and to test the encapsulation protocol. The sample is patterned to have a central area connected with four corner areas through thin lines of the film material. The covering slide has to cover the entire central area and the epoxy can only touch the corner areas and the connecting lines. As will be explained in the next section, by putting electrical contacts on the four corners, one can measure the electrical properties of just the central area. Effects from the four corners that are not encapsulated and contaminated

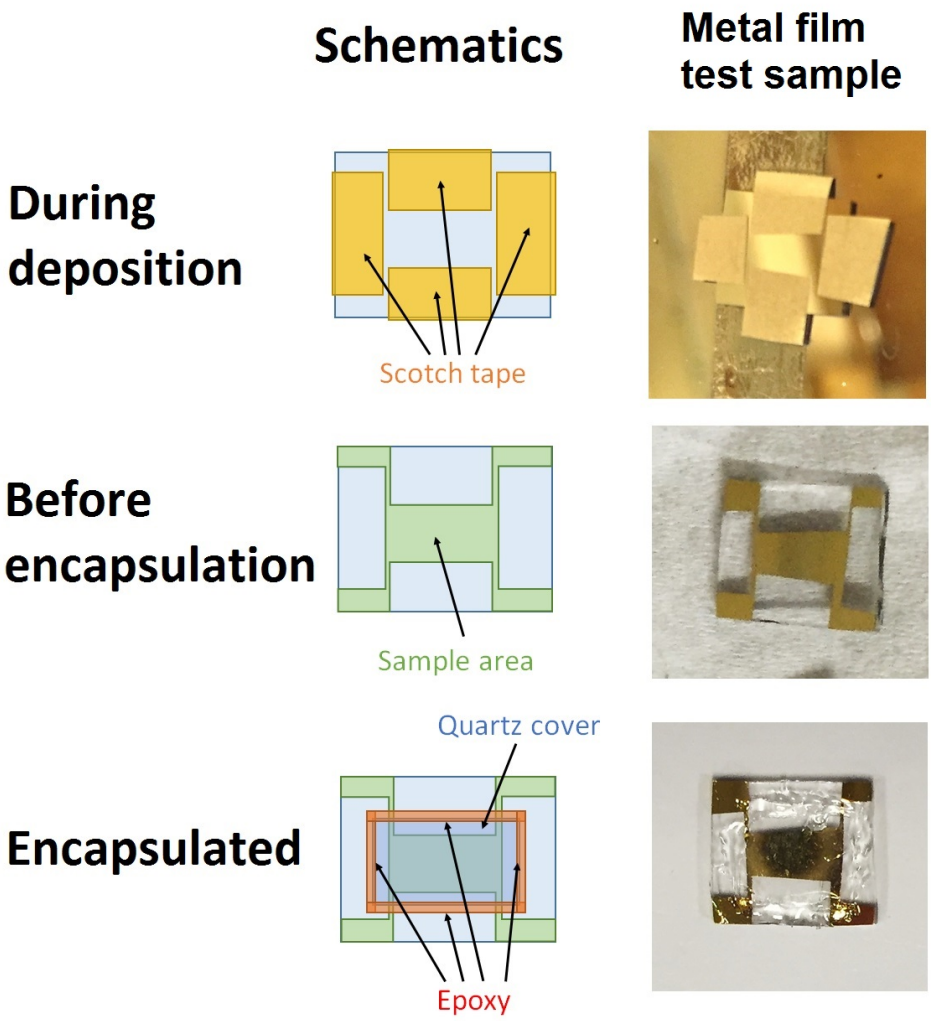

Figure 2.2. Procedure to encapsulate a thin film sample. Scotch tape covers part of the substrate during the deposition to provide the desired film pattern. The tape is removed after the deposition, then the sample is covered with quartz slide on top and sealed with epoxy on the cover edges to isolate the film at the center area from ambient air. The left column shows the schematics and the right column shows the sample pictures at each corresponding step. A metal film test sample is used to better show the film area since a-IGZO is transparent.

by epoxy will not affect the measurement results. For the uncapped samples, cold-pressed indium contacts can be directly placed on the corners or edges without patterning.

2.3. Measurement setup

This section introduces the measurement setup used in the first round measurements of the a-IGZO thin film samples. The instability response with a time scale up to one day was measured in the first round and presented in Section 2.4 and 2.5. Based those results, Chapter 3 will show improved measurement setup, as well as second round transient photoresponse results with an increased time scale up to several months.

2.3.1. Van der Pauw measurement setup

One of the most important electrical properties of a material is the electrical conductivity σ, which is measured using the van der Pauw method in this work. For a uniform thin film with thickness d, σ can be determined by measuring the sheet resistance $R_{\text{sheet}} = \frac{1}{\sigma d}$. Van der Pauw proposed a method to accurately measure the sheet resistance R_{sheet} for a uniform thin film of arbitrary shape, using 4 contacts that are sufficiently small and located on the circumference of the sample. [**53**] As illustrated in Fig. 2.3, by applying a current I_{AB} through pin A to B, and measuring the voltage difference V_{DC} between pin D and C, one can get a 4-point resistance $R_{AB,DC} = V_{DC}/I_{AB}$. Since the driving current and the voltage measurements are through different contacts, the measured 4-point resistance is unaffected by the contact resistance. Similarly, one can measure the 4-point resistance $R_{CB,DA}$. Then R_{sheet} can be calculated with Eq. (2.1).

$$R_{\text{sheet}} = \frac{\pi}{\ln 2} \frac{R_{AB,DC} + R_{CB,DA}}{2} f \tag{2.1}$$

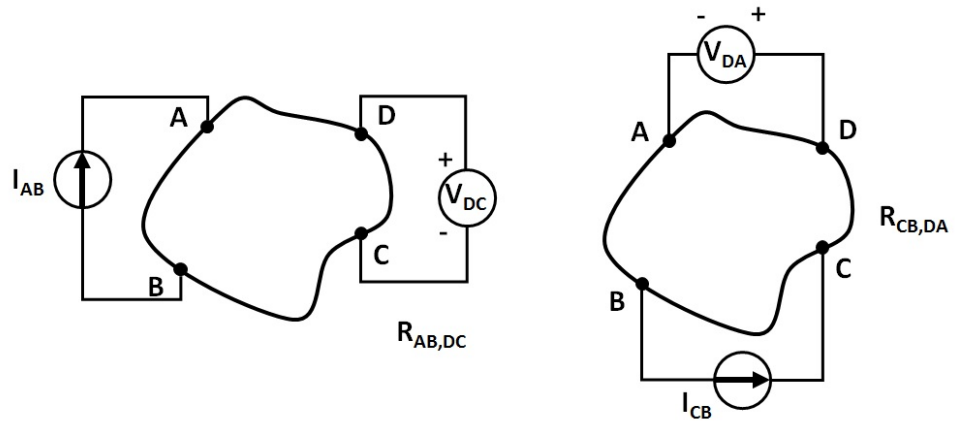

Figure 2.3. Contact configurations for the two 4-point resistances in a van der Pauw measurement. In the left configuration, by applying current I_{AB} through pin A to B and measuring voltage V_{DC} between pin D and C, 4-point resistance $R_{AB,DC}$ is measured. Similarly, in the right configuration, by applying current I_{CB} through pin C to B and measuring voltage V_{DA} between pin D and A, 4-point resistance $R_{CB,DA}$ is measured.

The geometry factor f in the above equation can be approximated by Eq. (2.2).

$$f \approx 1 - \left(\frac{R_{AB,DC} - R_{CB,DA}}{R_{AB,DC} + R_{CB,DA}}\right)^2 \frac{\ln 2}{2} - \left(\frac{R_{AB,DC} - R_{CB,DA}}{R_{AB,DC} + R_{CB,DA}}\right)^4 \left[\frac{(\ln 2)^2}{4} - \frac{(\ln 2)^3}{12}\right] \quad (2.2)$$

When $R_{AB,DC}$ and $R_{CB,DA}$ are similar in value, $f \approx 1$.

A pair of 4-point resistances need to be measured in a van der Pauw measurement. Those two resistances are typically measured in succession to switch the contacts. However, for a transient photoresponse measurement, where the thin film resistance is changing rapidly, one needs to measure the pair of resistances simultaneously. This can be achieved using the non-switching van der Pauw methods discussed in Chapter 3.

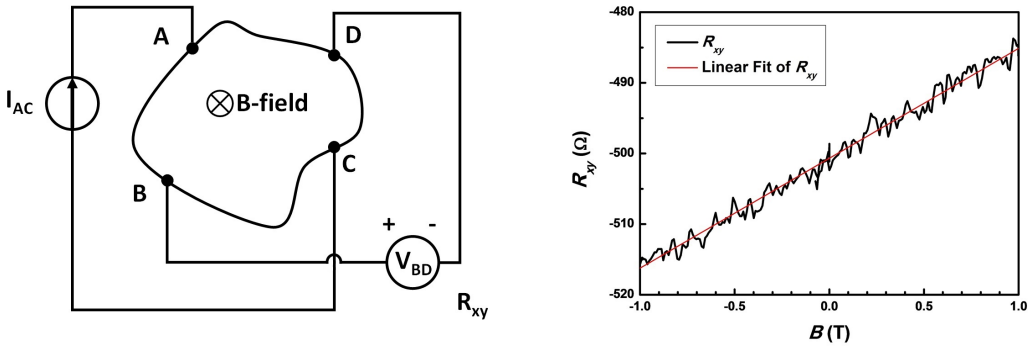

Figure 2.4. A typical Hall measurement setup (left) and measurement result for an n-type semiconductor. The magnetic field B perpendicular to the thin film is swept during the measurement. By applying a current I_{AC} through pin A to C and measuring the voltage V_{BD} between two pins B and D, the transverse resistance R_{xy} defined as $R_{xy} = R_{AC,BD} = V_{BD}/I_{AC}$ is recorded during the sweep. Carrier density and mobility are extracted using the linear fit (red line in the right panel) of R_{xy} as a function of B.

2.3.2. Hall measurement setup

Once the conductivity σ is known, it is also important to know how much of the conductivity can be attributed to carrier density n and mobility μ. In the Drude model, sample conductivity σ is determined by their product through Eq. (2.3), where e is the charge of a single electron.

$$\sigma = ne\mu \tag{2.3}$$

In typical experiments, the carrier density n is measured directly using Hall effect, then mobility μ can be calculated.

Fig. 2.4 shows a typical Hall measurement setup and the results. A current I_{AC} is applied through pin A to C, and the voltage V_{BD} between two pins B and D on difference sides of the current contacts is measured. The resulting 4-point resistance is defined as

the transverse resistance $R_{xy} = R_{AC,BD} = V_{BD}/I_{AC}$. A magnetic field B perpendicular to the thin film surface is applied and swept, during which the transverse resistance R_{xy} is recorded. The field sweep results are fitted into Eq. (2.4), in which e is the charge of a single electron, d is the film thickness, and n is the carrier density.

$$\Delta R_{xy} = \frac{\Delta B}{ned} \tag{2.4}$$

Hall measurements require the same contact setup as van der Pauw measurements. [**53**] For arbitrarily placed contacts, the measured transverse resistance R_{xy} usually has a component of the longitudinal resistance defined as R_{xx}, causing zero-field R_{xy} to deviate from 0. Thus only the slope is used for the linear fit in Eq. (2.4). Considering that the R_{xx} component varies symmetrically with field B, the difference between R_{xy} measured from the forward sweep R_{xy}^{+} and backward sweep R_{xy}^{-} is usually used to get more accurate results since the symmetric R_{xx} contribution automatically cancels. However, when the carrier density is changing rapidly during the magnetic sweep, such as during a transient photoresponse measurement, the traditional Hall measurement to be measured in a-IGZO for the first time, to our knowledge, is not appropriate. Therefore, a heterodyne Hall method designed to directly extract carrier density n or mobility μ from a single measurement at a single magnetic field B will be introduced in Chapter 3.

2.3.3. Illuminating and annealing setup

For measurements of instability under illumination and thermal stress, a light source and a temperature controller are also needed in the measurement setup. Fig. 2.5(a) shows the schematic of the setup. A UV LED light source is placed directly over the sample for

illumination, and the sample substrate is thermally connected to the thermistor and heater using a copper strip. To eliminate any influence from ambient light, all photoresponse measurements are conducted either in a tabletop aluminum dark box or an enclosed cryostat free of ambient room light. Constant current sources are used as LED power supplies to ensure constant illumination intensity during the measurements. Electrical toggle switches are used to turn on/off LEDs instantaneously. The thin film samples are contacted using the van der Pauw method described in Section 2.3.1. Then the changes of conductivity σ, carrier density n, and mobility μ over an extended time scale are measured and recorded. Over long time scales, the conductivity is measured by recording only one of the two 4-point resistances needed in the van der Pauw method, by assuming uniform photoresponse and thus a constant van der Pauw geometry factor f. The light source and the temperature controllers are implemented slightly differently between the first and second rounds of measurements, as will be described in the following.

For the first round of measurements, an apparatus shown Fig. 2.5(b) is used. A through-hole LED operating at 10 mA forward current is placed $\sim$ 2 cm above the sample for illumination, and a heater resistor is attached to the copper stripe with thermal epoxy to provide heating power. Elevated temperature is achieved by supplying a constant current to the heater, and the sample temperature is monitored using a thermistor thermally attached to the copper stripe. The whole apparatus is placed inside an aluminum box or a cryostat to provide an otherwise dark environment.

A dedicated sample chamber is designed for the second round of measurements. As shown in Fig. 2.5(c), a high power UV LED is used as the light source. The high power LED, which operates at a forward current of 700 mA, provides an illumination intensity

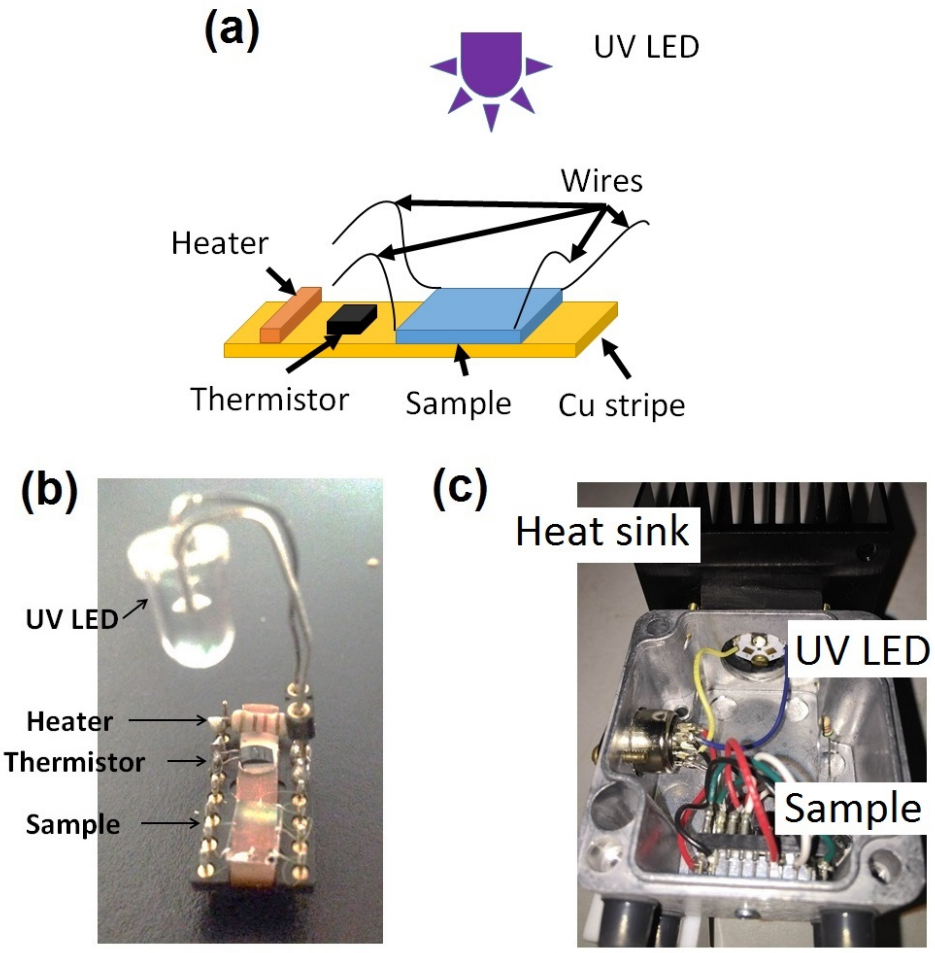

Figure 2.5. Experiment setup for the illumination and annealing measurements. (a) Schematic setup of illuminating and annealing a sample. The sample is illuminated with a UV LED placed on top, and annealed with a temperature controller unit thermally attached to the sample through a copper stripe. The sample is electrically contacted using the van der Pauw configuration for electrical measurements. (b) Setup during the first round of measurements. A through-hole UV LED is used as light source. Temperature is controlled with a heater resistor and monitored with a thermistor. (c) Sample chamber used in the second round or measurements, with 1. a high-power UV LED to illuminate the sample, 2. a sample holder directly under the LED and thermally attached to the aluminum box, and 3. an aluminum heat sink to dissipate LED heat.

much stronger than that used in the first round. To prevent heating the sample, the LED is directly mounted on a heat sink, and the heat sink is constantly cooled by an external fan. As we tested with a thermistor on the sample holder, temperature increase caused by LED heating was less than 0.5 K. Heater resistors are not utilized in the second round of measurements, but the sample temperatures are continuously monitored using thermistors thermally attached to the samples.

2.4. Electrical properties

This section and the next section show the first round measurement results. General electrical properties of the a-IGZO thin films deposited by PLD at various P_{O_2} will be presented in this section, and the characteristics of illumination-induced responses will be discussed. Various signatures of instabilities in gate bias stress and thermal stress are highlighted.

2.4.1. Carrier density and mobility at various P_{O_2}

For 200 nm thin films deposited at P_{O_2} = 5, 10, and 15 mTorr, the initial carrier density n and mobility μ are measured by Hall measurements, as shown in Fig. 2.6. All samples are determined by Hall effect to be n-type semiconductors. There is a general trend of exponentially decreasing carrier density n with linearly increasing P_{O_2} in Fig. 2.6(a). Also, for the pristine samples right after deposition, there is a trend of weakly increasing mobility μ with exponentially increasing carrier density n Fig. 2.6(b). Both the measured values and the trends in our samples with stoichiometry In:Ga:Zn = 1:1:2 agree well with

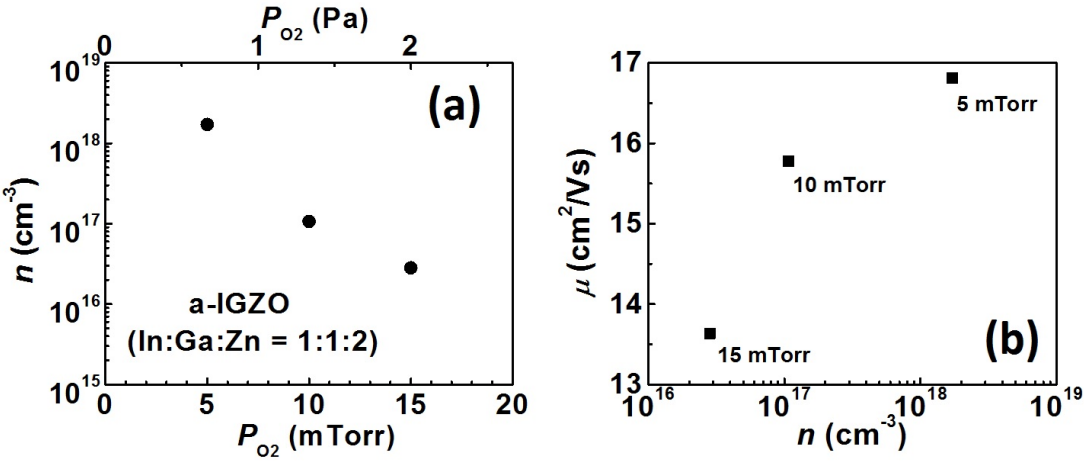

Figure 2.6. Electrical properties of pristine a-IGZO thin films right after PLD deposition. (a) Dependence of carrier densities n as a function of oxygen pressure P_{O_2} during deposition. (b) Dependence of initial electron mobility μ as a function of initial carrier density n for pristine samples deposited at different oxygen pressure P_{O_2}. Note that mobility μ is only increasing linearly by less than 25% when carrier density n increases exponentially by two orders of magnitude.

that shown in Fig. 2.1(a), reported for a-IGZO thin films with stoichiometry In:Ga:Zn = 1:1:1. [**21**]

2.4.2. Gate voltage dependence, hysteresis, and threshold instability

In thin film transistor (TFT) applications, the electrical conductivity of the a-IGZO thin films are controlled through a gate voltage bias. This requires a low intrinsic carrier density and a small film thickness. For the study of gate voltage dependence, a 50 nm PLD-grown a-IGZO thin film sample is used. The sample is deposited at a high oxygen partial pressure P_{O_2} = 18 mTorr to keep the film lightly doped. The film is deposited on a Si/SiO_2 substrate, which has 300 nm SiO_2 on top of heavily doped Si. The substrate is used as the gate terminal. The I-V curve between two contacts of the sample is plotted

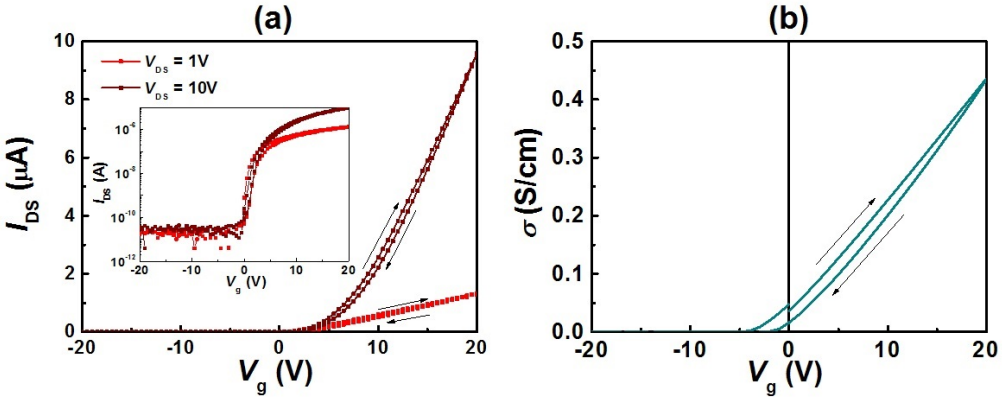

Figure 2.7. (a) Gate voltage V_g dependence of the drain-source current I_{DS} with the drain-source voltage V_{DS} = 1 V and 10 V. The inset shows the same transfer characteristic with log-scale current. The sweep rate for gate voltage V_g is 20 V/min. (b) Gate voltage V_g dependence of thin film conductivity σ. $V_{DS} = 0.1$ V was used to ensure the device was operating in the linear region. The sweep rate for gate voltage V_g is 4 V/min. The sweep directions are labeled by the arrows in both panels. Hysteresis between the up-sweep and down-sweep is observed in both measurements indicating bias-stress instability.

in Fig. 2.7(a), and the thin film conductivity measured with the van der Pauw method is plotted in Fig. 2.7(b). Without a gate bias, the thin film is highly resistive. This is expected from the carrier density dependence on P_{O_2} discussed in the previous subsection. With a large positive bias, the current I and sample conductivity σ increase almost linearly with the applied gate voltage V_g, and the slope increases linearly with the drain-source voltage V_{DS}, implying that the sample is operating in the linear region. By modeling the dielectric layer as a capacitor, the field effect transistor (FET) mobility μ_{FET} can be estimated from the relation between thin film conductivity σ and gate bias V_g through Eq. (2.5).

$$\Delta\sigma = \Delta n \cdot e \cdot \mu_{FET} = \Delta V_g C_{ox} \mu_{FET}/d \tag{2.5}$$

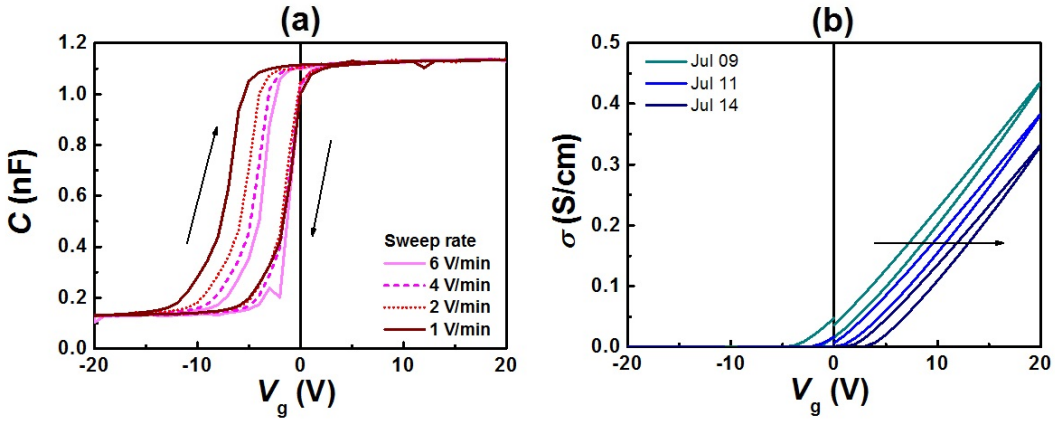

Figure 2.8. (a) Gate voltage V_g dependence of the thin film capacitance C with sweep rate of 6, 4, 2, and 1 V/min. The hysteresis increased with decreasing sweep rate. (b) Gate voltage V_g dependence of thin film conductivity σ, measured on the same sample in three different dates. The gate sweep rate was 4 V/min. The entire transfer curve shifted over days without bias stress.

The film thickness of this sample is $d = 50$ nm, and the dielectric capacitance of the 300 nm SiO_2 layer is $C_{ox} = 11.6$ nF/cm^2. Using the linear region slope $\Delta\sigma/\Delta V_g \approx 0.023$ S/Vcm shown in Fig. 2.7(b), the estimated FET mobility is $\mu_{FET} \approx 10$ cm^2/Vs, consistent with the Hall mobility of similar grown samples. With a negative bias, the film is completely depleted. No p-type conduction is observed with large negative bias, which may be attributed to a large number of trap states near the valence band. [**13**]

Unlike ideal TFTs with fast responses, the a-IGZO thin films also show slow responses during gate operation. There is a small hysteresis in the transfer characteristics in Fig. 2.7, as indicated by the arrows. The hysteresis effectively causes a threshold voltage V_{th} difference between up-sweep and down-sweep. Such a threshold shift becomes more obvious in the capacitance-voltage (C-V) measurement in Fig. 2.8(a). The C-V measurement is conducted using a 17 Hz AC voltage of 0.01 V amplitude added on the DC gate bias V_g.

V_g is swept at different sweep rates, and the AC current between the back-gate and the sample contacts is measured every 1 V during the sweep. As shown in Fig. 2.8(a), with decreasing sweep rate, the hysteresis become stronger when sweeping from a negative bias to a positive bias.

The hysteresis can be attributed to instability caused by negative bias stress (NBS). NBS instability is a major challenge for amorphous oxide applications in display devices, because the amorphous oxide TFT transistors are under negative bias over 90 % of a typical operation cycle. [**24**] The origin of NBS instability is often attributed to holes trapped at the gate insulator interface. [**24**, **35**, **54**, **55**] With a negative bias, holes are attracted to the interface, and trapped by hole traps at the interface. With a positive bias, holes release from the traps are depleted from the interface by the electrical field. This leads to the hysteresis observed between up-sweep and down-sweep. Many reports have tried to reduce NBS instability using gate insulator materials with less interfacial trap states. [**35**, **56**]

An extremely slow threshold voltage V_{th} shift is also observed for this sample when stored without gate-bias stress. As shown in Fig. 2.8(b), there is a slow and steady shift of the whole transfer curve over several days. This is probably due to photoconductivity since the sample was initially exposed to UV illumination during PLD growth and kept in dark afterwards. Gate bias sweep does not stop or reset this V_{th} shift, suggesting that instability under illumination and gate bias are caused by different mechanisms.

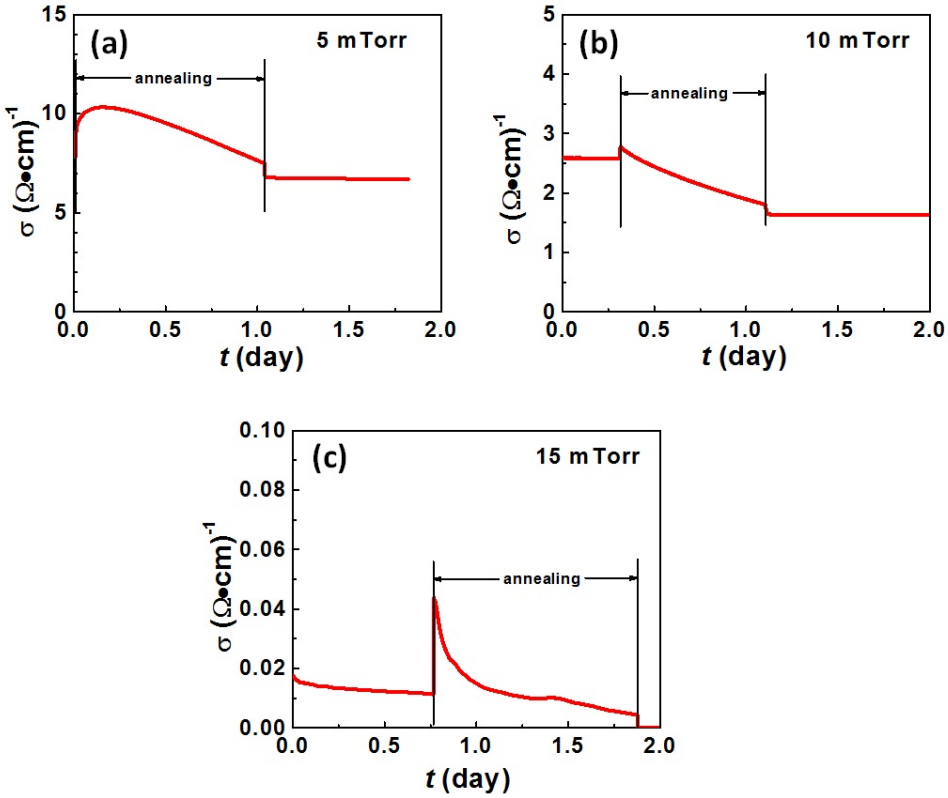

Figure 2.9. Conductivity transient during and after 80 ℃ annealing on desktop in a dark environment for 200 nm a-IGZO thin films. The samples were deposited by PLD at P_{O_2} = (a) 5 mTorr, (b) 10 mTorr, and (c) 15 mTorr. Even though the samples showed different transients during annealing, all samples had decreased conductivity after about a day of annealing.

2.4.3. Effects of annealing on conductivity stability

For as-deposited a-IGZO thin films, it has been proposed that defect states near the electron mobility edge can be reduced through an annealing process. [**14**] To study the effect of annealing, the 200 nm samples were annealed in the dark and in ambient air at 80 ℃ (350 K) for around 1 day, while the conductivity was measured, as shown in Fig. 2.9. For the 5 mTorr sample, the conductivity kept increasing for several hours before an

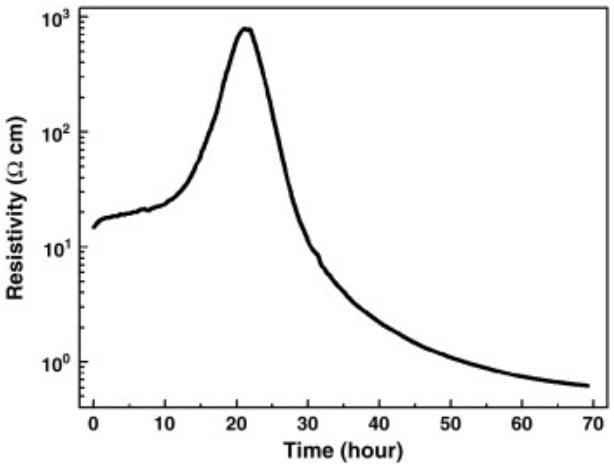

Figure 2.10. In-situ resistivity change in a 100 nm a-InZnO thin film during 200 ℃ annealing, as measured by Lee et al. [**57**] The resistivity was increasing initially and started to decrease after $\sim$ hours of annealing.

overall net decrease. For the 10 mTorr and 15 mTorr samples, conductivity only increased for a few minutes when the annealing started. All samples showed a long-term decrease of conductivity during the annealing process.

The overall reduction in conductivity after annealing may be due to oxidization of oxygen vacancies by ambient air during the annealing, which then reduces carrier density. [**14**] However, multiple physical processes might happen simultaneously during the annealing. Lee *et al.* measured the opposite sign of resistivity change in an related a-InZnO thin film during 200 ℃ annealing for 70 hours, and observed a resistivity peak (as opposed to our *conductivity* peak) followed by a slow resistivity decrease at long time scale, as shown in Fig. 2.10. The eventual conductivity increase in their work was attributed to carriers generated in the slow local structure relaxation. [**57**]

2.5. Characteristics of photoresponse and photo-instability

Besides instability under bias stress and thermal stress, a-IGZO thin films also shows instability under illumination. This section discusses the important characteristics of illumination induced instability in a-IGZO system, including its dependence on illumination wavelength, deposition oxygen pressure, and annealing statues. It is also observed that mobility remains constant for each sample during illumination and relaxation even through conductivity can change by orders of magnitudes.

2.5.1. Wavelength dependence

To study the dependence on illumination wavelength, a 140 nm P_{O_2} = 15 mTorr a-IGZO thin film sample was illuminated using red (630 nm), green (565 nm), blue (430 nm) and UV (405 nm) LEDs in an otherwise dark environment. As shown in Fig. 2.11, significant photoresponse was only observed under blue and UV illumination, whose photon energy is $\sim$ 3 eV. Reports on the wavelength dependence in a-IGZO based TFT transfer curves also showed that strong photo-induced effects only exist for wavelength smaller than 420 nm. [**58**] Therefore, we chose UV LEDs with 405 nm wavelength (3.06 eV photon energy) in the first round of measurements and UV LEDs with 385 nm wavelength (3.22 eV photon energy) in the second round of measurements. Note that even though the threshold photon energy is close to a-IGZO band-gap ($\sim$ 3 eV), [**4**] the physical mechanisms for photoresponse remains a controversial topic. Chapter 5 will review several candidate models for photoresponse in a-IGZO system.

2.5.2. Transient responses at various P_{O_2}

The transient photoconductivity of 200 nm a-IGZO thin films deposited at P_{O_2} = 5, 10, and 15 mTorr was studied. The films were illuminated by 405 nm UV LEDs for at least 24 hours and relaxed for at least 24 hours. The results are shown as the black curves in Fig. 2.12.

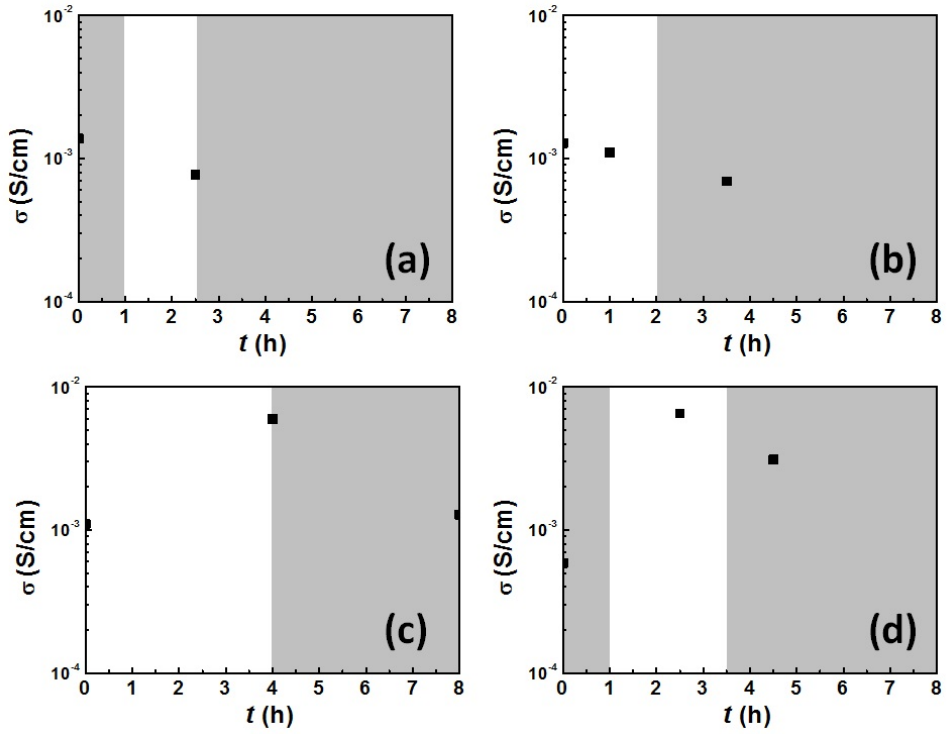

Figure 2.11. Wavelength dependence of photoresponse in a 140 nm P_{O_2} = 15 mTorr a-IGZO thin film sample. Conductivity σ versus time t under illumination with (a) 630 nm red LED, (b) 565 nm green LED, (c) 430 nm blue LED, and (d) 405 nm UV LED are shown. The areas with white backgrounds indicate the time under illumination, and the areas with gray backgrounds indicate the time in dark. Red and green LEDs show no dependence on illumination, with the same decay with time as under dark conditions. Blue and UV LEDs show an order of magnitude increase in conductivity after illumination.

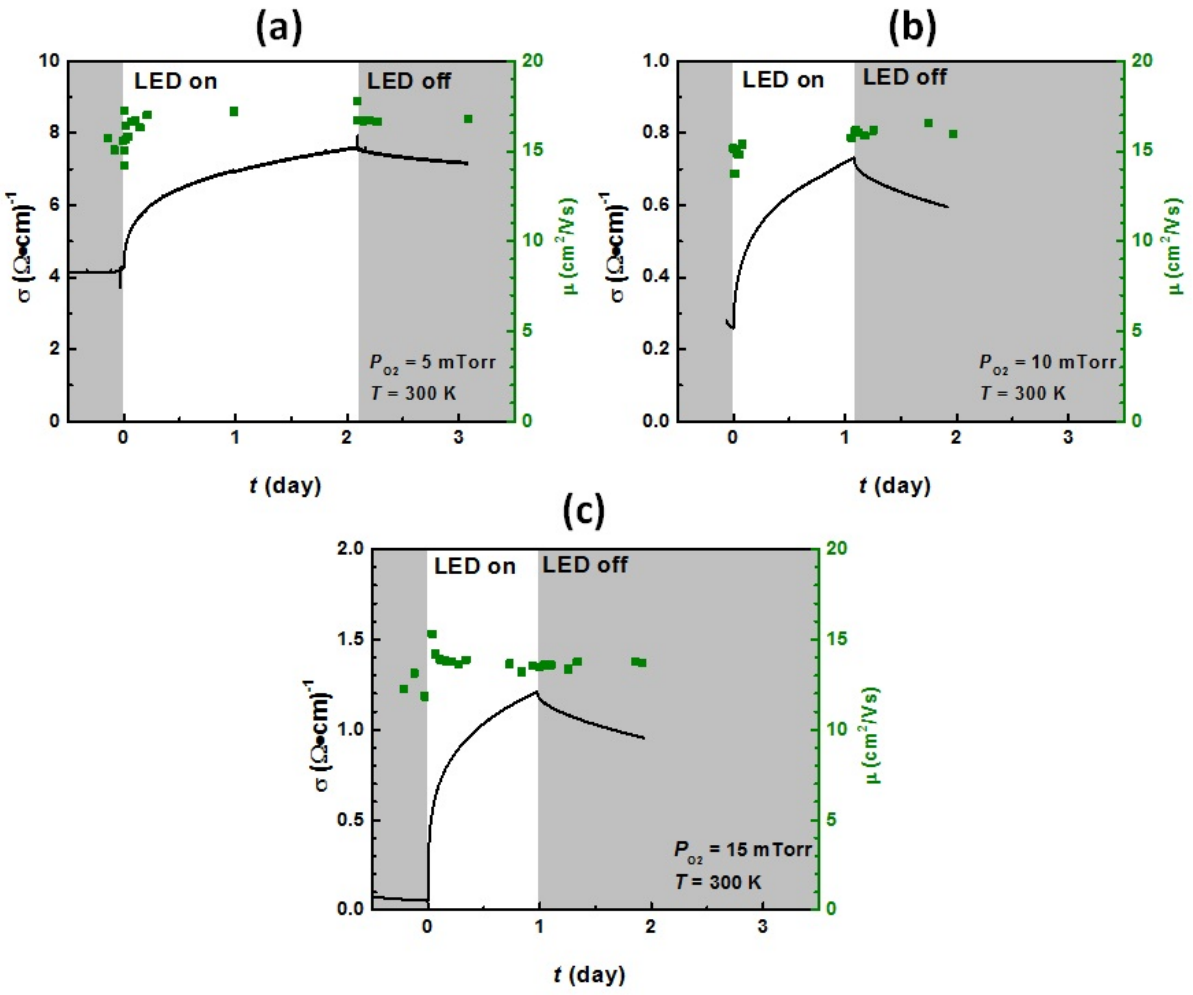

Figure 2.12. Comparison of photo-excitation and dark relaxation conductivity σ (left axis) over time t for thin films deposited at oxygen pressure P_{O_2} = 5, 10, and 15 mTorr for panels (a), (b), and (c), respectively. All measurements were conducted at room temperature in a He-flow cryostat. The conductivity measurement was briefly interrupted and the Hall mobility was measured at discrete time points, as shown by the green squares (right axis) in each graph. All samples showed approximately constant mobility μ during photo-excitation and dark relaxation.

Among the three samples, the most lightly-doped sample with P_{O_2} = 15 mTorr in panel (c) shows the largest relative photoresponse, over one order of magnitude conductivity enhancement due to illumination. For all three samples, even after a whole day

of illumination, the conductivity did not reach a saturation value with the curves still showing a significant slope at the end of the day. Note in Fig. 2.12(a) how the slope barely changes between day 1 and day 2, indicating the extreme slowing of the response at long times. This is in contrast to previous works on a-IGZO which only illuminated for 3 hours – insufficient time to characterize the time dependence of the illumination behavior [**20**] – or on related crystalline ZnO films which revealed what appears to be a stretched exponential behavior during illumination that the authors of that work neither explicitly mention nor analyze. [**59**] In the dark relaxation, the sample conductivity for all three samples did not reach a steady-state value after a whole day. As can be seen in Fig. 2.12, the rate of photoconductivity change under dark relaxation appears to be significantly slower than the corresponding change during UV excitation rate for each sample.

2.5.3. Mobility stability during illumination

During the photoconductivity measurements, the data collection was interrupted occasionally for Hall effect measurements to determine the free carrier density. By sweeping magnetic field between -2 T to 2 T, the electron density n at that time was determined. The mobility μ was deduced and plotted as a green square in Fig. 2.12. For the 5 mTorr sample, mobility increased slightly from ∼16 cm^2/Vs before illumination to ∼17 cm^2/Vs during and after illumination. Similarly, mobility of the 10 mTorr sample increased slightly from ∼15 cm^2/Vs to ∼16 cm^2/Vs under illumination, and mobility of the 15 mTorr sample increased slightly from ∼13 cm^2/Vs to ∼14 cm^2/Vs. Due to the finite time for the magnetic field sweep, measured mobilities tend to have large error shortly

after the LED was switched on or off, when carrier density was changing rapidly. Even with this error, mobility was mostly constant to within a standard deviation of 5% for each sample, whereas conductivities changed up to orders of magnitude. Therefore, the large changes in conductivity can be attributed principally to changes in carrier density, and the mobility can be assumed approximately constant. In the discussions of the following chapters, we will assume the mobility of each sample is a constant throughout the measurement.

2.5.4. Effect of annealing on photoresponse instability

Thermal annealing of amorphous oxide thin films has been widely observed to improve device stability in that decay amplitudes are reduced and decay time constants tend to be slower. [**60**–**62**] By measuring sub-gap density of state distribution through optical absorption and x-ray photoemission spectroscopy, Kamiya and Nomura *et al.* suggested that the improved stability is due to decrease of sub-gap defect states during annealing. [**17**, **63**]

Heating up the thin films should increase the rate of any thermally activated processes, but may also promote reactions which alter the chemistry and/or stoichiometry of the films, as shown in section 2.4.3. Photoconductivity curves during both illumination and dark relaxation were measured, under as-grown (300 K), annealing (350 K), and post-anneal (300 K) conditions, where each sample was annealed in 350 K for two days in a He-filled cryostat. Fig. 2.13 shows the results for the same 200 nm a-IGZO samples used in Fig. 2.12. For all those samples, the elevated temperature during the anneal is observed to enhance both the photo-excitation and dark relaxation amplitudes and rates. When

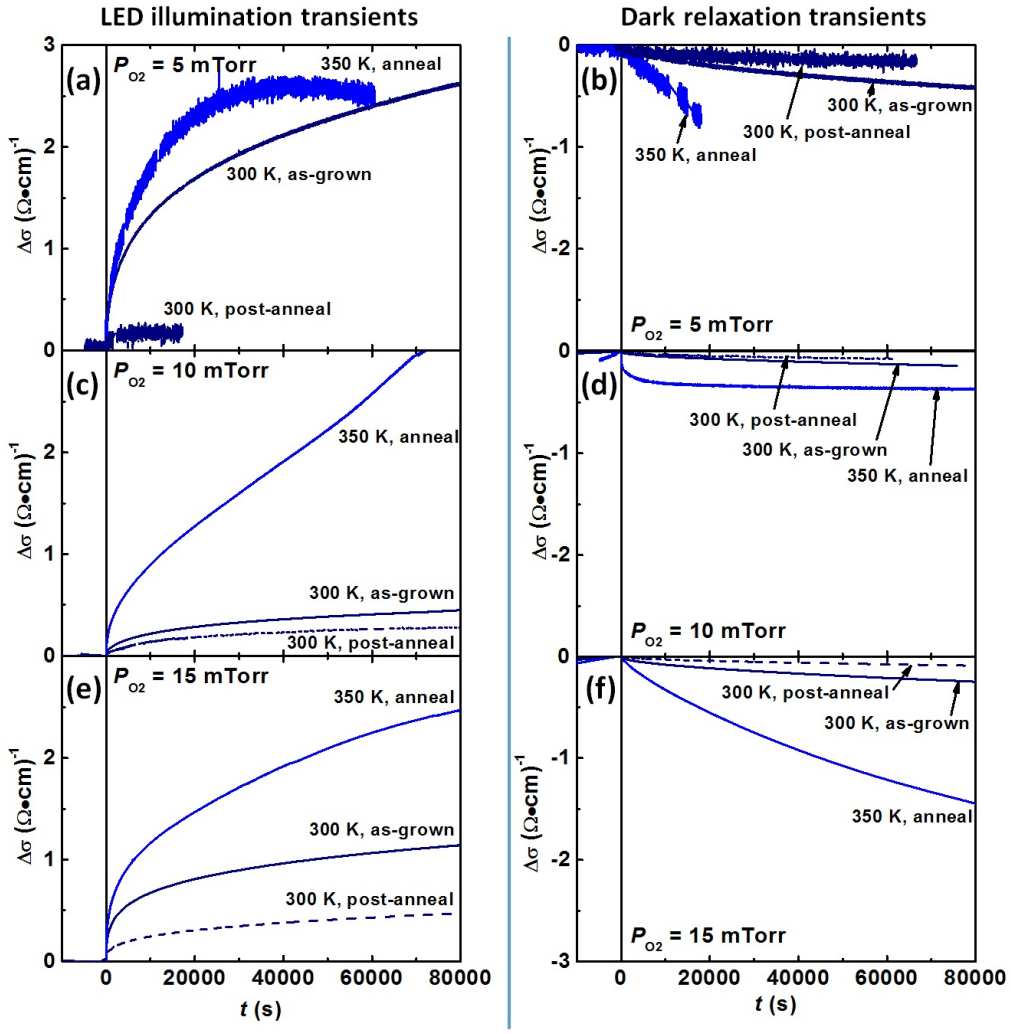

Figure 2.13. Comparison of the photoresponses under as-grown, anneal, and post-anneal states in a-IGZO thin films. The left column (a), (c), and (e) are LED illumination transients and the right column (b), (d), and (f) are dark relaxation transients. The first row (a) and (b) are the transients in the $P_{O_2} = 5$ mTorr sample, the second row (c) and (d) are the transients in the 10 mTorr sample, are the third row (e) and (f) are the transients in the 15 mTorr sample. The transients of the conductivity $\sigma(t)$ was measured, and the relative conductivity $\Delta\sigma(t) = \sigma(t) - \sigma(t = 0)$ is plotted. The initial conductivity $\sigma(t = 0)$ was measured right before the LED was turned on or off. For all samples, enhanced photoresponses were observed during 350 K annealing, and decreased photoresponses were observed at 300 K post-anneal.

the temperature was lowered back to 300 K after annealing, both rates were suppressed, implying that the 350 K anneal resulted in changes in the thin film properties for our experiment conditions.

2.6. Summary

In this chapter, we reviewed the typical methods for sample preparation and electrical property characterization, and presented the first round of measurement results with those methods. The thin films can be prepared by either physical deposition methods such as pulsed laser deposition (PLD) and magnetron sputtering, or chemical synthesis methods such as combustion-based solution processes. The PLD-grown thin films were studied by measuring their conductivity using the van der Pauw method, and carrier density and mobility using the Hall method. The electrical properties of the a-IGZO thin films showed strong dependence on deposition oxygen pressure P_{O_2}. A large and slow instability response was also observed when the sample was under negative bias stress, thermal stress, or illumination stress. Discussions in the following chapters will focus on illumination-induced response as a representative of the general instability problems. Based on the characteristics observed in the first round of transient photoresponse measurements, a set of improvements to the existing measurement methods will be developed, and the results of a second round of transient photoconductivity measurements will be presented in the next chapter.

CHAPTER 3

Novel methods for measuring transients

This chapter shows the improvements we have made for the second generation of transient photoconductivity measurements. Section 3.1 discusses the challenges for the existing measurement methods, and the goals our new methods are trying to achieve. Section 3.2 reproduces the frequency-modulated non-switching method for measuring a pair of van der Pauw resistances simultaneously. Section 3.3 introduces a newly invented heterodyne method that measures the sum (or difference) of two four-point resistances on the same sample instantaneously without switching contacts. This heterodyne method can be applied to both the van der Pauw (resistance sum) and the Hall (resistance difference) measurements. The heterodyne Hall method allows for fast and accurate Hall measurements, so that the transient of carrier density and mobility can be measured. The heterodyne Hall method also promises increased accuracy for Hall characterization of low-mobility samples. Finally, Section 3.4 introduces a modular time division multiplexer design that allows continuous measurement of multiple samples over time-scales spanning several orders of magnitudes with minimal measurement equipment.

3.1. Need for new measurement methods

As shown in Section 2.5, the conductivity and carrier density of the a-IGZO thin films are constantly changing during and after photo-excitation, and asymptotic values can

not be reached in the time scale of days. Those unique features have presented several challenges for designing an accurate and efficient measurement setup.

(1) Simultaneous measurement of resistances

The standard van der Pauw measurement requires a pair of 4-point resistances both made using different configurations of the same four contacts. For a sample in steady-state, one can simply conduct both measurements in succession. But during a fast photoresponse, the sample resistance can change dramatically during the time it takes to switch contacts and remeasure, inducing a large measurement error. Thus one needs to measure the two resistances simultaneously without switching the contacts.

(2) Rapid measurement of Hall effect

In a conventional Hall measurement, a magnetic field sweep that takes at least 10 minutes is required to get a single data point. During a photoresponse measurement, the carrier density may have changed significantly during the Hall measurement. An improved Hall measurement method is needed to determine electron density and thus mobility in a much shorter time.

(3) Rapid and slow transients

The observed photoresponses in the a-IGZO samples exhibit transient time scales spanning from less than a second to several months. Thus a measurement setup is required that would measure fast transitions at the start of excitation/relaxation with a resolution much shorter than 1 s, then dynamically reduce resolution as the response slows down.

(4) Long-term measurements of multiple samples

The properties of the a-IGZO samples vary dramatically with different oxygen pressure during deposition and other preparation parameters. So a complete characterization of

the a-IGZO system requires measurements on many different samples, and sequential measurements of the samples would take extremely long. Thus a measurement apparatus is needed that can measure multiple samples in parallel, without sacrificing resolution for the fast initial transient response.

In the following sections, several improvements to the conventional van der Pauw and Hall methods will be presented to solve the challenges mentioned above.

3.2. Frequency modulated non-switching van der Pauw method

This section reproduces the method first proposed and demonstrated by Kim *et al.*, [**64**] and then goes beyond this work to analyze the signal interference between the two modulation frequencies. The uniformity of the photoresponse in a-IGZO thin films is also studied with this method.

3.2.1. Advantages of simultaneous van der Pauw measurement

In a standard van der Pauw measurement, a pair of 4-point resistances are required to determine the sheet resistance R_{sheet}. For samples with constant R_{sheet}, this is done by measuring with two contact configurations in succession. However, during a photoresponse measurement, where the thin film resistance could be changing rapidly, the time used to switch contacts will introduce extra error in the measurement results. One way to avoid contact switching is to use the TFT structure, where the channel length and width are pre-determined. With the known geometry, the ratio between the measured 2-point resistance and the sheet resistance R_{sheet} can be estimated. However, such a 2-point measurement cannot exclude contact resistances. Alternatively, one may assume a constant van der

Pauw geometry factor between the sheet resistance and a given 4-point resistance. Thus only one 4-point resistance needs to be recorded. This assumption requires the photo-illumination to be uniform over the entire sample, in the case of photo-induced transients. This assumption of uniformity has been verified in our experiments by measuring a pair of 4-point resistances simultaneously.

Simultaneous measurements of two 4-point resistances is achieve using frequency modulation. Kim *et al.* [**64**] proposed to use two different modulation frequencies for the two contact configurations. In principle, the driving current applied at each frequency is independent from that at a different frequency. Thus the 4-point resistance excited by the current source at each frequency can be obtained by only measuring the voltage amplitude at the corresponding modulation frequency, and the need for contact switching is eliminated.

3.2.2. Circuit design

Fig. 3.1 shows the circuit design of the frequency modulated non-switching van der Pauw method, after Kim *et al.* (Ref. [**64**]). The current I_{AB} is modulated at frequency f_1, and the current I_{CB} is modulated at frequency f_2. Therefore, $R_{\mathrm{AB,DC}}$ appears in the f_1 component of voltage V_{DC}, $R_{\mathrm{AB,DC}} = \frac{V_{\mathrm{DC}}}{I_{\mathrm{AB}}}|_{f=f_1}$. And similarly, $R_{\mathrm{CB,DA}} = \frac{V_{\mathrm{DA}}}{I_{\mathrm{CB}}}|_{f=f_2}$. For simplicity, the two longitudinal resistances will be referred to as R_{xx1} and R_{xx2}. Notice that even though the signal at each frequency is independent of those at other frequencies, the ground contact B is common for all frequencies. In our experiments, two SRS 830 lock-in amplifiers are used to provide the modulated AC input voltages, which are converted to the modulated AC currents through two constant current sources. The same lock-in

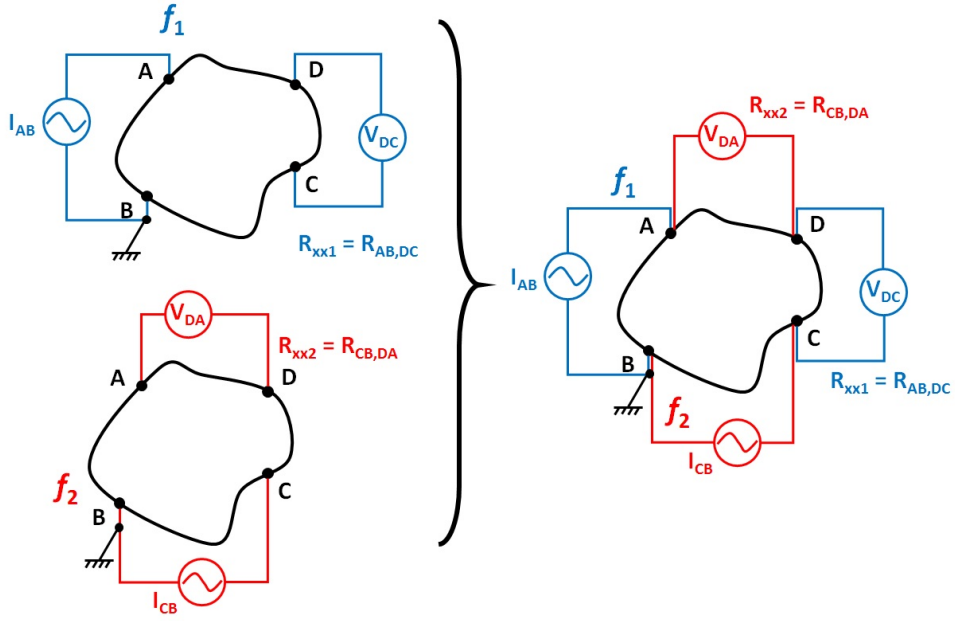

Figure 3.1. Schematic illustration of combining two van der Pauw measurement circuits of different contact configurations into a single frequency-modulated non-switching van der Pauw circuit. Note the current ground contact labeled B is shared by both frequencies.

amplifiers are used to measure the output voltages. Each lock-in amplifier only measures the signal at its reference frequency. The signals at other frequencies are ideally filtered away and non-idealities resulting in signal interference are discussed in the next section.

The functionality of this circuit has been verified on a GaAs quantum well sample. We measured the longitudinal resistances while repeatedly sweeping the magnetic field B between -5 T and +5 T at 195 K, each time with a different circuit configuration. As shown in Fig. 3.2, this non-switching van der Pauw method using $f_1 = 29$ Hz and $f_2 = 17$ Hz yields almost the same results as those measured sequentially using the standard van der Pauw method, while reducing the total measurement duration by half. A clear

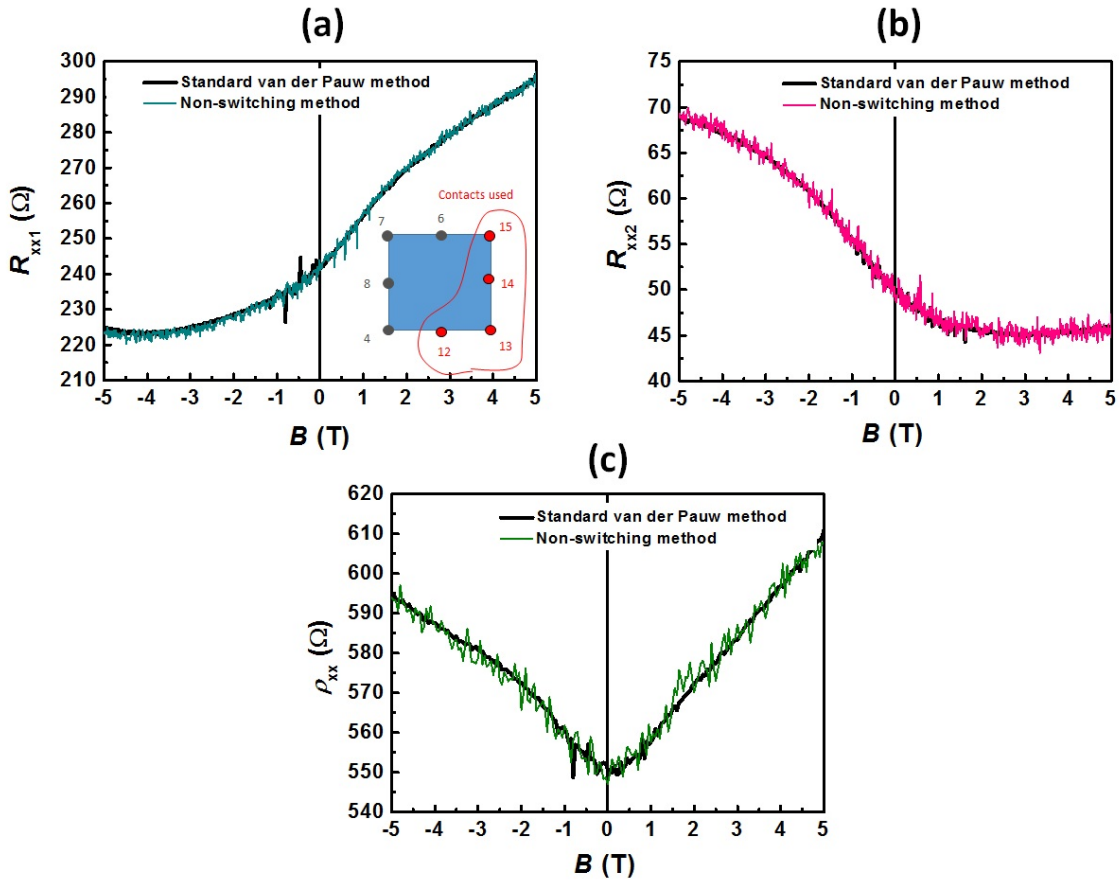

Figure 3.2. Magnetoresistance measurement results in a test GaAs quantum well sample measured by the standard van der Pauw method (thick black curves) and the frequency-modulated non-switching van der Pauw method (thin colored curves). The results shown are (a) $R_{\mathrm{xx1}} = R_{13-14,12-15}$, (b) $R_{\mathrm{xx2}} = R_{15-14,12-13}$, and (c) sheet resistivity ρ_{xx} during magnetic sweeps between -5 T and 5 T. The inset of (a) shows the contact geometry.

drawback of this non-switching method, however, is the increased noise in the signal caused by interference of the two measurement frequencies.

3.2.3. Signal interference analysis

For ideal experimental setup and lock-in amplifiers, there would be no interference between the two modulation frequencies. However, such interference is inevitable in real experiments. As shown in Fig. 3.2, the non-switching method gives significantly higher noise than sequential measurement due to this interference. The original paper by Kim *et al.* only verified the circuit correctness without discussing the interference problem. [**64**] Here we will show how the noise level can be reduced by choosing appropriate modulation frequencies and an appropriate ground contact.

The standard deviation ΔR_{xx1} and ΔR_{xx2} are used to quantify the noise level at constant magnetic field and temperature, 1 data point per second for 120 s. Separate measurements of R_{xx1} and R_{xx2} at $B = 0$ and $T = 195$ K with the same lock-in amplifiers at $f = 17$ Hz show that $R_{xx1} = 242.6\ \Omega$, $\Delta R_{xx1} = 0.13\ \Omega$, $R_{xx2} = 49.8\ \Omega$, and $\Delta R_{xx2} = 0.09\ \Omega$. Therefore $\Delta R_{xx} \approx 0.1\Omega$ is the minimum noise level we can expect from this sample in the same experiment condition, corresponding to no interference. Any increased noise level will be attributed to signal interference.

The noise level depends significantly on the choice of the modulation frequencies f_1 and f_2. Fig. 3.3(a-c) shows the noise level as various f_1 and f_2 choices. As shown in Fig. 3.3(a), with f_2 fixed at 17 Hz, increasing f_1 from 13 Hz up to 113 Hz tends to decrease the noise level. With the frequency values chosen for f_1 and f_2 swapped, the same trend is observed, as shown in Fig. 3.3(b). Similarly, with both f_1 and f_2 increased by 60 Hz such that the frequency difference remains the same, the noise level also remains the same, as shown in Fig. 3.3(c). Those trends can be explained by the design of lock-in amplifiers. When a lock-in amplifier receives a measurement signal, it first multiplies the

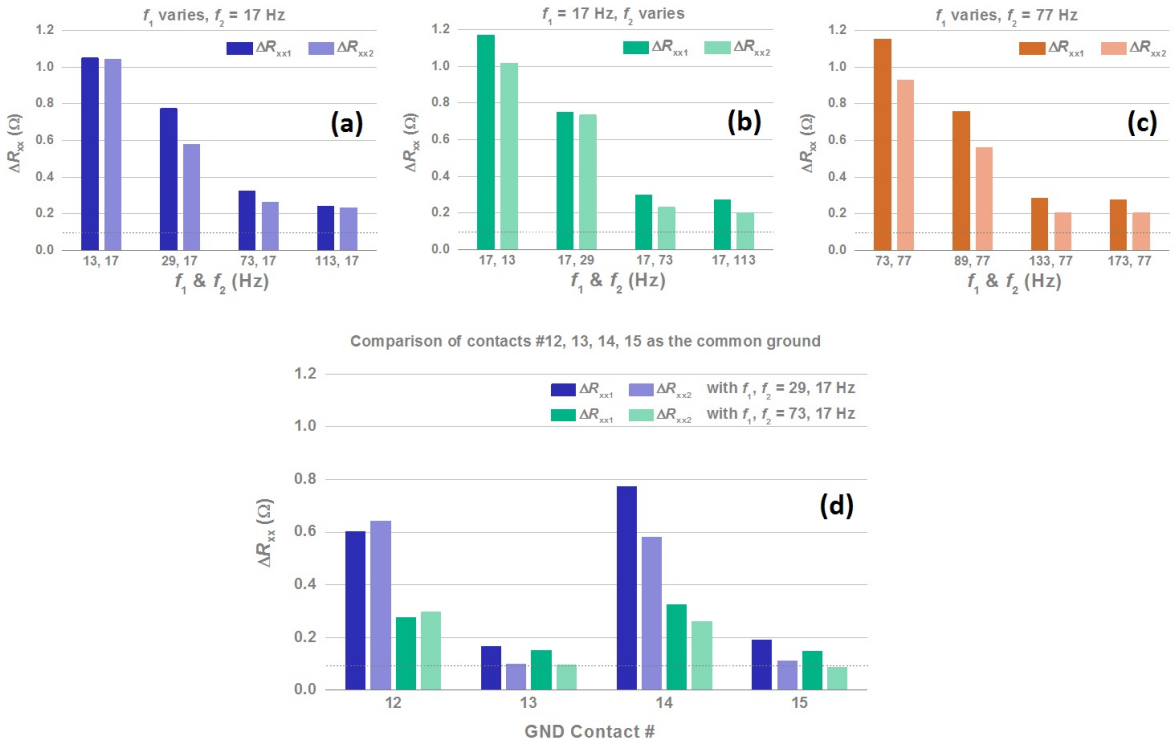

Figure 3.3. Noise level of the frequency modulated non-switching van der Pauw method measured with (a) $f_1 = 13$, 29, 73, 113 Hz and $f_2 = 17$ Hz, (b) $f_1 = 17$ Hz and $f_2 = 13$, 29, 73, 113 Hz, (c) $f_1 = 73$, 89, 133, 173 Hz and $f_2 = 77$ Hz, (d) $f_1 = 29$ or 73 Hz and $f_2 = 17$ Hz, using contact # 12, 13, 14, and 15 alternately as the ground contact. From panels (a-c), the noise level appears to depend mostly on the frequency difference $f_1 - f_2$. Panel (d) shows that the choice of the ground contact also affects the interference noise level. The contact geometry is shown as the inset of Fig. 3.2(a).

signal by a sine wave at the reference frequency, then passes the multiplied signal to a low-pass filter and measures only the DC component. [**65**] The interference is caused by the frequency components that are not effectively filtered away. Therefore, the interference level is decided primarily by the frequency difference $|f_1 - f_2|$, not the absolute value of f_1 and f_2. Only a further increase in the frequency difference would be expected to reduce the interference between the two signals.

The noise level is also affected by the choice of the ground contact. Fig. 3.3(d) shows the noise of the GaAs test sample when using different contacts as the ground. As is obvious from Fig. 3.3(d), certain ground contact choices lead to noise levels much lower than that achieved by tuning the frequencies, and the overall contribution from interference can be mostly eliminated by combining a large frequency difference with a good choice of the ground contact. The large signal interference associated with certain ground contacts might be explained by the harmonics generated when currents are flowing through a non-linear common ground contact. Thus one should test for the most linearly resistive ground contact before applying the non-switching method.

3.2.4. Test of non-switching method: uniformity of a-IGZO photoresponse

The non-switching van der Pauw method has been applied on a 50 nm a-IGZO thin film grown by PLD at $P_{O_2} = 10$ mTorr to verify whether the photoresponse is uniform across the whole sample. Any non-uniform stoichiometry might cause local variations in the relaxation time and lead to a time-varying anisotropy in the sheet resistivity. Fig. 3.4(a) shows the two measured 4-point resistances dynamically changing with time, and (b) shows the calculated sheet resistance and the ratios between the sheet resistance and the measured 4-point resistances. For a whole day of dark relaxation after steady illumination, the geometry factors $R_{\mathrm{sheet}}/R_{\mathrm{xx1}}$ and $R_{\mathrm{sheet}}/R_{\mathrm{xx2}}$ were almost constant, even though the sheet resistance R_{sheet} showed significant relaxation. Fig. 3.4(c) plots the sample conductivity calculated from both R_{xx1} and R_{xx2}, and shows the estimation error of measuring only R_{xx1} or R_{xx2} and assuming constant geometry factor. For a conductivity response around 10 %, the error of assuming a constant geometry factor is only 0.5

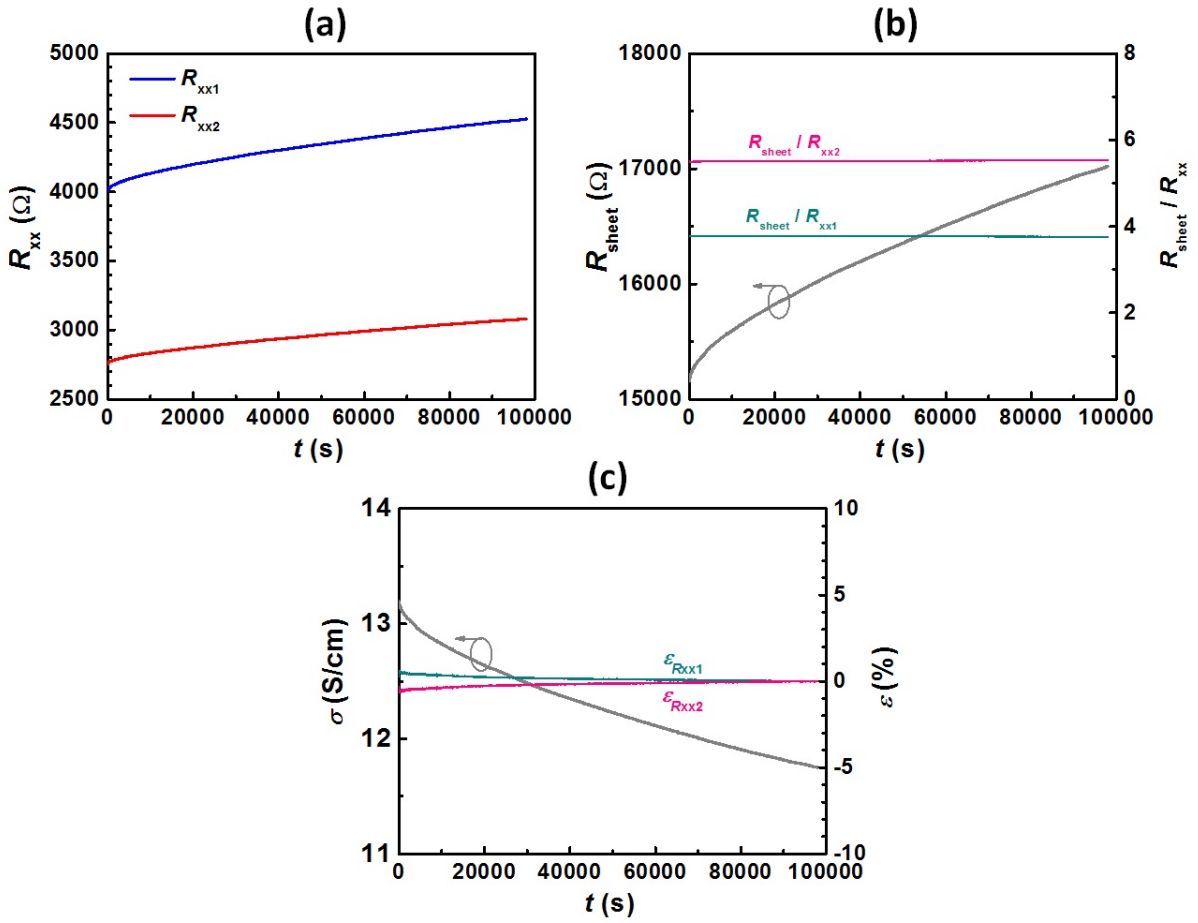

Figure 3.4. Comparison of the transients for 4-point resistances and the sheet conductivity. (a) Measured dark relaxation of longitudinal resistances R_{xx1} and R_{xx2} in a 50nm PLD-grown 10 mTorr a-IGZO thin film after UV LED illumination. (b) Calculated sheet resistance R_{sheet} and geometry factors $R_{\mathrm{sheet}}/R_{\mathrm{xx1}}$ and $R_{\mathrm{sheet}}/R_{\mathrm{xx2}}$ during the relaxation transient. The geometry factors were almost constant during the relaxation. (c) Calculated conductivity σ and the error ϵ when σ is estimated using only R_{xx1} or R_{xx2} assuming constant geometry factors. With conductivity changing by more than 10 %, the error caused by assuming an illumination-independent geometry factors was less than 1 %.

%. Therefore, for a-IGZO photoresponse measurements, one can reasonably assume a constant geometry factor, measure it either at the start or the end of the measurement,

and record the response of only one 4-point resistance to calculate the time evolution of the sheet resistance and the conductivity.

3.3. Heterodyne method for van der Pauw and Hall measurements

The non-switching van der Pauw method introduced in the last section allows for simultaneous measurement of two resistances, but it suffers from increased noise levels, and two measurement instruments are required. Here, based on the same idea of frequency modulation, we invent a new heterodyne method that can improve both measurement efficiency and accuracy. The heterodyne method works for both Hall measurements, and van der Pauw measurements, where the latter case holds provided that the geometry factor remains constant.

3.3.1. Heterodyne van der Pauw method

The heterodyne van der Pauw method directly measures the sum of two longitudinal resistances instead of measuring them with separate instruments. The circuit flow chart of the heterodyne van der Pauw method is shown in Fig. 3.5. The upper current source circuit of Fig. 3.5, similar to the frequency-modulated non-switching van der Pauw circuit, supplies modulated constant currents I_a and I_b through contact A and contact C, respectively. The lower voltage heterodyne circuit generates a single output signal V_{O} from two longitudinal voltages V_{DC} and V_{DA}, using the analog signal processing of Fig. 3.5 with adders and multipliers.

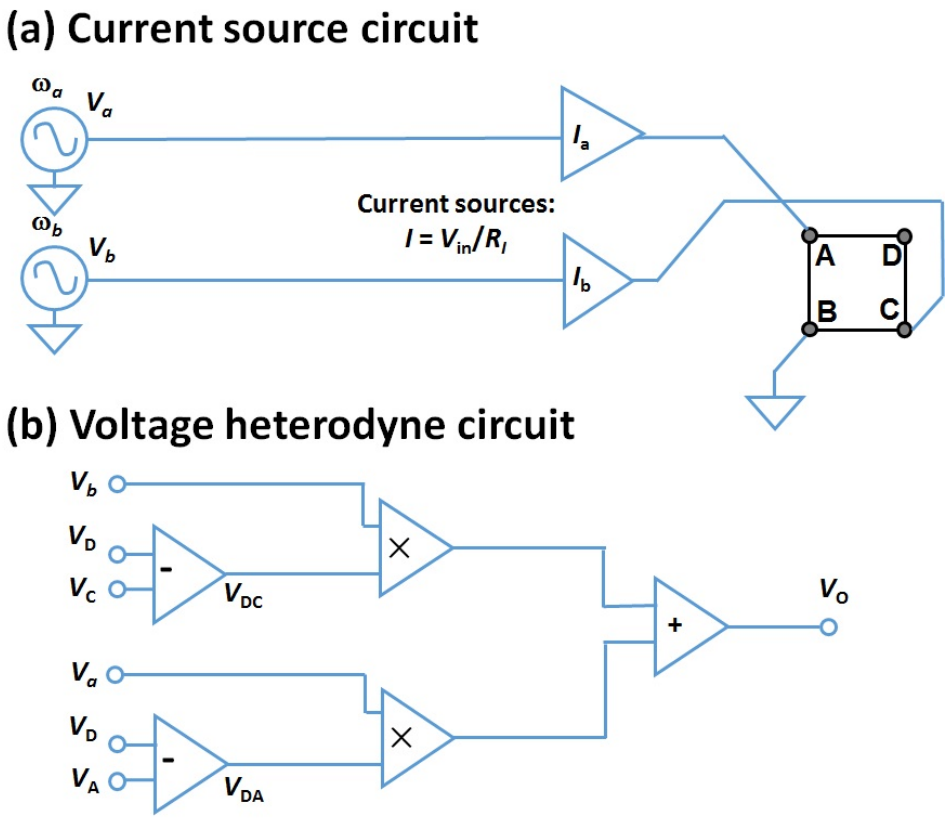

Figure 3.5. Circuit design for the heterodyne van der Pauw method. The current source circuit (a) provides the driving current I_a at frequency ω_a from contact A to B, and I_b at frequency ω_b from contact C to B. The voltage heterodyne circuit (b) generates a single output voltage $V_O = \frac{V_{DC}(t)V_b(t)+V_{DA}(t)V_a(t)}{V_R}$ through analog adders and multipliers.

Two AC voltage sources, V_a and V_b, operating at different frequencies, ω_a and ω_b, and the same amplitude, V_0, are used as signal sources.

$$V_a(t) = V_0 \cos(\omega_a t + \theta_a)$$
$$V_b(t) = V_0 \cos(\omega_b t + \theta_b) \tag{3.1}$$

The AC voltages are sent to current source circuits with reference resistance R_I, to generate input currents I_a and I_b as followed, where $I_0 = V_0/R_I$.

$$\begin{aligned} I_a(t) &= I_0 \cos(\omega_a t + \theta_a) \\ I_b(t) &= I_0 \cos(\omega_b t + \theta_b) \end{aligned} \tag{3.2}$$

Four contacts on the sample, arranged in the van der Pauw configuration, are connected to the circuit. Current I_a is supplied from contact A to B, and current I_b is supplied from contact C to B. Contact B is used as the common ground for all frequencies.

The longitudinal voltages V_{DC} and V_{DA} are therefore defined by Eq. (3.3), where $Z_{AB,DA} = \frac{V_{DA}}{I_{AB}}$ and $Z_{CB,DC} = \frac{V_{DC}}{I_{CB}}$ are the 3-point impedances that result from current through contacts AB or CB, respectively.

$$\begin{aligned} V_{DC}(t) &= I_0 \left[R_{AB,DC} \cos(\omega_a t + \theta_a) + Z_{CB,DC} \cos(\omega_b t + \theta_b) \right] \\ V_{DA}(t) &= I_0 \left[R_{CB,DA} \cos(\omega_b t + \theta_b) + Z_{AB,DA} \cos(\omega_a t + \theta_a) \right] \end{aligned} \tag{3.3}$$

They include contributions from both the thin film and the contacts, and might have capacitive components when the contacts are not ohmic. For the heterodyne van der Pauw method, the detailed compositions of $Z_{AB,DA}$ and $Z_{CB,DC}$ are irrelevant, as long as they remain constant.

The voltages excited by the current source circuit are then proceed by the voltage heterodyne circuit. The longitudinal voltage V_{DC} is multiplied by V_b, and V_{DA} is multiplied by V_a. The multiplied signals are added together to produce a single output voltage V_{O}, as given in Eq. (3.4), where V_R is the the amplitude of the reference used in the heterodyne

multipliers.

$$
\begin{aligned}
V_{\mathrm{O}} =& \frac{V_{DC}(t)\, V_b(t) + V_{DA}(t)\, V_a(t)}{V_R} \\
=& \frac{V_0^2}{2V_R R_I} \left\{ \begin{array}{l}
[\boldsymbol{R_{AB,DC}} + \boldsymbol{R_{CB,DA}}] \cos[(\boldsymbol{\omega_a} + \boldsymbol{\omega_b})\, \boldsymbol{t} + (\boldsymbol{\theta_a} + \boldsymbol{\theta_b})] \\
+ [\boldsymbol{R_{AB,DC}} + \boldsymbol{R_{CB,DA}}] \cos[(\boldsymbol{\omega_a} - \boldsymbol{\omega_b})\, \boldsymbol{t} + (\boldsymbol{\theta_a} - \boldsymbol{\theta_b})] \\
+ \mathrm{Re}(Z_{CB,DC}) \cos[2(\omega_b t + \theta_b)] - \mathrm{Im}(Z_{CB,DC}) \sin[2(\omega_b t + \theta_b)] \\
+ \mathrm{Re}(Z_{AB,DA}) \cos[2(\omega_a t + \theta_a)] - \mathrm{Im}(Z_{AB,DA}) \sin[2(\omega_a t + \theta_a)] \\
+ \mathrm{Re}(Z_{CB,DC}) + \mathrm{Re}(Z_{AB,DA})
\end{array} \right\}
\end{aligned} \tag{3.4}
$$

The output signal V_{O} has 5 frequency components. The desired value $R_{AB,DC} + R_{CB,DA}$ appears at frequency $\omega_a + \omega_b$ and $\omega_a - \omega_b$. All other signals are separated to different frequencies. Thus one only needs to measure the voltage amplitude at either frequency $\omega_a + \omega_b$ or $\omega_a - \omega_b$ to know $R_{AB,DC} + R_{CB,DA}$. In this work, the root-mean-square (RMS) amplitude at frequency $\omega_a \pm \omega_b$ of V_{O} is measured and defined as $|V_{\mathrm{out}}|$. Using the van der Pauw Eq. (2.1), the sheet resistance R_{sheet} can be calculated from V_{out} through Eq. (3.5), where the geometric factor f may be assumed to be a constant set by the sample geometry according to the standard van der Pauw method.

$$
R_{\mathrm{sheet}} = \frac{\pi}{\ln 2} \frac{[R_{AB,DC} + R_{CB,DA}]}{2} f = \frac{\pi}{\ln 2} \frac{\sqrt{2} V_R R_I}{V_0^2} f \tag{3.5}
$$

The heterodyne van der Pauw method has been verified using a 200 nm 5 mTorr PLD-grown a-IGZO thin film sample with steady electrical properties. First, the geometry factor f should be calibrated from Eq. (2.2) using the standard van der Pauw method. The two longitudinal resistance measured are $R_{xx1} = 3.67\ \mathrm{k\Omega}$ and $R_{xx2} = 1.73\ \mathrm{k\Omega}$, respectively,

giving a geometry factor is $f \approx 0.95$. Thus and the sheet resistance determined by the standard van der Pauw method is $R_{\text{sheet}} = 11.67$ kΩ. When applying the heterodyne van der Pauw method, the parameters $V_0 = \sqrt{2}$ V, $V_R = 10$ V, $R_I = 100$ kΩ, $\omega_a = 17$ Hz, and $\omega_b = 51$ Hz were used. The directly measured output amplitude at frequency $\omega_a + \omega_b = 68$ Hz is $|V_{\text{out}}| = 3.80$ mV. By plugging in those numbers and $f = 0.95$ into Eq. (3.5), the sheet resistance determined by the heterodyne van der Pauw method is $R_{\text{sheet}} = 11.7$ kΩ. Note that even though the geometry factor f needs to be calibrated before the measurements, only one output signal from the the heterodyne circuit needs to be measured to give the sum of longitudinal resistances $R_{xx1} + R_{xx2}$, thereby allowing transient resistivities to be measured, as was the goal.

Transient measurements using the heterodyne van der Pauw method have a reduced error compared to those using only one 4-point resistance. One reason is that the geometric factor f only changes slightly even with a large change of the longitudinal resistance ratio R_{xx1}/R_{xx2}. For example, for a transient response where R_{xx1}/R_{xx2} increases from 2 to 3 would only give an error ~ 5 % for the final R_{sheet} result. As a final advantage, only one measurement lock-in amplifier is needed for the heterodyne van der Pauw method.

The heterodyne van der Pauw method also allows measurements over a much wider frequency range. The previous non-switching method discussed in Section 3.2 requires both modulation frequencies to be within the lock-in frequency range, which is typically below 10 kHz, while conductivity measurements at higher frequencies are necessary for many material systems. For example, for the ionic conductor system, Almond *et al.* proposed a method to separate conductivity contributions from carrier density and hopping rate by measuring the frequency-dependent AC conductivity to 10 MHz at a few different

temperatures. [**66**] Such a high measurement frequency can be achieved using the heterodyne van der Pauw method, as long as the frequency *difference* $\omega_a - \omega_b$ is within the measurement range of lock-in amplifiers.

3.3.2. Heterodyne Hall method

The Hall effect method is the standard way to separate the carrier density n and mobility μ in the overall conductivity σ of a semiconductor material. It requires a transverse 4-point resistance to be measured in a magnetic field. In practice, it is usually not measured in a constant magnetic field but rather as the slope of a magnetic field B sweep. Since the contacts cannot be perfectly symmetric, the directly measured transverse resistance $R_{AC,BD}$ at a fixed B field usually has a longitudinal component aR_{xx} and a transverse Hall component R_{xy}, making $R_{AC,BD} \neq 0$ when $B = 0$. In the Drude model, one have $R_{xx}(+B) = R_{xx}(-B)$, and $R_{xy}(+B) = -R_{xy}(-B)$. Thus the aR_{xx} component can be eliminated by measuring at two opposite B fields, as shown in Eq. (3.6).

$$
\begin{aligned}
R_{AC,BD}(+B) &= R_{xy}(+B) + aR_{xx}(+B) \\
R_{AC,BD}(-B) &= R_{xy}(-B) + aR_{xx}(-B) \\
R_{AC,BD}(+B) - R_{AC,BD}(-B) &= 2R_{xy}(+B) + 0
\end{aligned}
\tag{3.6}
$$

The method of Eq. (3.6) as they stand still requires flipping the magnetic field. This can be avoided using the Onsager-Casimir symmetry $R_{BD,AC}(+B) = R_{AC,BD}(-B)$. [**67**–

70]. Thus the measurement can be significantly simplified, as shown in Eq. (3.7).

$$
\begin{aligned}
&R_{AC,BD}(+B) = R_{xy}(+B) + aR_{xx}(+B) \\
&R_{BD_{AC}}(+B) = R_{AC,BD}(-B) = R_{xy}(-B) + aR_{xx}(-B) \\
&R_{AC,BD}(+B) - R_{BD,AC}(+B) = 2R_{xy}(+B) + 0
\end{aligned}
\tag{3.7}
$$

The circuit implementation of this Hall effect measurement using the heterodyne 4-point method is as follows. The basic circuit design of the heterodyne Hall method is shown in Fig. 3.6, where care should be taken to notice the slightly different contact configuration compared to the heterodyne van der Pauw method shown in Fig. 3.5. The current I_a at frequency ω_a flows through contact A to C, and the current I_b at a different frequency ω_b flows through contact D to B independently. Contact C remains the ground for all signals, and current sources with output currents I_b and $-I_b$ are used to allow contacts B and D to be at any voltage.

The resulting diagonal voltages V_{BD} and V_{AC} are defined by Eq. (3.8), where $Z_{BD} = \frac{V_{BD}}{I_{BD}}$ and $Z_{AC} = \frac{V_{AC}}{I_{AC}}$ are the 2-point impedances across contacts BD and AC, respectively. Both 2-point impedances include contributions from the contacts, thus may not be perfectly ohmic. Nevertheless, the heterodyne Hall method can be applied as long as both Z_{BD} and Z_{AC} remain constant.

$$
\begin{aligned}
V_{BD}(t) &= I_0 \left[R_{xy}(+B) \cos(\omega_a t + \theta_a) + Z_{BD} \cos(\omega_b t + \theta_b) \right] \\
V_{AC}(t) &= I_0 \left[R_{xy}(-B) \cos(\omega_b t + \theta_b) + Z_{AC} \cos(\omega_a t + \theta_a) \right]
\end{aligned}
\tag{3.8}
$$

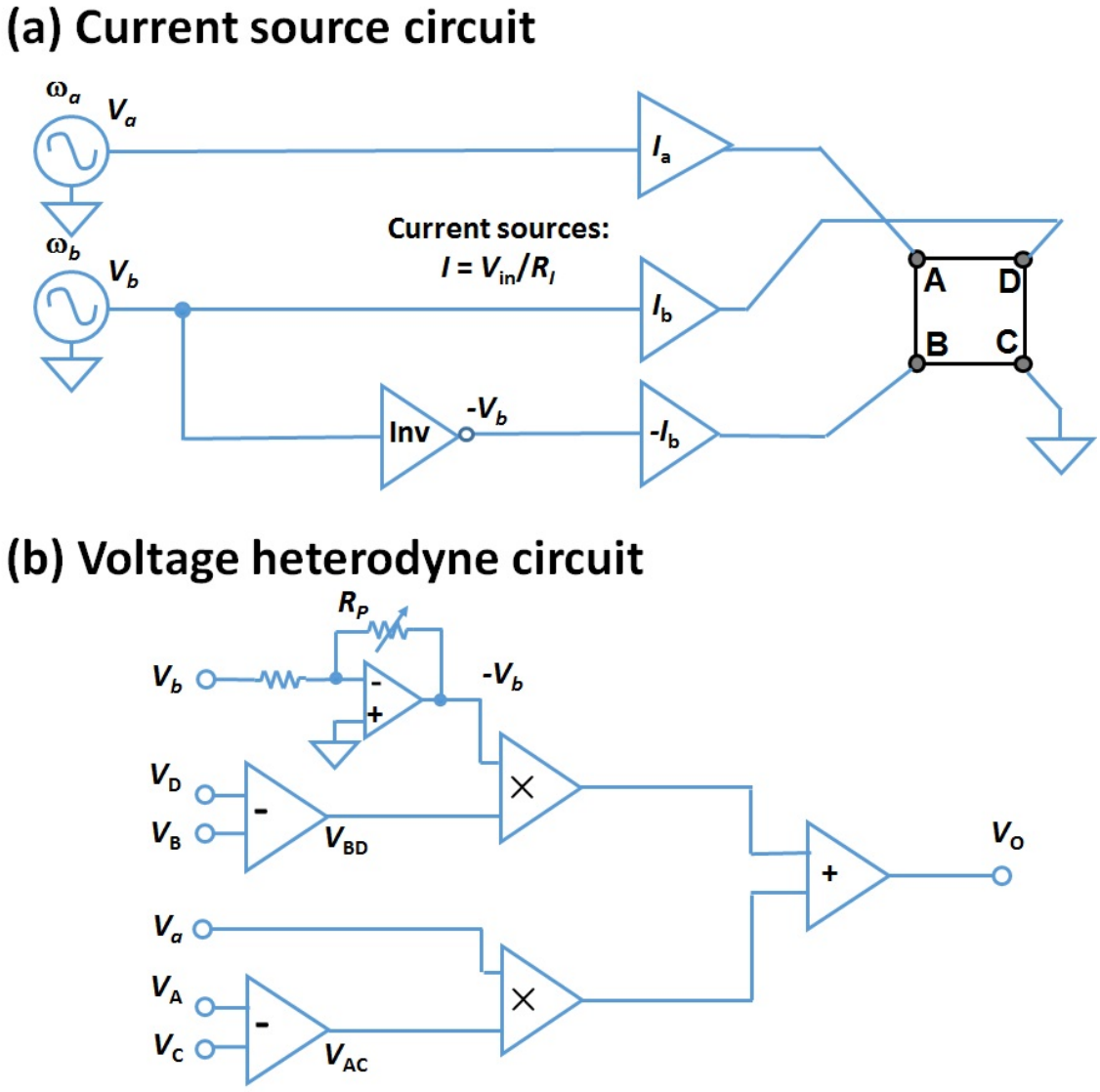

Figure 3.6. Circuit design of the heterodyne Hall method. The current source circuit (a) provides current I_a at frequency ω_a from contact A to C, and current I_b at frequency ω_b from contact D to B. The voltage heterodyne circuit (b) generates a single output voltage $V_{\mathrm{O}} = \frac{V_{BD}(t)V_b(t) - V_{AC}(t)V_a(t)}{V_R}$ through analog adders and multipliers. A calibration potentiometer R_P is included to match the amplitude of V_a and $-V_b$.

With the circuit design in Fig. 3.6, the output voltage V_O would be as following.

$$
\begin{aligned}
V_{\mathrm{O}} =& \frac{V_{BD}(t)\, V_b(t) - V_{AC}(t)\, V_a(t)}{V_R} \\
=& \frac{V_0^2}{2V_R R_I} \left\{ \begin{array}{l}
[\boldsymbol{R_{xy}(+B)} - \boldsymbol{R_{xy}(-B)}] \cos[(\boldsymbol{\omega_a} + \boldsymbol{\omega_b})\, \boldsymbol{t} + (\boldsymbol{\theta_a} + \boldsymbol{\theta_b})] \\
+ [\boldsymbol{R_{xy}(+B)} - \boldsymbol{R_{xy}(-B)}] \cos[(\boldsymbol{\omega_a} - \boldsymbol{\omega_b})\, \boldsymbol{t} + (\boldsymbol{\theta_a} - \boldsymbol{\theta_b})] \\
+ \mathrm{Re}(Z_{BD}) \cos[2(\omega_b t + \theta_b)] - \mathrm{Im}(Z_{BD}) \sin[2(\omega_b t + \theta_b)] \\
- \mathrm{Re}(Z_{AC}) \cos[2(\omega_a t + \theta_a)] + \mathrm{Im}(Z_{AC}) \sin[2(\omega_a t + \theta_a)] \\
+ \mathrm{Re}(Z_{BD}) - \mathrm{Re}(Z_{AC})
\end{array} \right\}
\end{aligned} \tag{3.9}
$$

V_O has 5 frequency components. The desired value $R_{xy}(+B) - R_{xy}(-B)$ appears at the first two terms in the bracket, frequency $\omega_a + \omega_b$ and $\omega_a - \omega_b$. All other signals occur at different frequencies. Thus, similar to the van der Pauw heterodyne method, one needs the voltage amplitude at either frequency $\omega_a + \omega_b$ or $\omega_a - \omega_b$ to know $R_{xy}(+B) - R_{xy}(-B)$. In this work, the root-mean-square (RMS) amplitude at frequency $\omega_a \pm \omega_b$ of V_{O} is measured and defined as V_{out}. Using the Hall effect Eq. (2.4), carrier density n is directly related to V_{out} through Eq. (3.10).

$$
\begin{aligned}
|V_{\mathrm{out}}| &= \frac{V_{\mathrm{O},\omega_a \pm \omega_b}}{\sqrt{2}} = \frac{V_0^2}{2\sqrt{2} V_R R_I} [2R_{xy}(+B)] = \frac{V_0^2}{\sqrt{2} V_R R_I} \cdot \frac{B}{ned}, \\
\text{Thus } n &= \frac{B}{ed} \cdot \frac{1}{|V_{\mathrm{out}}|} \cdot \frac{V_0^2}{\sqrt{2} V_R R_I}.
\end{aligned} \tag{3.10}
$$

Mobility μ can therefore be calculated from n when the sheet resistance $R_{\mathrm{sheet}} = \frac{1}{ned\mu}$ is also known.

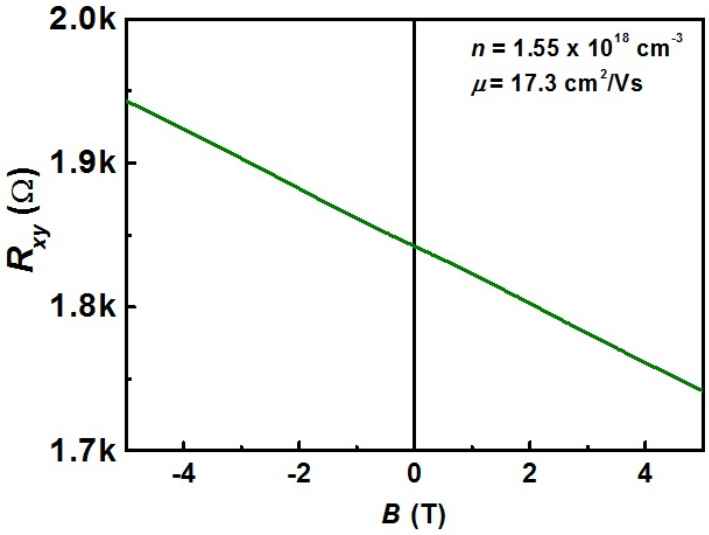

Figure 3.7. Measurement results of R_{xy} using the conventional Hall method on the 200 nm 5 mTorr PLD-grown a-IGZO test sample.

3.3.3. Verification and error analysis of the heterodyne Hall method

To verify the heterodyne Hall method, the circuit was built and tested on the same 200 nm 5 mTorr PLD-grown a-IGZO thin film sample used to verify the heterodyne van der Pauw method. The sample had steady sheet resistance $R_{sheet} = 11.67$ kΩ. Fig. 3.7 shows the results when measured using the conventional 4-point Hall method, with magnetic field B sweeping between -5 T to 5 T. From the R_{xy} slope, it is determined that $n = 1.55 \times 10^{18}$ cm^{-3} and $\mu = 17.3$ cm^2/Vs. In the measured R_{xy} results, background offset is $aR_{xx} = 1.84$ kΩ and the response R_{xy}/B is only 20 Ω/T.

The heterodyne Hall method was tested with magnetic field cycling from 0 to 5 T, then to -5 T, then back to 0. The parameters are chosen as $V_0 = \sqrt{2}$ V, $V_R = 10$ V, and $R_I = 100$ kΩ, $\omega_a = 1.7$ Hz, and $\omega_b = 6.8$ Hz. The directly measured output signal V_{out} is plotted in Fig. 3.8(a). Note the apparent phase drift in panel (a).

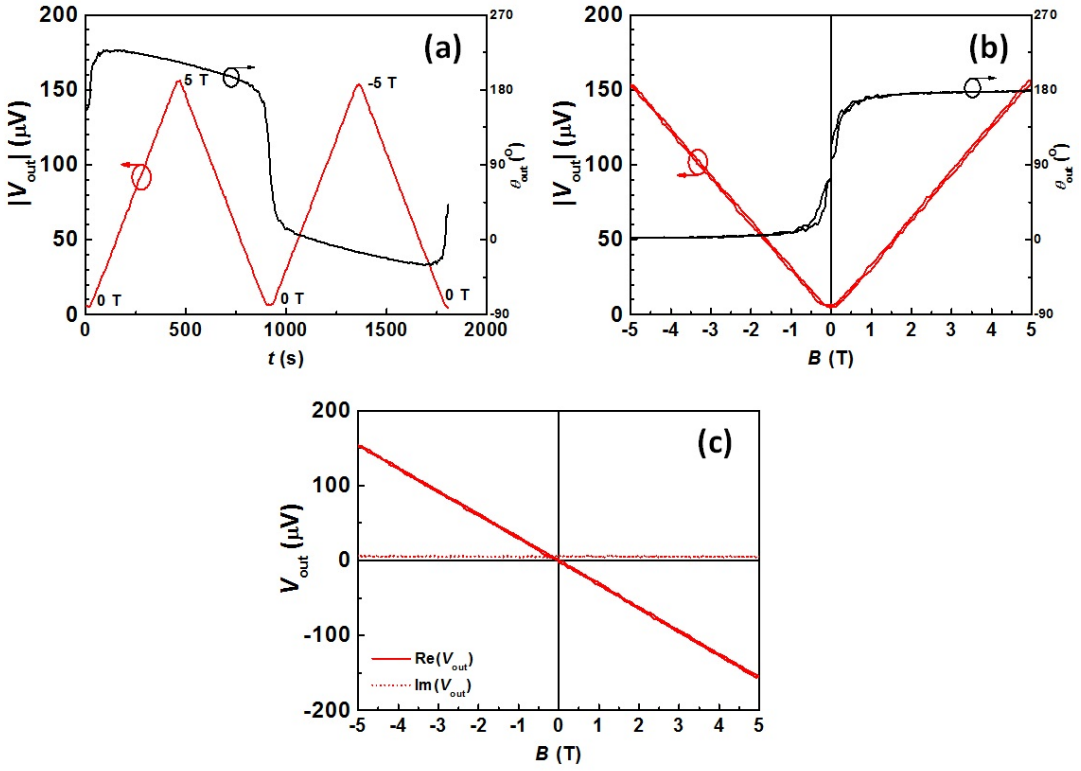

Figure 3.8. Magnetic field sweep results using the heterodyne Hall method on the 200 nm 5 mTorr PLD-grown a-IGZO test sample. (a) Directly measured amplitude and phase of output signal V_{out} as a function of time t. A linear drift of V_{out} phase can be observed. (b) The amplitude and phase of V_{out} after synchronicity correction plotted as a function of magnetic field B. The results for the up-sweep and down-sweep now align well with each other. Note the $|V_{\text{out}}|$ still does not reach 0 at $B = 0$ even after synchronicity correction. (c) The real and imaginary part of V_{out} after synchronicity correction plotted as a function of magnetic field B. Note the real part depends linearly on B, and there is a constant non-zero offset in the imaginary part.

It is clear from the phase drift in this data that the directly measured data needs to be corrected before applying Eq. (3.10). As shown in Fig. 3.8(a), where the magnitude and phase of the output voltage are plotted in time, the V_{out} phase showed the expected 180-degree phase shift when the magnetic field changes polarity, but in addition there

was an overall slope indicating an unexpected phase drift in time. The phase drift can be explained by the synchronicity error from the frequency mismatch between the output signal and the lock-in reference signal arising because ω_a and ω_b are not perfectly synchronized. Estimating from the phase drift rate, the frequency difference between the lock-in reference signal and the output signal is only 0.00016 Hz, smaller than the frequency accuracy of 0.001 Hz for the oscillators in the lock-in amplifiers we used as signal sources. A synchronicity correction was performed after the fact, by assuming a constant phase drift rate. The V_{out} after synchronicity correction is plotted in Fig. 3.8(b). Now the output phase remains the same for up-sweep and down-sweep, and only changes polarity with magnetic field B. After the synchronicity correction, V_{out} still has non-zero amplitude at $B = 0$. This non-zero output is caused by an offset error. By plotting the real and imaginary parts of V_{out} as Fig. 3.8(c), it is clear that the real part is the desired Hall signal that changes linearly with B, and the imaginary part is just a constant offset independent of B.

This imaginary offset error can be explained by the phase misalignment of the two output components $V_a V_{AC}/V_R$ and $-V_b V_{BD}/V_R$. Fig. 3.9 demonstrates how those two components add up to generate the output signal V_{out}. In an ideal circuit, the two vector components have exactly opposite phases, and exactly the same amplitude at $B = 0$, giving $V_{\text{out}} = 0$ at $B = 0$. During the magnet sweep, both components remain opposite to each other, with only the amplitudes changing linearly with B. Thus V_{out} also changes linearly with B in an ideal circuit. In a real circuit, however, the two components are not exactly opposite to each other, giving a small offset V_{offset} at $B = 0$. During the magnet sweep, the amplitudes of the two components change linearly with B, but the

amplitude of their vector sum V_{out} is not linear with B. The output signal V_{out} can be decomposed as the vector sum of the offset signal V_{offset} and the desired Hall signal V_{Hall}. As shown in the right panel of Fig. 3.9, V_{offset} remains constant during magnet sweep, and V_{Hall} is perpendicular with V_{offset}. Therefore, amplitude of the Hall signal $|V_{\text{Hall}}|$ can be calculated from the output amplitude $|V_{\text{out}}|$ and the offset amplitude $|V_{\text{offset}}|$ from the following equation, where $|V_{\text{offset}}|$ can be measured at $B = 0$.

$$|V_{\text{out}}|^2 = |V_{\text{Hall}}|^2 + |V_{\text{offset}}|^2 \tag{3.11}$$

The Hall signal amplitude $|V_{\text{Hall}}|$ is then inserted into Eq. (3.10) to calculate carrier density n and thus mobility μ.

For most experiments like the one in Fig. 3.8, the offset correction can be skipped because $|V_{\text{offset}}|$ is so small that $|V_{\text{Hall}}| \approx |V_{\text{out}}|$ for $|B| > 0.5$ T. Thus only one fixed large B field is needed for Hall measurements, making the heterodyne Hall method ideal for measuring fast transient of n and μ. As shown in Fig. 3.8(b), the $|V_{\text{Hall}}|/B$ slope can be directly identified from a single data point at any sufficiently large B field. Using the output amplitude at $B = 4$ T, the calculated carrier density n is 1.54×10^{18} cm^{-3} and the sample mobility μ is 17.3 cm^2/Vs, both agree to within less than 1% with that obtained from the standard Hall measurement reported at the start of this section.

In the cases where only small magnetic fields are available, a high-accuracy Hall measurement is possible with only two data points, one at zero field to measure $|V_{\text{offset}}|$ and the other at magnetic field B_0 to measure $|V_{\text{out}}|$. When estimating the offset $|V_{\text{offset}}|$, there is inevitably some error that can lead to large error in the desired signal $|V_{\text{Hall}}|$. To increase

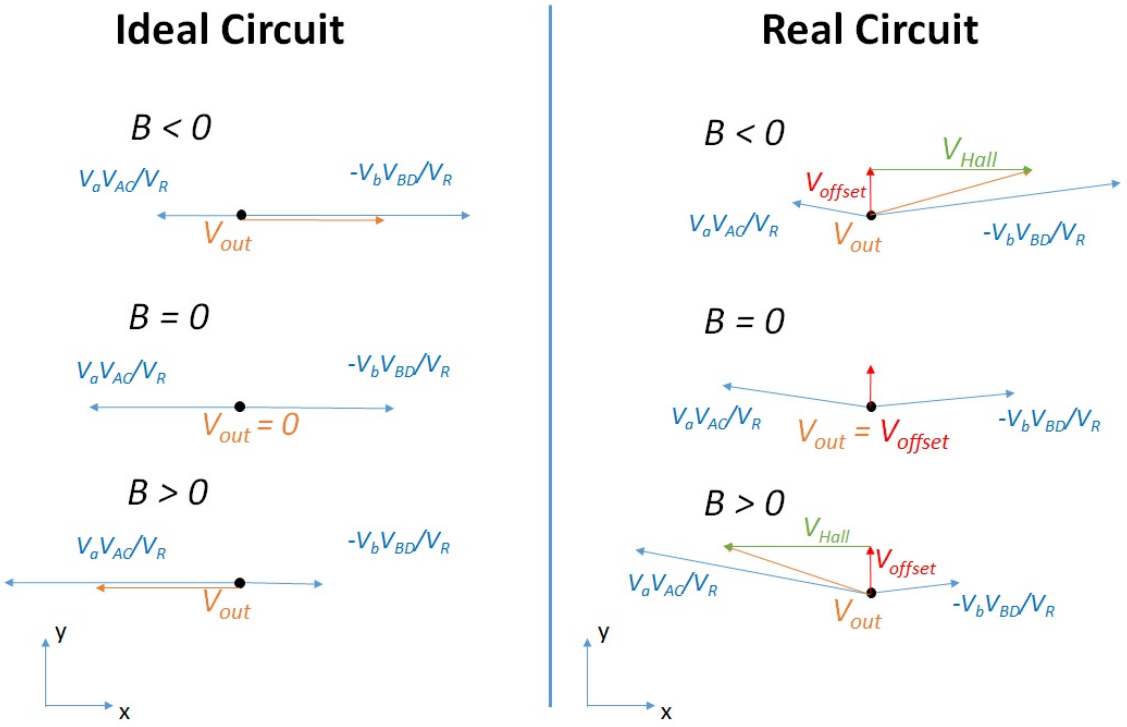

Figure 3.9. Schematic illustration of the components that added up to produce the measured output V_{out}. (left) V_{out} decomposed as the sum of the multiplier outputs in an ideal circuit. V_{out} is 0 at $B = 0$, and changes linearly with B. (right) V_{out} decomposed as the sum of multiplier outputs in a real circuit, where the phase misalignment causes non-zero V_{offset} at $B = 0$. V_{out} measured in a real circuit can be decompose as the vector sum of V_{Hall} and V_{offset}, where V_{Hall} changes linearly with B and V_{offset} remains constant.

the signal-to-noise ratio, an alternative way is to intentionally tune the calibration potentiometer R_P in the circuit so that $|V_{\text{out}}| \gg |V_{\text{offset}}|$ at $B = 0$, and then measure $|V_{\text{out}}|$ at $B = 0$ and $B = B_0$. This gives $\Delta|V_{\text{Hall}}| \approx \Delta|V_{\text{out}}|$, and carrier density n and mobility μ can be estimated from $\Delta|V_{\text{Hall}}|/B_0$ using Eq. (3.10). This two-field method has been tested on the same a-IGZO sample with $B_0 = \pm$ 0.1 T. $|V_{\text{out}}|$ measured at frequency $\omega_a + \omega_b$ is shown in Fig. 3.10. From the slope, the calculated carrier density n is 1.50 $\times$ 10^{18} cm^{-3}

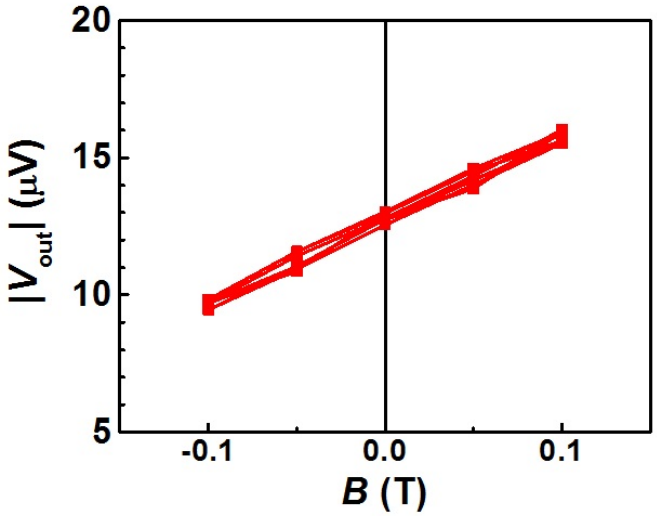

Figure 3.10. Measurement results of $|V_{\text{out}}|$ using the heterodyne Hall method on the 200 nm 5 mTorr PLD-grown a-IGZO test sample with maximum field of only $B_{\text{max}} = \pm 0.1$ T. The calibration potentiometer R_P was intentionally off-calibrated to have $|V_{\text{out}}| \gg |V_{\text{offset}}|$ at $B = 0$. The sweep was repeated several times to check reproductivity of the results.

and the sample mobility μ is 17.8 cm^2/Vs, very close to those measured with an order of magnitude larger magnetic fields.

3.3.4. Advantages of the heterodyne Hall method

Comparing with the conventional Hall method, the heterodyne Hall method reduces the measurement time needed, while increasing the measurement accuracy. With the heterodyne Hall method, the carrier density transient can therefore be directly measured, and Hall effect measurements can be applied to materials with extremely low mobilities.

One major limitation of the conventional Hall method is that it cannot accurately measure the carrier density transient continuously. Previously, Hall measurements could only be conducted at a few discrete time points (see for example Fig. 2.12), because each

Hall measurement requires either sweeping the magnetic field or switching the contacts. Thus one could at best interpolate an average electron density n and mobility μ during that time period. Moreover, the longitudinal resistance component aR_{xx} may also change during the magnet sweeping or contact switching, introducing extra measurement error. Indeed, when measuring mobility change during transient photoresponse using the conventional Hall method, increased variance in the Hall mobility μ was observed right after LED switch, when conductivity σ was changing rapidly (Fig. 2.12).

As we shall demonstrate, the heterodyne Hall method allows continuous measurements of carrier density transient. By applying a constant magnetic field, the carrier density n can be calculated from a continuous transient of the heterodyne Hall output V_{out} through Eq. (3.10). The carrier density transient in a 50 nm capped $P_{O_2} = 15$ mTorr sample was measured and plotted in Fig. 3.11. The heterodyne Hall circuit was calibrated so that carrier density n can be directly calculated from V_{out} with magnetic field $B = 5$ T. From the graph, the initial and final carrier densities are 5.6×10^{17} cm^{-3} and 13.5×10^{17} cm^{-3}, respectively. The initial and final sheet resistances measured using the van der Pauw method are 128.3 kΩ and 49.6 kΩ, respectively. Thus the mobility has increased from 17.4 cm^2/Vs to 18.7 cm^2/Vs during the illumination-induced transient measurement. This data represents, to our knowledge, the first direct measurement of illumination-induced carrier density transient in amorphous oxide systems. Previous reports only measured the conductivity transients, and assumed constant mobility without verification. [**20**, **71**, **72**] As a result of the present work, this assumption can now be verified using the heterodyne Hall method, to identify any mobility transient response.

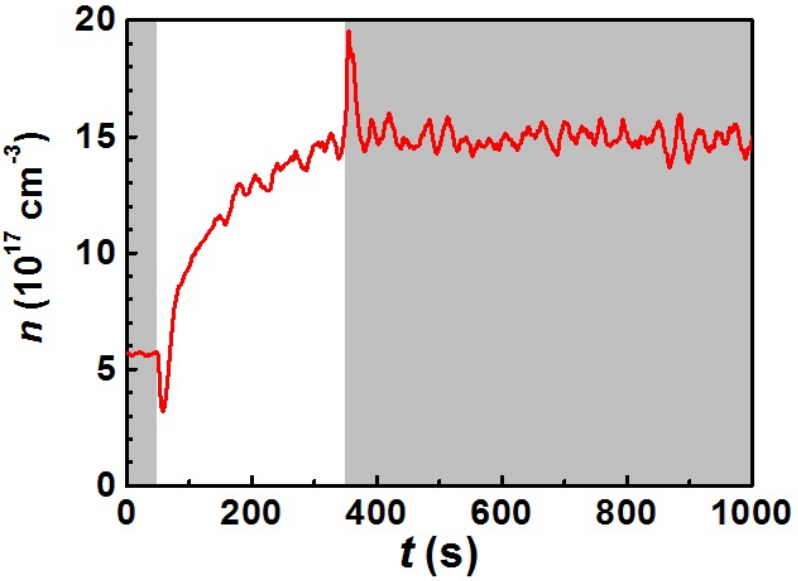

Figure 3.11. Carrier density transient measured using the heterodyne Hall method on the 50 nm 15 mTorr capped PLD-grown a-IGZO thin film sample. The magnetic field was kept at 5 T during the measurement. The sample was illuminated by a 385 nm UV LED operating at 10 mA constant current. The time range with LED on is indicated by the white background. The sample was kept in dark when not illuminated, as indicated by the gray background.

We also show below that the heterodyne Hall method might be able to measure samples with unprecedented low mobilities, or be able to measure useful Hall signals in unprecedented low magnetic fields. The limits of accuracy of a Hall measurement for low mobility samples or at low magnetic fields is usually limited by the minimum μB product that can be accurately measured. This is because in a Hall measurement, the desired signal is the R_{xy} component, the R_{xx} component sets the scale for all background effects which can obscure this signal, such as an overall offset which might drift with time and noise. Thus the effective signal-to-noise ratio (SNR) is proportional to the ratio of R_{xy} divided by R_{xx}

which is simply the product of μ and B.

$$SNR \propto \frac{R_{xy}}{R_{xx}} \propto \frac{B/ned}{1/ne\mu d} = \mu B \tag{3.12}$$

Therefore, accurate Hall measurements in low mobility materials can normally only be handled by applying huge magnetic fields.

Many previous reports have tried to improve the capability of the conventional Hall method by decoupling the desired R_{xy} component from the aR_{xx} background. The most widely used approach is the AC magnetic field method, which modulates the magnetic field B, thus R_{xy}, by a low frequency, and measures only the signal at the modulation frequency. [**73**, **74**] The AC magnetic field is usually generated by a specially designed electromagnet which can tolerate a large oscillating current. Gunawan *et al.* proposed a more compact and cost-effective way to generate the AC magnetic field with a pair of cylindrical diametric magnets rotating mechanically at the modulation frequency. [**75**] Nevertheless, all AC magnetic field systems require very low modulation frequencies, typically 0.1 Hz or lower, and have limited maximum available magnetic field, typically around 1 T. [**76**] Thus they can only be applied to samples with mobility of 0.1 cm^2/Vs or higher, and need very long measurement times on the scale of an hour or more to get a single data value.

In the face of these daunting measurement difficulties, low-mobility materials are showing increasing technological importance. For example, transparent p-type amorphous oxides are necessary for making transparent, flexible, all-oxide complementary field-effect transistors together with n-type amorphous oxides such as a-IGZO. P-type amorphous oxide such as delafossite $CuAlO_2$ was reported to have a Hall mobility $\mu = 0.03$ cm^2/Vs. [**77**]

Another important low mobility material is the ionic conductors, also known as solid electrolytes. Ionic conductors are receiving increasing applications for energy conversion devices including Li-ion batteries and solid oxide fuel cells. [**78**, **79**] Electricity is conducted in ionic conductors by ions instead of electrons or holes, thus carrier mobility can be very low due to the ionic mass which exceeds the electron and hole masses by almost 4 orders of magnitude. Ionic conductor $RbAg_4I_5$ was reported to have a mobility $\mu = 0.05$ cm^2/Vs. [**80**] Such low mobility cannot be easily characterized using the standard Hall effect techniques.

The heterodyne Hall method makes it much easier to measure Hall mobilities in low mobility materials. This is achieved by canceling the background signal component aR_{xx} through the experimental design. Thus the heterodyne Hall method can be much more cost effective compared to previous methods based on modulated AC magnetic field, and is readily compatible with all kinds of DC magnetic field sources. Estimating from Fig. 3.10, using electrical components with higher accuracy, the smallest field to extract a slope with 10% accuracy is $B_{\min} \approx 0.01$ T. Eq. (3.12) shows that the minimum measurable μB sets the capability of Hall measurements, which equals to

$$\mu B_{\min} \approx \left(15 \text{ cm}^2/\text{Vs}\right) \times (0.01 \text{ T}) = \left(0.0015 \text{ m}^2/\text{Vs}\right) \times (0.01 \text{ T}) = 1.5 \times 10^{-5}.$$

Using a simple table-top Hall effect setup made of 2 rare earth magnets above and below the sample, a magnetic field around 0.3 T can be easily achieved. Together with the heterodyne Hall method, the minimum measurable mobility is $\mu_{\min}(0.3\text{T}) = 1.5 \times 10^{-5}$ / 0.3 T = 0.5 cm^2/Vs, which is good enough for most semiconductor materials, including n-type amorphous oxides such as a-IGZO. In comparison, a commercially-designed Ecopia

HMS-3000 Hall measurement system requires sample mobility to be twice as large above 1 cm^2/Vs with a much more cumbersome 0.58 T permanent magnet that must be mechanically flipped from +B to -B polarity for a single measurement. Using the 15 T magnet in our lab, the minimum measurable mobility can be further reduced to only $\mu_{min}(15T) = 1.5 \times 10^{-5}$ / 15 T = 0.01 cm^2/Vs, which is capable for measuring low mobility materials including p-type amorphous oxides and ionic conductors. The minimum measurable mobility can be as low as $\mu_{min}(45T) = 1.5 \times 10^{-5}$ / 45 T $\approx$ 0.003 cm^2/Vs using the 45 T DC magnetic field at the National High Magnetic Field Lab in Tallahassee.

3.4. Modular time division multiplexer for efficient simultaneous characterization of fast and slow transients in multiple samples

3.4.1. System design

In this section, a modular time division multiplexer (MTDM) will be introduced to measure multiple samples with transient responses exhibiting a broad range of time constants. This work was recently accepted for publication. [**81**] Transient photoresponse in a-IGZO thin films exhibits a very fast transient at short time scales right after the LED turns on / off, and the response becomes extremely slow at long time scales. Thus the measurement setup should collect data initially with a temporal resolution as fine as possible, then decrease the time resolution at longer times for the slow response to reduce redundancy. Previous reports only focused on time scales shorter than one day. Such a short measurement duration can lead to an underestimation of the time scales and the total response amplitude. Measurement duration up to months are necessary for a complete characterization of the transient photoresponse in a-IGZO thin films. Also, since a-IGZO

properties depend heavily on the growth conditions, multiple samples need to be characterized to fully understand the material system, thus the measurement setup should utilize a minimal number of measurement instruments efficiently to measure as many samples as possible with as few instruments as possible. MTDM units are designed to meet the above requirements.

Fig. 3.12 shows the system design of the MTDM unit. It has two different modes, labeled as the dedicated mode and the multiplexed mode. The dedicated mode measures the initial fast response and the multiplexed model measures the subsequent slow response. Since the fast response only accounts for a small portion of total response duration, there is no need to measure the fast response of all samples simultaneously. Thus, at most one sample is measured in the so-called dedicated mode at any given time and all other samples are measured simultaneously in the multiplexed mode. The complete circuit diagram of a MTDM unit is included in Appendix A.

3.4.2. Dedicated mode and multiplexed mode

The dedicated mode directly connects one sample with one measurement instrument, thus the data collection from this sample can be the as fast as the measurement instrument can support. As shown in Fig. 3.12, the sample connected to the dedicated mode is selected by a rotary switch to make sure that at most one sample is connected to the dedicated mode. There is also an open position in the switch, which connects the dedicated mode measurement device to an open circuit. This position is selected when all samples are measured in the multiplexed mode.

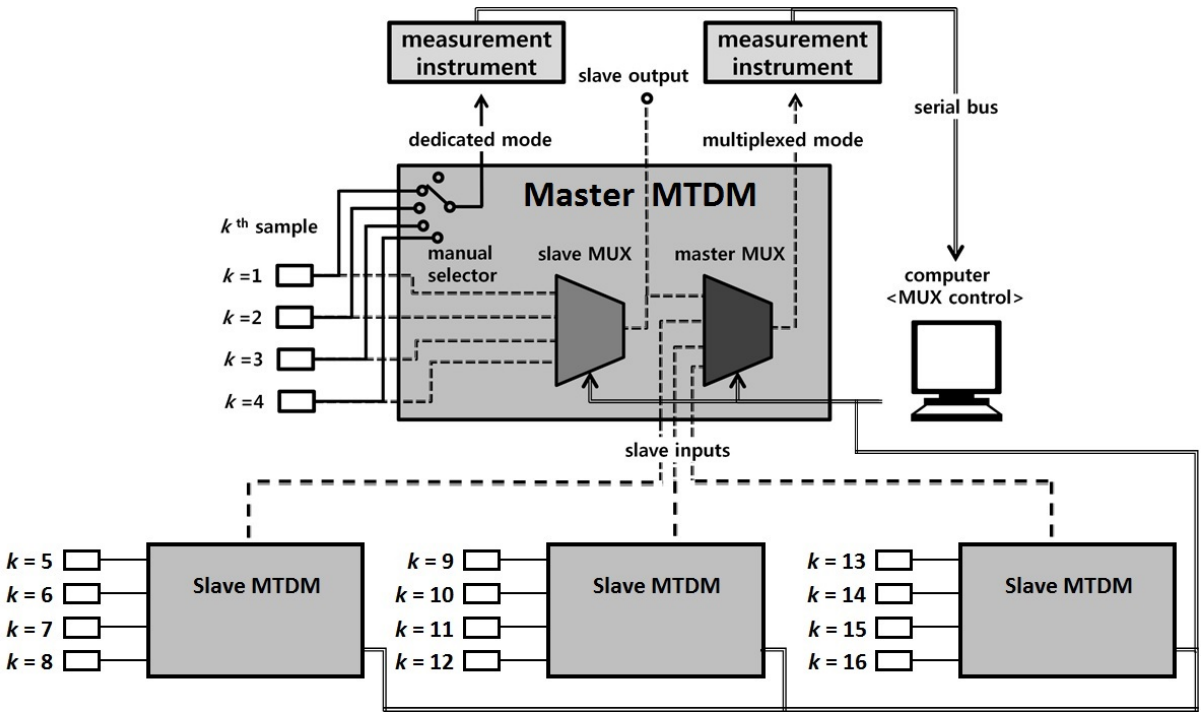

Figure 3.12. System design of the modular time division multiplexer (MTDM) unit. Solid lines symbolize the dedicated mode connections. Dashed lines represent the multiplexed mode connections. The hollow lines are data bus signals to and from the computer. A two-layer hierarchy with 4 channels in each layer is shown. The slave MTDM units have the same internal design as the master MTDM unit. At the top of the figure, the measurement instruments are used for the dedicated mode and the multiplexed mode respectively. The rotary switch is in position 1 indicating that the $k = 1$ sample is in the dedicated mode.

The multiplexed mode applies the time-division multiplexing method to measure multiple samples with a single measurement instrument. All samples are connected to the same measurement instrument through a multiplexer, which receives control signals from a computer and allows only one sample to be connected with the measurement instrument at a time. The computer sends control signals to cycle through all samples in sequence. Therefore, the measurement interval for each sample, Θ_M, long enough to exceed the

stabilization time of the measurement instrument after selecting the next sample, τ_s, multiplied by the total number of samples connected, N.

$$\Theta_M \geq N \cdot \tau_s \tag{3.13}$$

The maximum number of samples in one single MTDM unit is limited by both the space available for the sample housing units as well as by the number of selector channels on the multiplexer chip. This limitation is solved by using a hierarchy of multiplexers. As shown in Fig. 3.12, multiple MTDM units are used, with one labeled as the master unit and others labeled as the slave units. The output from the slave units are sent to the master unit, where all output signals from the first layer of multiplexers are selected by a second layer multiplexer. If only k samples are allowed for a single multiplexer, a two layer hierarchy would accommodate k^2 samples, and the number can be easily increased with more layers of hierarchy. Note the control signals generated from the computer should provide synchronized control for all multiplexers.

3.4.3. Decay time constant estimation: Switching from the dedicated to the multiplexed mode

When measuring a transient response, it is important to identify how rapidly the sample is decaying at any given instant to decide which measurement mode one should be in. Because the signal transient is always slowing down, the only transition that the system needs to monitor is that from dedicated to multiplexed mode. In the MTDM measurements, the decay time constant τ_n at time t_n is estimated by fitting the last $q = 50$ collected data with a simple exponential response $\xi_n(t) = A_n e^{-t/\tau_n} + B_n$, where A_n and

B_n are just two fit parameters. The best fit for τ_n is determine using the least square error method. Once τ_n is known, the desire measurement interval T_n is decided proportional to τ_n, i.e. $T_n = R \cdot \tau_n$, where R is a user-specified constant defining measurement resolution.

The desired measurement interval T_n also decides when one sample should be switched from the dedicated mode to the multiplexed mode. At the beginning of each measurement, the sample is put in the dedicated mode and the data is collected at the maximum rate. When there is enough data to estimate T_n, the data collection interval is dynamically adjusted to T_n to reduce redundant data. When T_n further increases to be larger than the measurement interval in the multiplexed mode Θ_M, defined in Eq. (3.13), this sample can be switched to the multiplexed mode. In real experiments, considering the errors in τ_n estimation, samples are switched from the dedicated mode to the multiplexed mode only when T_n is significantly larger then Θ_M.

3.5. Second round: Transient photoconductivity for a-IGZO thin films

Once the improved MTDM measurement system became operational, second round of measurements of the transient photoresponse in a-IGZO thin films with time scales up to several months was conducted using the MTDM of Section 3.4. The MTDM unit we built supports 4 samples measured simultaneously using one multiplexer, and the second layer multiplexer was included for future expansion. Two SR830 lock-in amplifiers were used as the measurement instruments. A Python program was developed to generate control signals, estimate the decay time constant in real time, adjust measurement interval in the dedicated mode, and collect data from the lock-in amplifiers.

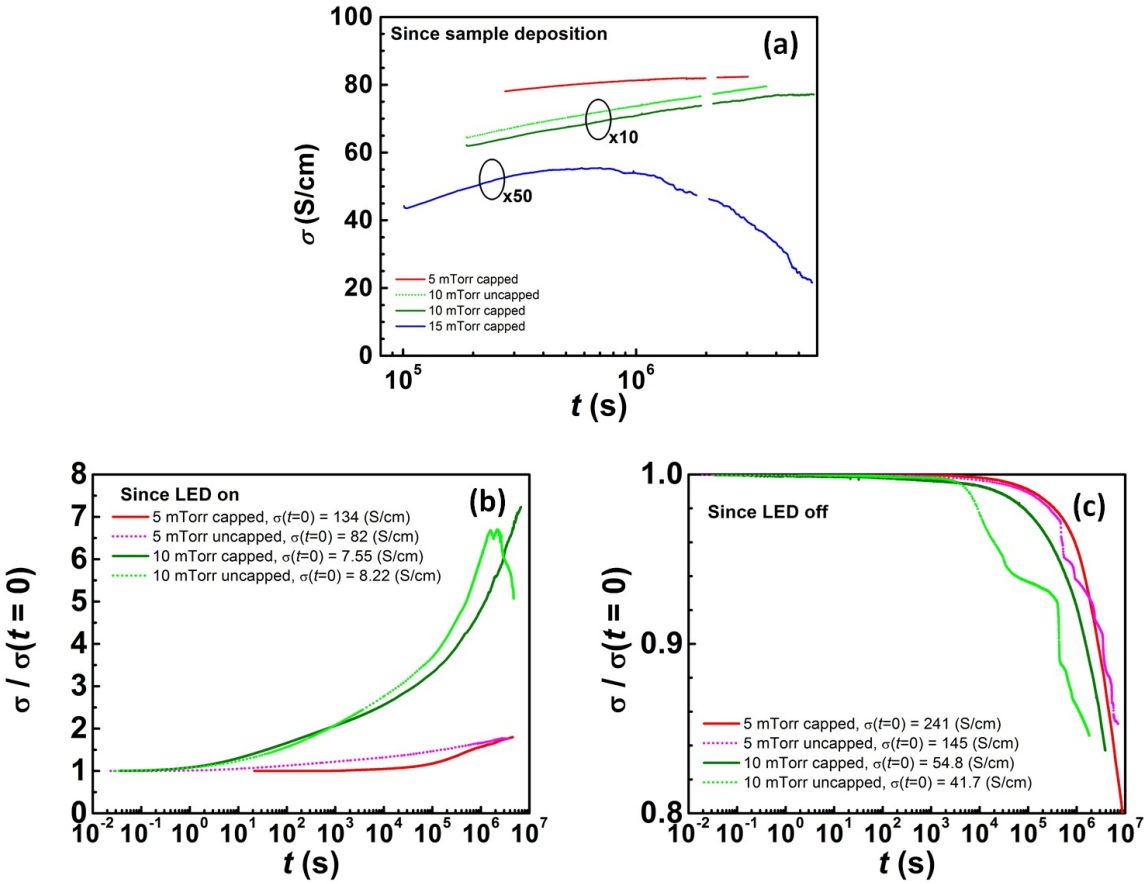

Figure 3.13. Second round of conductivity transients measurement results for the a-IGZO thin film samples. (a) Transient conductivity change of pristine a-IGZO thin film samples after PLD deposition. (b) Transient photoconductivity of a-IGZO thin films under UV LED illumination. (c) Transient photoconductivity of a-IGZO thin films during dark relaxation after prolonged UV LED illumination.

In the second round of transient photoresponse measurements, a batch of 50 nm a-IGZO thin film samples were deposited by PLD at P_{O_2} = 5, 10, 15 mTorr. Both capped and uncapped samples, were used in the measurement. Fig. 3.13 compares the transient responses at different phases of the photoresponse measurements. With the help of the MTDM unit, transient responses were measured with initial measurement intervals as

rapid as 30 ms and the total measurement durations as long as 10^7 s (4 months). Without the MTDM unit, measurements for the presented data would have taken over 2 years to take sequentially.

We now review the results of these measurements starting with the dark relaxation response of pristine samples shown in Fig. 3.13(a). As expected, the initial conductivity σ of the samples right after deposition is larger for lower oxygen pressure P_{O_2} during deposition and monitored for several weeks. The pristine samples are kept in the dark after deposition. For all pristine samples, conductivity increased slowly after deposition. This is probably due to structural relaxation, as PLD growth of IGZO thin films at room temperature is a non-equilibrium process. In the 15 mTorr sample, the conductivity started to decrease after a week, around 10^6 seconds, whereas all other more heavily doped samples grown at lower P_{O_2} show a weakly increasing conductivity appearing to level-off at long times. This decrease in conductivity in the 15 mTorr sample may be the result of a post-illumination relaxation since the samples are exposed to UV light during PLD growth and such dark relaxations are known to exhibit reduced conductivities.

Photoresponses during UV illumination and dark relaxation in Fig. 3.13 panels (b) and (c), respectively, clearly indicate the importance of encapsulation. For both illumination and relaxation, the capped samples (dark green, dark red) showed simple monotonic response with decreasing rate, whereas, the 10 mTorr uncapped sample in particular (light green) showed a small conductivity decrease after two weeks of UV illumination in panel (b), and both uncapped samples showed apparently random steps of rapid conductivity decrease during dark relaxation in panel (c). Data analysis in the following chapters

will discuss these results with special emphasis on the very smooth month-long transient observed in the post-illumination dark relaxation of the encapsulated samples.

CHAPTER 4

Mathematical Analysis of General Transient Response

This chapter talks about how any general transient response towards an asymptotic steady state can be modeled as the superposition of exponential transients with distributed time constants. Section 4.1 shows its mathematical representation and the condition to apply this analysis. Section 4.2 discusses common fitting methods to the directly measured transient response data that can extract a time constant distribution. A classification of fitting methods as descriptive and predictive is proposed, and the dependence of the fitted spectrum on measurement duration is studied. In Section 4.3, using the properties of the convolution integral for the transient on a semi-log plot versus log-time, it is revealed that the log-scale derivative plot can be used to directly identify features of the the log-scale decay spectrum. From this analysis, we derive the minimum required measurement duration to characterize the time constant distribution as the inflection point on the semi-log plot. With the convolution integral, Section 4.4 develops a simple method that directly estimates the decay spectrum and the asymptotic value of the decay using easily identifiable features on the semi-log transient plot. The application of the distributed time constant analysis methods is demonstrated in Section 4.5 with experimental data from a-IGZO photoconductivity transients.

4.1. Generalized transient response with distributed time constants

Simple exponential decay, which successfully describes transient response in many crystalline systems, fails to fit transient photoresponse in a-IGZO thin films. Fig. 4.1 shows the best simple exponential fit for the initial 1/3 and the final 1/3 of the long-term photoconductivity transients observed in the encapsulated a-IGZO samples. For all responses, the initial segments show decay rates significantly faster than the corresponding final segments in the same response. Thus the measured transients clearly have more than one time constant involved. To have a complete description of such non-exponential transients, this section will generalize them as a summation of exponential decays over a distribution of time constants.

Time constants characterize the dynamic response of non-equilibrium carrier concentrations in solid state systems. In crystalline materials, decays are typically characterized by a single exponential decay time constant or a few discrete time constants, whereas amorphous systems are better described by a statistical distribution of time constants. [**82**] As an example for crystalline systems, Shockley-Read-Hall theory assumes a single activation energy for the emission rate from each defect species to the nearest energy band. [**83**] For crystals with multiple species of ionic dopants, the photoresponse can have a different time constant associated with each defect level. This has been experimentally verified by photoinduced current transient spectroscopy (PICTS) experiments. [**84**, **85**] In amorphous semiconductors, on the other hand, the observed transient responses are typically more complicated. [**20**, **28**, **86**] Although some groups have modeled transients in amorphous systems in terms of a handful of discrete relaxation time constants, [**20**,**87**] the justification for such an interpretation is unclear due to structural randomness which

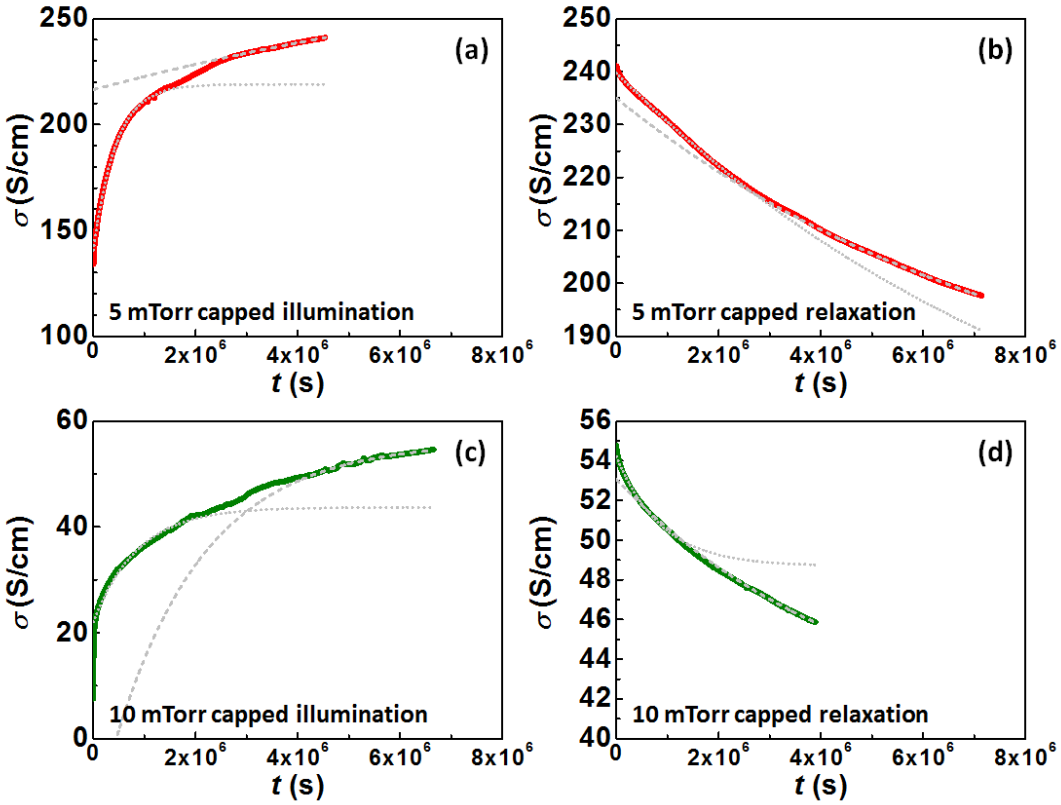

Figure 4.1. Transient photoconductivity of a-IGZO compared to simple exponential fits in (a) photo-illumination and (b) dark relaxation of the 5 mTorr capped sample, and (c) photo-illumination and (d) dark relaxation of the 10 mTorr capped sample. The measured transient photoconductivity is plotted as the thick red curves for the 5 mTorr sample, and the thick green curves for the 10 mTorr sample. The best simple exponential fit to the initial 1/3 of each curve is plotted as a dotted gray line, and the best simple exponential fit to the final 1/3 of each curve is plotted as a dashed gray line. Note the best simple exponential fits at short time scales do not match those at long time scales.

seems to preclude sub-populations of nominally identical defects. Instead, interpretations of relaxation behavior in amorphous systems more typically assume a continuum of time constants which are statistically distributed. [**55**, **86**, **88**] Alternatively, such non-exponential transient responses can be modeled with a time-dependent time constant,

such as predicted in the dispersive diffusion model, whereby a power-law behavior of the time constant results in a stretched exponential transient response. [**28**, **89**] Regardless of the underlying physical mechanism of the non-exponential decay, any such transient can always be mathematically decomposed into an amplitude spectrum of exponential decays with different time constants, whereby the shape of the spectrum serves as a fingerprint of the physical mechanism behind the non-exponential decay. [**90**]

The analysis method developed here assumes that the transient response of interest $f(t)$ has a positive definite decay spectrum when expressed as a sum of exponential decays. This is satisfied if and only if the decay amplitude is decreasing monotonically with time, and all higher derivatives also increase or decrease monotonically with alternating sign of derivative order. [**91**]

$$(-1)^n \frac{d^n f(t)}{dt^n} > 0, n = 1, 2, 3 \cdots \tag{4.1}$$

In practice, due to the large noise in higher order derivatives, it is usually only possible to accurately verify the first and the second order derivatives of the transient to apply the methods developed here. The above property is observed in almost all experimentally measured decay responses as long as the system is damped or overdamped (not underdamped) and there is no oscillatory term in the response. [**91**] Many other transient responses, including the generation and annealing of excess carriers and structural defects due to thermal stress, electric field, and illumination are proposed to have similar relaxation kinetics. [**28**] Thus the analysis methods developed here also apply to more general non-exponential relaxation problems.

The continuous time constant distribution case can be generalized from the simpler case of discrete time constants. The simplest transient response is a simple exponential response with a single time constant τ_0, amplitude A_0 at $t = 0$, and an asymptotic background f_∞ for $t \to +\infty$.

$$f(t) = f_\infty + A_0 \mathrm{e}^{-t/\tau_0} \tag{4.2}$$

For multi-exponential response with a finite number of discrete time constants $\tau_1, \tau_2 \cdots \tau_n$, the overall response $f(t)$ is just the sum of simple exponentials, with amplitude $A_1, A_2 \cdots A_n$ for each time constant.

$$f(t) = f_\infty + \sum_{i=1}^{n} A_i \mathrm{e}^{-t/\tau_i} \tag{4.3}$$

The number of fit parameters can become statistically large as the time-constant resolution increases, and the response function soon crosses over to the continuum limit. Such a generic transient response signal $f(t)$ over time t can be expressed in a Fredholm integral equation of the first kind, as Eq. (4.4), with the simple exponential decay function $h(t, \tau) = e^{-t/\tau}$ as the kernel function of the continuous decay spectrum variable τ, and a signed distribution density function $g(\tau)$ defined for each time constant τ taking the role of the discrete amplitude parameters A_n, over an asymptotic constant background f_∞.

$$\begin{aligned} f(t) &= f_\infty + \int_0^{+\infty} g(\tau) \mathrm{e}^{-t/\tau} d\tau \\ &= f_\infty + \int_0^{+\infty} g(\tau) h(t, \tau) d\tau \end{aligned} \tag{4.4}$$

Johnston used a similar expression to decompose the stretched exponential function as a Fredholm integral of a decay rate distribution. [**90**] As Zorn has shown, [**91**] Eq. (4.4) can describe any transient response that satisfies the general monotonic behavior of Eq. (4.1).

Non-exponential transients usually consist of time constant distributions that span several orders of magnitude. Thus it is often more convenient to re-write Eq. (4.4) as a function of $\ln\tau$. To distinguish from the linear-scale transient $f(t)$, we will label the log-scale transient functions with upper-case letters as $F(x)$. Similarly, log-scale simple exponential decay is labeled as $H(x)$, and log-scale decay spectrum is labeled as $G(u)$. For the log-scale time, one can select an arbitrary unit time τ^* such as $\tau^* = 1s$, and define variables as a function of log-scale time $x = \ln(t/\tau^*)$ and the log-scale time constant $u = \ln(\tau/\tau^*)$, or the equivalent inverse expressions, $t = \tau^* \mathrm{e}^x$ and $\tau = \tau^* \mathrm{e}^u$. Substituting $t = \tau^* \mathrm{e}^x$ and $\tau = \tau^* \mathrm{e}^u$ into Eq. (4.4) gives Eq. (4.5) for the log-scale response $F(x)$, with $G(u) = \tau g(\tau)$ being the log-scale decay spectrum, and $H(x) = \exp[-\exp(x)]$ being the simple exponential decay with time constant $\tau = \tau^*$ represented as a function of log-scale time x.

$$\begin{aligned} F(x) &= f_\infty + \int_{-\infty}^{+\infty} G(u)\mathrm{e}^{-\mathrm{e}^{x-u}} du \\ &= f_\infty + \int_{-\infty}^{+\infty} G(u)H(x-u)du \end{aligned} \tag{4.5}$$

Note in particular the argument of the exponentiated exponential in the top line of Eq. (4.5), whereby x and u appear only in terms of their difference. This fact allows us to write the second line of Eq. (4.5) which explicitly identifies the convolution form. Thus by plotting the response with respect to log-scale time x, the difficult-to-invert Fredholm

integral problem of Eq. (4.4) has been converted into a far more tractable convolution integral form in Eq. (4.5), with impulse response $H(x)$. Note that the impulse function $H(x)$ in the convolution integral Eq. (4.5) is simply the kernel function $h(t, \tau^*) = e^{-t/\tau^*}$ in the Fredholm integral Eq. (4.4) expressed in log-time x. Whereas the transient response $f(t)$ and its derivative $f'(t)$ in linear time are changing monotonically versus time t as in Eq. (4.1), Section 4.3 will show that $F(x)$ always has an inflection point on a semi-log plot versus x, meaning that the first derivative in log-time $\frac{dF(x)}{dx}$ has an extremum versus x. Therefore it can be highly illuminating to plot the transient response on a semi-log plot versus log-time.

The generalized transient response function Eq. (4.4) in linear time and (4.5) in log-time clearly can be applied for discrete time constants, as well. Starting with the simple exponential response in Eq. (4.2), this corresponds to a decay spectrum $g(\tau) = A_0\delta(\tau - \tau_0)$ in Eq. (4.4), and a log-scale decay spectrum $G(u) = A_0\delta(u - u_0)$ in Eq. (4.5), where $u_0 = \ln(\tau_0/\tau^*)$. Thus the log-scale transient response would be Eq. (4.6).

$$F(x) = f_\infty + A_0 H(x - u_0) \tag{4.6}$$

The multi-exponential response in Eq. (4.3) corresponds to the decay spectrum $g(\tau) = \sum A_i\delta(\tau - \tau_i)$, and therefore the log-scale spectrum becomes $G(u) = \sum A_i\delta(u - u_i)$ with $u_i = \ln(\tau_i/\tau^*)$. This $G(u)$ spectrum, when entered into the defining integrals of Eqs. (4.5), would give the following log-scale response $F(x)$.

$$F(x) = f_\infty + \sum_{i=1}^{n} A_i H(x - u_i) \tag{4.7}$$

4.2. Fitting methods for transients with distributed time constants

In most experiments, only the transient response $f(t)$ can be measured directly. The continuous decay spectrum of interest $g(\tau)$ and $G(u)$ are determined by inverting Eq. (4.4) or (4.5) respectively in linear- or log-time, thereby finding the spectrum that best fits the experimental data $f(t)$ or equivalently $F(x)$. Several fitting methods have been developed in literature. The three of them that have been widely used to characterize transient responses will be discussed below as examples. The continuum multi-exponential (CME) fit developed here approximates the continuous integral Eqs. (4.4) and (4.5) as multi-exponential decays with a large number of discrete time constants, without making any prior assumption about the decay spectrum shape or the transient behavior. Alternatively, one can assume a decay spectrum shape *a priori*, such as the Gaussian distribution fit, or a specific transient behavior, such as the stretched exponential fit, and achieve a best fit under that constraint, with significantly fewer fit parameters.

4.2.1. Continuum multi-exponential fit

To extend the multi-exponential fit used for transient photoresponse in amorphous materials previously, [**20**, **87**] here we develop a continuum multi-exponential fit method which works any continuous time constant distribution given sufficient data to describe the whole transient response $f(t)$. [**92**]

To numerically solve the inverse integral of Eqs. (4.4) or equivalently (4.5), one can approximate the continuous decay spectrum as a sum of finely-spaced discrete decay time constants. It is instructive to sample the log-scale decay spectrum $G(u)$ in a finite range from $u_{\min}$ to $u_{\max}$ at a fixed interval Δu, corresponding to sampling the linear-scale decay

spectrum $g(\tau)$ at exponentially increasing time constant points $\tau_{i+1} = e^{\Delta u}\tau_i$. The log-scale decay spectrum $G(u)$ is sampled at log-scale time constants u_1, u_2, $\cdots$ u_i, $\cdots$, equivalent to sampling the linear-scale decay spectrum $g(\tau)$ at time constants $\tau_1 = \tau^* e^{u_1}$, $\tau_2 = \tau^* e^{u_2}$, $\cdots$ $\tau_i = \tau^* e^{u_i}$, $\cdots$. The distribution density $G(u)$ in the range $[u_i, u_{i+1})$ is assumed to be a constant G_i, which is equivalent to assuming a constant distribution density $g_i = G_i/\tau_i$ in the range $[\tau_i, \tau_{i+1})$. Therefore, the Fredholm integral Eq. (4.4) is approximated by the multi-exponential form Eq. (4.8a), where $\Delta\tau_i$ is the sampling interval between two adjacent τ values as $\Delta\tau_i = \tau_{i+1} - \tau_i$. And the convolution integral Eq. (4.5) is approximated by the multi-exponential form Eq. (4.8b), where Δu is a constant.

$$f(t) = f_\infty + \sum_i g_i e^{-t/\tau_i} \Delta\tau_i \tag{4.8a}$$

$$F(x) = f_\infty + \sum_i G_i H(x - u_i) \Delta u \tag{4.8b}$$

With interval $\Delta u \to 0$, the linear-scale Eq. (4.8a) becomes equivalent to the log-scale Eq. (4.8b). The two discrete multi-exponential sum equations provide good approximations to the continuous integral Eqs. (4.4) and (4.5) respectively. [**92**]

In a real experiment, what one measures is the response $f_m = f(t_m)$ at m discrete sampling times t_1, t_2, $\cdots$ t_m, and the decay spectrum $g_i = g(\tau_i) = G_i/\tau_i$ is also sampled at n predetermined discrete time constants τ_1, τ_2, $\cdots$ τ_n. Eq. (4.8) is then reduced to a matrix multiplication.

$$f = M\theta \tag{4.9}$$

$$\text{where } f = \begin{bmatrix} f(t_1) \\ f(t_2) \\ \vdots \\ f(t_m) \end{bmatrix}, \; M = \exp\left(- \begin{bmatrix} 0 & t_1/\tau_1 & t_1/\tau_2 & \cdots & t_1/\tau_n \\ 0 & t_2/\tau_1 & t_2/\tau_2 & \cdots & t_2/\tau_n \\ \vdots & \vdots & \vdots & \ddots & \vdots \\ 0 & t_m/\tau_1 & t_m/\tau_2 & \cdots & t_m/\tau_n \end{bmatrix} \right), \text{ and } \theta = \begin{bmatrix} f_\infty \\ G_1 \Delta u \\ G_2 \Delta u \\ \vdots \\ G_n \Delta u \end{bmatrix}.$$

In this matrix representation, t_1, t_2, $\cdots$ t_m are the time points when measurement is taken, and τ_1, τ_2, $\cdots$ τ_n are the spectrum of time constants decided *a priori*, so each element in matrix M is known in advance. Vector f is the measured transient response. All one need to do is to invert this linear equation to get the vector θ and thus the decay spectrum. However, direct matrix calculation may not yield the best fit result. In practice, one would choose $n < m$, so Eq. (4.9) is over-determined, but a small noise in the measurement data can still lead to a large variation in the decay spectrum solution. To avoid overfitting measurement noise, the solution to Eq. (4.9) has to be constrained to minimize the total cost function C defined in Eq. (4.10).

$$C = \frac{\|M\theta - f\|^2}{2m} + \lambda \frac{\sum_{i=1}^{n} g_i^2}{2m} \tag{4.10}$$

In this cost function, the first term is just the average square error of the fitted response $M\theta$ relative to the experimental response f. The second term is the Tikhonov regularization term to suppress false signals coming from noise and overfitting, where λ is the regularization parameter to determine how much one wants to smooth the decay spectrum against measurement noise. [**88**] Note the asymptotic value, f_∞, should not be included in the regularization term.

A significant advantage of the continuum multi-exponential fit method is that it requires no prior assumptions for the shape of the decay spectrum. As long as data is taken at time scales long enough to identify the asymptotic background, the continuum multi-exponential method can be successfully applied to extract decay spectra of any shape.

4.2.2. Gaussian distribution fit

In many applications, however, the decay spectrum $G(u)$ can be assumed to have a known distribution, such as the Gaussian distribution fit to be discussed here significantly simplifying the fit procedure.

In a disordered system, the statistical nature of the local coordination configuration leads one to expect that any activation energy would become broadened to generate a Gaussian distribution in energy E. [**88**, **93**] Assuming a thermally activated decay response, each relaxation time constant τ can be related to an activation energy E through Eq. (4.11), where ν is the attempt-to-escape frequency, often assumed to be the phonon frequency, k_B is Boltzmann's constant, and T is the temperature. [**88**, **94**]

$$\tau = \tau^* \mathrm{e}^u = \frac{1}{\nu} \mathrm{e}^{E/k_B T} \tag{4.11}$$

Thus a Gaussian distribution with respect to energy E corresponds to a Gaussian distributed decay spectrum $G(u)$ in log-time. The Gaussian distributed $G(u)$ has the form as Eq. (4.12), with integrated spectral weight A, centered at u_0, and standard deviation

s.

$$G(u) = \frac{A}{s\sqrt{2\pi}} \mathrm{e}^{-\frac{(u-u_0)^2}{2s^2}} \tag{4.12}$$

This spectral distribution cannot be directly inserted into equation (4.5) to get the transient response because it does not give a closed form expression for either $f(t)$ or $F(t)$. In real applications, it is only necessary to numerically calculate the response between limited time-scales from $t_{\min}$ to $t_{\max}$, and therefore only a limited decay constant range between $u_{\min}$ and $u_{\max}$ needs to be considered, where $u_{\min}$ and $u_{\max}$ are chosen so that $\exp(u_{\min}) = \tau_{\min} \ll t_{\min}$, and $\exp(u_{\max}) = \tau_{\max} \gg t_{\max}$. With this choice of time constant range, states with time constants below $u_{\min}$ have fully relaxed for all data points at $t > 0$, and states with time constants above $u_{\max}$ would have not started to relax when the measurement ends. Thus decay spectrum distribution out of the $[u_{\min}, u_{\max}]$ range would not affect the transient response in the measurement time range from $t_{\min}$ to $t_{\max}$]. A Gaussian spectrum exponential response on the log-scale would therefore have the following numerical form, where the asymptotic value f_∞ is determined as $f_\infty = f_0 - A$, and f_0 is the initial value measured at $t = 0$.

$$\begin{aligned} F(x) = f_\infty + \frac{A}{s\sqrt{2\pi}} \sum\nolimits_{u_{\min}}^{u_{\max}} \mathrm{e}^{-\frac{(u_i-u_0)^2}{2s^2}} H(x-u_i)\Delta u \\ + A\left[\frac{1}{2} - \frac{1}{2}\mathrm{erf}\left(\frac{u_{\max}-u_0}{\sqrt{2}s}\right)\right] \end{aligned} \tag{4.13}$$

The linear-scale transient response $f(t)$ with time $t > 0$ can then be calculated from equation (4.13). By varying the values of fit parameters A, u_0, and s, the best Gaussian

distribution fit is determined as the parameter set that gives the least square fit to the experimentally measured transient.

4.2.3. Stretched exponential fit

The transient response $f(t)$ could alternately be assumed to follow a stretched exponential in time, as discussed here. Historically, stretched exponential transients were observed in many disordered systems over a large range of time scales. [**71**,**86**,**89**,**95**–**97**] The stretched exponential function corresponds to transient responses with the following linear-scale and log-scale form, where τ_0 is the characteristic time constant, $u_0 = \ln(\tau_0/\tau^*)$ is the characteristic time constant on log-scale, A is total response amplitude, and β is the stretching exponent.

$$
\begin{aligned}
f(t) &= f_\infty + A\mathrm{e}^{-(t/\tau_0)^\beta} \\
F(x) &= f_\infty + A\mathrm{e}^{-\left(\mathrm{e}^{x-u_0}\right)^\beta} \\
&= f_\infty + A \cdot H[\beta(x-u_0)]
\end{aligned}
\tag{4.14}
$$

Compared with the simple exponential response in Eq. (4.6), the stretched exponential function only added a stretched factor β to the log-scale time x inside the argument of H. Thus on a semi-log plot, the stretched exponential response is just the simple exponential response literally stretched horizontally by a factor of $1/\beta$ around u_0.

The stretched exponential decay satisfies Eq. (4.1), thus can be decomposed to distributed time constants with a decay spectrum $G(u)$. For stretched exponentials with rational β values, $G(u)$ can be expressed in a closed analytical form. For example, the stretched exponential decay with $\beta = 1/2$ has the analytical expression for $G(u)$ as Eq.

(4.15). [**90**]

$$G(u) = A\frac{e^{u-u_0/2}}{2\sqrt{\pi}}[H(u-u_0)]^{1/4} \tag{4.15}$$

Johnston calculated the analytical function of $G(u)$ for a few different rational β values, and showed that the stretched exponential transient always yields a continuous asymmetric single-peak decay spectrum $G(u)$ for $0 < \beta < 1$. [**90**] The relationship between the decay spectrum $G(u)$ features and the fit parameters A, τ_0, and β in Eq. (4.14) will be discussed in detail in Chapter 5.

By varying the values of parameters τ_0, A, and β, the least-square fit assuming stretched exponential transient can be determined. The corresponding decay spectrum $G(u)$ is then calculated through numerical inverse Laplace transform of Eq. (4.14). [**98**]

4.2.4. Fitting accuracy for descriptive methods and predictive methods

To distinguish the utility of the various fit methods mentioned above, we propose to classify a fitting method as being either descriptive, if it makes no *a priori* assumptions about the spectrum distribution, or predictive, if it assumes a functional lineshape for the spectrum that is to be parameterized by a small number of variables. [**99**]

Descriptive methods attempt to solve the inverse integral Eqs. (4.4) and (4.5) directly from only the experimental data with no assumption about the time constant distribution. One example of the descriptive methods is the continuum multi-exponential method. Because no knowledge about the decay spectrum is assumed *a priori* in descriptive methods, a large number of fit parameters are required to adapt to all possible spectrum lineshapes. In addition, the finite time scales for experimental measurements limit the

range of time constants that can be studied by descriptive methods. Previous reports on transient responses observed in amorphous oxides usually have time scales from 1 s to 1 day, [**20**, **71**, **86**, **97**] which is often insufficient to realistically describe decay spectra with significant spectral weight at time constants much longer than 1 day. As we will show in Section 4.3, careful consideration however, does allow one to properly identify when the measurement duration is sufficient to accurately characterize the bulk of the spectral distribution.

In some other cases, the response is known to have a certain lineshape for either the decay spectrum $G(u)$ or for the transient $f(t)$. We will label such fitting methods as predictive methods because the behavior at long time scales can be extrapolated from a limited sampling time range of experimental data at short times. The Gaussian distribution fit and the stretched exponential fit discussed above as examples of predictive methods. Both fitting methods have only 3 fit parameters. In general, predictive methods require far fewer fit parameters compared to descriptive methods because the general structure of the decay spectrum $G(u)$ is predetermined.

To identify the best predictive method for the a-IGZO system and the minimum measurement time needed to get reliable fitting results, transient responses are simulated with ideal spectral lineshapes, and fitted with all three fitting methods introduced above. The two generated datasets assume initial response $f_0 = 1$ and the asymptotic response $f_\infty = 0$. The first dataset follows the Gaussian spectrum distribution Eq. (4.12), assuming total spectrum amplitude $A = 1$, average time constant τ_0, and standard deviation $s = \ln 10$. The model spectrum is plotted as the light blue area in Fig. 4.2(a), and the corresponding transient response $F(x)$ is calculated through Eq. (4.13). The second

dataset follows the stretched exponential transient Eq. (4.14), assuming total response amplitude $A = 1$, effective time constant τ_0, and stretched exponent $\beta = 0.5$. The model spectrum for the second dataset is calculated with Eq. (4.15), and is plotted as the light green area in Fig. 4.2(b). Transient data is generated from $t = 10^{-5}\tau_0$ to $t = 10^{3}\tau_0$, with 2000 data points evenly spaced on the semi-log versus log-scale time x. The fitting accuracy of each fitting method is characterized by the root-mean-square (RMS) fitting error ε. For each artificial transient responses, the model spectrum for each dataset is known *a priori*, and the spectra of the best fits from the fitting methods can be compared against this model spectrum. The fitting results are plotted in Fig. 4.2(a) and (b), and the decay spectra corresponding to the fitting results are plotted in Fig. 4.2(c) and (d).

Fig. 4.2 shows that the predictive method is only effective when the correct lineshape is known in advance. When assuming a Gaussian distributed spectrum in the first dataset as in Fig. 4.2(a), the Gaussian distribution method (blue dashed line) correctly fits the transient with negligible fitting error $\varepsilon < 0.001\%$, while the stretched exponential method (green dotted line) fails to fit the transient and exhibits noticeable fitting error $\varepsilon > 1\%$. Similarly, when assuming a stretched exponential transient in the second dataset as in Fig. 4.2(b), the stretched exponential method (green dotted line) correctly fits the transient with $\varepsilon < 0.001\%$, while the Gaussian distribution method (blue dashed line) fails with much larger error $\varepsilon > 1\%$. The difference of the assumptions behind different predictive methods are more obvious when comparing their decay spectra as in Fig. 4.2(c) and (d). The stretched exponential method always assumes an asymmetric decay spectrum, thus fails to fit transient response with symmetric Gaussian distributed spectrum. And the Gaussian distribution method always assumes a symmetric decay spectrum, thus fails to

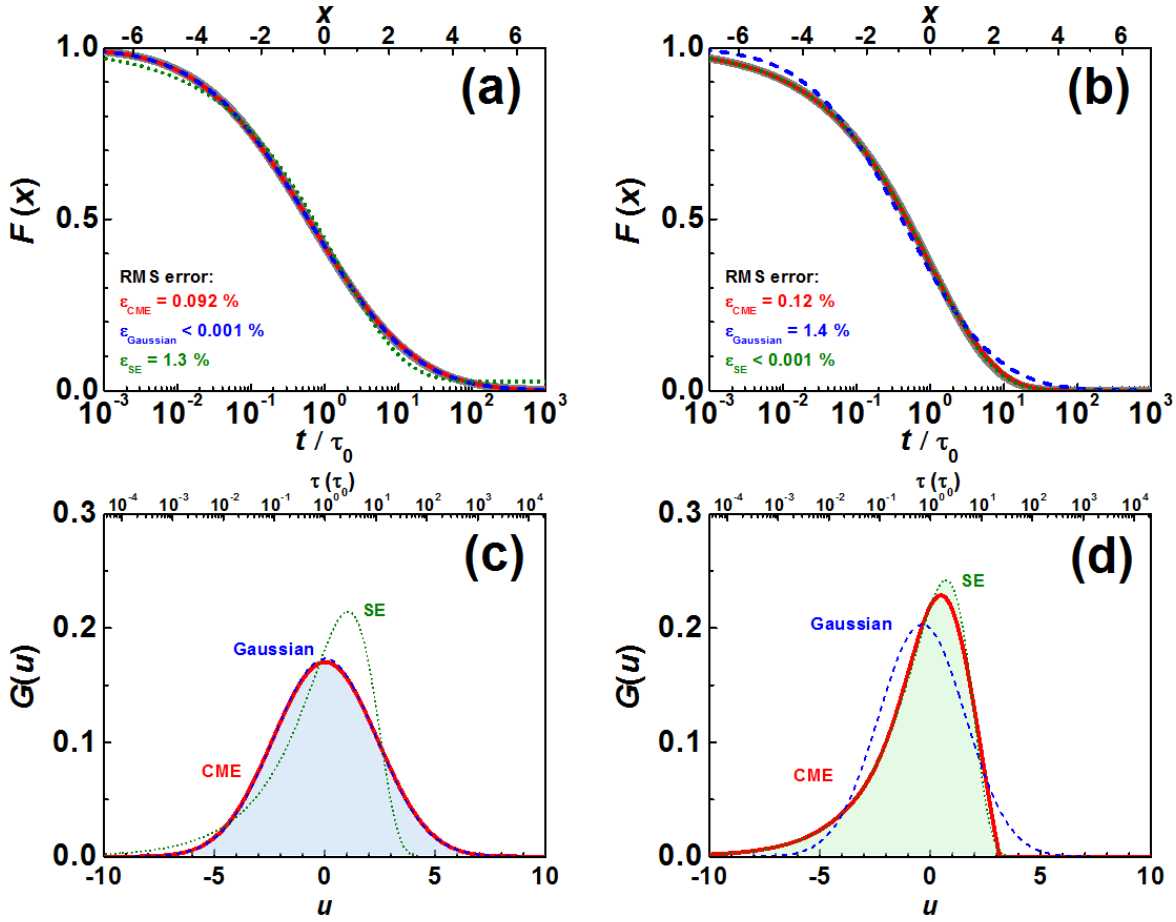

Figure 4.2. (a) Simulated log-scale transient response $F(x)$ (thick gray line) assuming Gaussian distributed spectrum and (b) simulated transient response $F(x)$ (thick gray line) assuming stretched exponential transient, and the fitting results using the continuum multi-exponential (CME) fit (red solid line), the Gaussian distribution fit (blue dashed line), and the stretched exponential (SE) fit (green dotted line). (c) and (d) Decay spectra $G(u)$ corresponding to the fitted responses in (a) and (b), respectively. The model Gaussian spectrum is plotted as the light blue area, and the model SE spectrum is plotted as the light green area.

fit the stretched exponential transient with asymmetric decay spectrum. Therefore, the predictive methods can only be applied when the decay spectrum $G(u)$ structure is known *a priori*.

On the other hand, the descriptive CME method always yields a good fit to the transient response $F(x)$ and reconstructs the correct decay spectrum $G(u)$ as long as the measurement lasts long enough to reach the asymptotic value f_∞. As shown by the red lines in Fig. 4.2(a) and (b), the continuum multi-exponential method correctly fits both datasets with fitting error $\varepsilon \approx 0.1\%$. The decay spectra for the CME fits, plotted as the red lines in Fig. 4.2(c) and (d), can be symmetric or asymmetric to adapt to model decay spectra with any shape.

4.2.5. Convergence trend of fitting methods

In many experiments, the data collection is stopped before the response reaches the asymptotic value f_∞. This subsection discusses the dependence of the accuracy of the fits on the measurement duration.

To test the accuracy of fits that work with restricted datasets of reduced measurement durations t_{meas}, the generated transient data is truncated at $t_{\text{meas}} = 0.1\ \tau_0$, τ_0, $10\ \tau_0$ before applying the fitting methods. Fig. 4.3 shows the decay spectra $G(u)$ obtained with limited measurement durations. In Fig. 4.3(a), for the transient response that assumes a Gaussian distribution as Eq. (4.12), the continuum multi-exponential (CME) descriptive method gives a good approximation to the whole spectrum only after $t_{\text{meas}} = 10\ \tau_0$ when the measurement time exceeds the "mode" or peak in the model spectrum by one order of magnitude, while the Gaussian predictive method fit accurately reconstructs the whole spectrum already at $t_{\text{meas}} = 0.1\ \tau_0$. The incorrect stretched exponential lineshape fails to reconstruct the model Gaussian spectrum regardless of measurement duration. A similar trend is observed in Fig. 4.3(b) in the dataset that assumes a stretched exponential decay

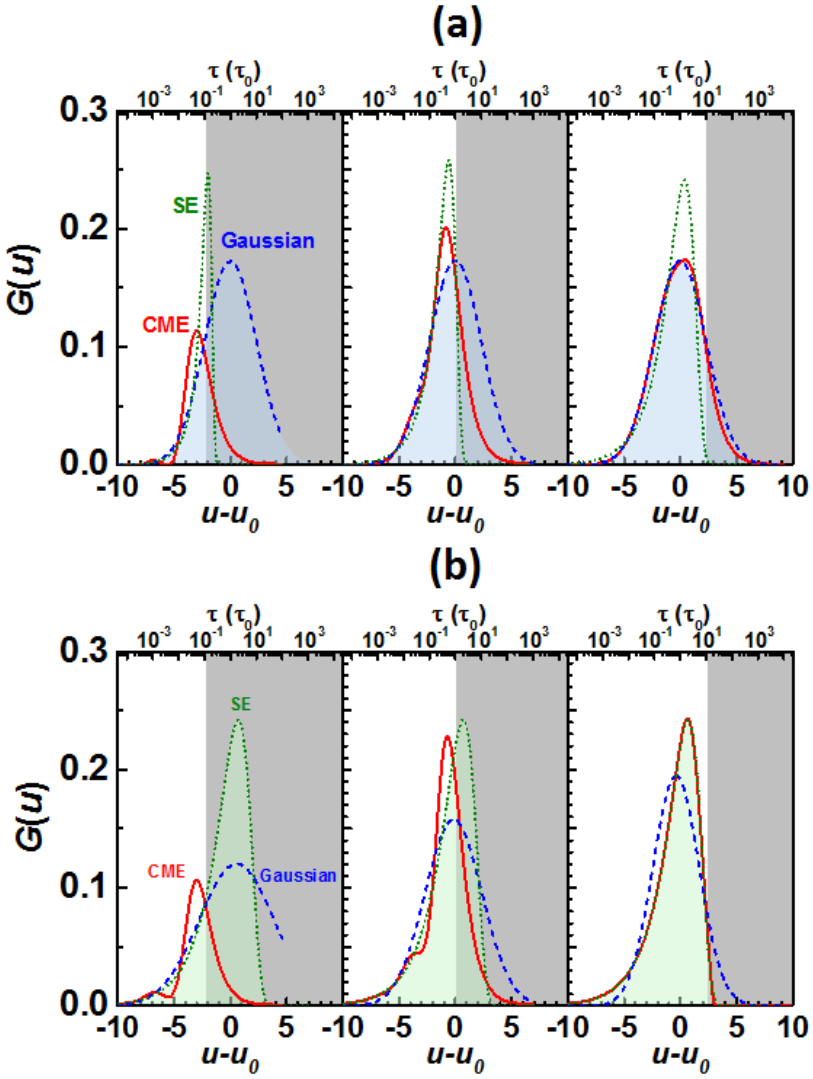

Figure 4.3. (a) Plot of a simulated Gaussian distributed spectrum (light blue area), and (b) of a simulated spectrum associated with the stretched exponential (SE) model (light green area), with curves indicating the decay spectra corresponding to the Gaussian predictive method (blue dashed lines), stretched exponential (SE) predictive method (green dotted lines), and continuum multi-exponential (CME) descriptive method (red lines). Three measurement durations $t_{\mathrm{meas}} = 0.1\ \tau_0,\ \tau_0,\ 10\ \tau_0$ are displayed as white windows from left to right in each panel. When the predictive lineshape matches the simulated data lineshape, the measurement duration can be quite short, only 1/10 of the τ_0 time scale. However, if the predictive lineshape does *not* match the simulated data lineshape, the convergence is poor. The CME method, on the other hand always converges well, but requires a measurement of 10 times τ_0.

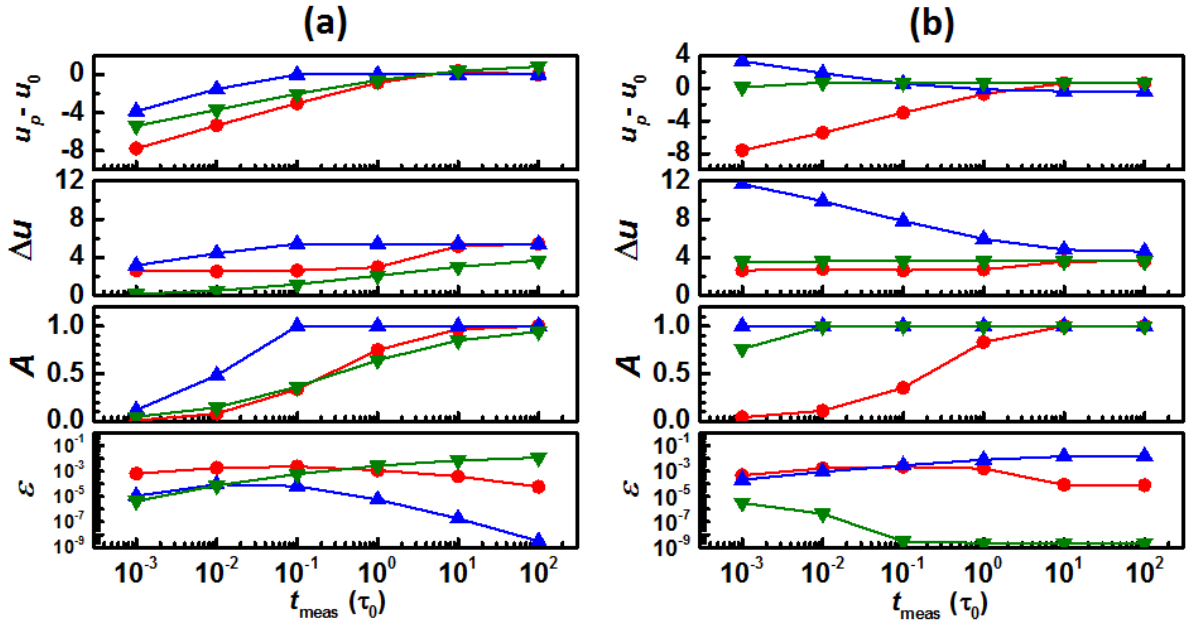

Figure 4.4. Convergence plots: The convergence trend of the decay spectrum shape from the Gaussian predictive method (blue), the stretched exponential (SE) predictive method (green), and the continuum multi-exponential (CME) descriptive model (red) as a function of measurement duration t_{meas} when applied to (a) a transient generated assuming a Gaussian distributed spectrum, and (b) a stretched exponential transient. Lineshape accuracy is identified by the spectral peak position u_p, the linewidth Δu, the integrated area A, and the RMS error ε.

following Eq. (4.14). The CME descriptive method reconstructs the whole spectrum only at $t_{\text{meas}} = 10\ \tau_0$, while the stretched exponential predictive method reconstructs the spectrum even at $t_{\text{meas}} = 0.1\ \tau_0$. The Gaussian predictive method cannot reconstruct the stretched exponential spectrum since it is the wrong lineshape.

The convergence trends of fitted decay spectra as a function of measurement duration t_{meas} using different fitting methods are compared in Fig. 4.4. To graphically illustrate the fitting accuracy of all methods, the lineshape of log-scale decay spectrum $G(u)$ is characterized with three main features: the mode position u_p, full-width-half-maximum

width Δu, and the total spectrum amplitude A. The convergence trends of the RMS fitting error ε are also plotted. When the correct predictive method is used, the fitted decay spectrum converges before $t_{\text{meas}} = 0.1\ \tau_0$, with error ε keeping low. However, when a descriptive method or a wrong predictive method is used, the fitted decay spectrum only starts to converge from $t_{\text{meas}} = 10\ \tau_0$. Since the descriptive CME method can adapt to any decay spectrum shape, the fitting error ε of the descriptive method remains low, while an incorrect predictive method that fails to fit the transient will have a large, non-converging error ε with increasing t_{meas}.

With this convergence trend, we propose an experimental approach for fitting arbitrary non-exponential transients. Here the Gaussian distribution method and stretched exponential method are used as examples, but this approach can be applied to any other predictive method. First, the most accurate predictive method should be identified from candidate models in the literature. Any such predictive method should start to converge at a measurement duration significantly smaller than the mode or peak time constant $\tau_p = \tau^* \mathrm{e}^{u_p}$ in the fitted spectrum $G(u)$, i.e. $t_{\text{meas}} \ll \tau_p$. If a predictive method is not available or needs to be verified, then the descriptive method should be used but will require significantly longer time to converge, namely $t_{\text{meas}} \gg \tau_p$. For a-IGZO system, the estimated measurement duration using descriptive methods can be several months, while using predictive methods can reduce it to several hours. [**86**]

In the next section, a more generalizable analytical method is derived to identify the dominant time constant in the decay spectrum, which is also the minimum useful measurement duration for characterizing a distributed decay response, without having to fit the transient response.

4.3. Semi-log transient plot and log-scale derivative

As shown by Eq. (4.5), transient response $F(x)$ has the convolution form when plotted on the semi-log plot as a function of log-time x. This section will discuss the advantage of semi-log plots and use the properties of convolution integrals to identify experimentally necessary information such as the minimum useful measurement duration directly from transient data plotted on a semi-log scale.

Since Eq. (4.5) has the convolution form, the derivative $F'(x)$ with respect to log-scale time x is also a convolution of $G(u)$ with impulse response $H'(x)$, as shown in Eq. (4.16). Equivalently, higher order derivatives can be expressed as the convolution of $G(u)$ with impulse response $H''(x)$, $H'''(x)\cdots$ *etc.*

$$F'(x) = \int_{-\infty}^{+\infty} G(u)H'(x-u)du \tag{4.16}$$

For transient responses with large time constant components, it is often hard to determine the asymptotic background f_∞ accurately. Solving the decay spectrum $G(u)$ from the derivative form Eq. (4.16) would help increase the accuracy of f_∞ estimation.

The shape of the kernel function $h(t,\tau_0) = e^{-t/\tau_0}$ in Eq. (4.4) and the impulse functions $H(x) = exp[-exp(x)]$ and $-H'(x)$ in Eqs. (4.5) and (4.16) are plotted in Figure 4.5, with the unit time τ^* chosen to be $\tau^* = \tau_0$. The curve of $H(x)$ shows an inflection point at $x = 0$, corresponding to a "unimodal" or single-peak structure of $-H'(x)$. The derivative peak $-H'(x)$ shows integrated area $\int_{-\infty}^{+\infty} -H'(x)dx = 1$, mode position $x_{H,p} = 0$, mode height $-H'(x_{H,p}) \approx 0.37$, and average position $\int_{-\infty}^{+\infty} -x \cdot H'(x)dx = -\text{Eu}$, where Eu ≈ 0.577 is Euler constant. The asymmetric $-H'(x)$ peak has full-width half maximum (FWHM)

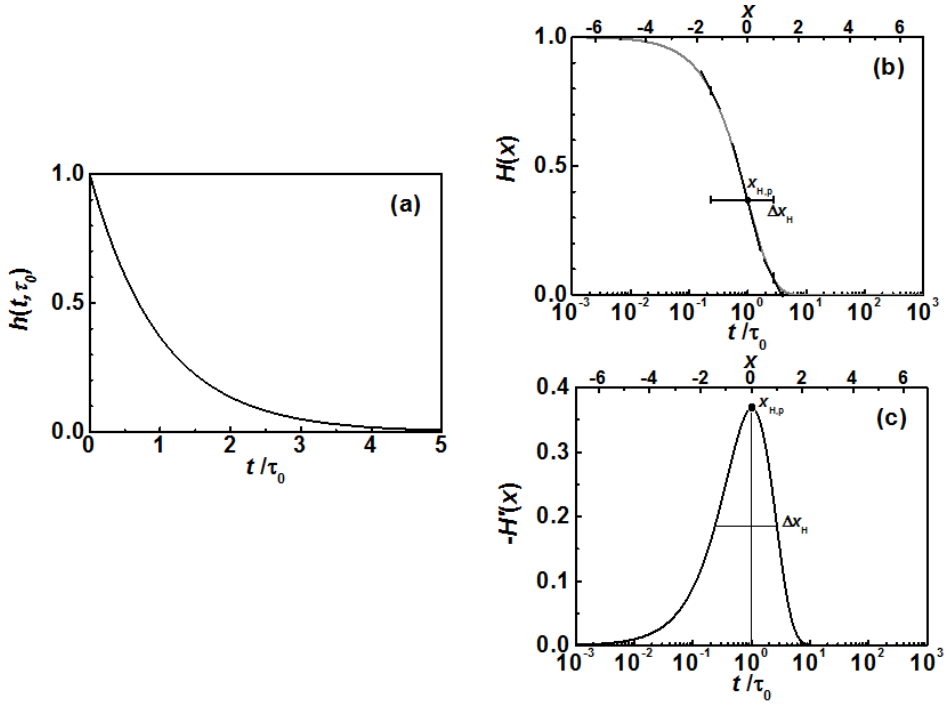

Figure 4.5. Plots of (a) simple exponential decay function $h(t, \tau_0)$, (b) unit decay response $H(x)$ as a function of log-time x, and (c) derivative of unit decay response $-H'(x)$. The derivative peak maximum $x_{H,p}$ is indicated with the solid circle and the vertical line. The width at half maximum is indicated with the horizontal line.

$\Delta x_H \approx 2.45$, with larger asymmetric left width $\Delta x_H^- \approx 1.46$ and smaller right width $\Delta x_H^+ \approx 0.99$.

As shown by Eq. (4.16) and Fig. 4.5, the derivative peak $-F'(x)$ is just the convolution of decay spectrum $G(u)$ with the unimodal impulse response $-H'(x)$. Therefore, $-F'(x)$ would signatures of the lineshape of $G(u)$. To illustrate the connection between the log-scale responses and the decay spectrum shapes, transient responses assuming simple exponential decays (simple), Gaussian-shaped spectrum decays (Gaussian spectrum), and stretched exponential decays (stretched) are generated and compared in Fig. 4.6. All decays assume an initial value $f_0 = 1$ and an asymptotic background $f_\infty = 0$, so that they

all have total response amplitude $A = 1$. The characteristic time constant for all decays are τ_0. The Gaussian distribution spectrum is chosen with a standard deviation $s = \ln 10$, representing a time constant distribution spanning around 2 orders of magnitude, and the stretched exponential decay assumes a stretching exponent $\beta = 0.5$, representing a typical β value reported for stretched exponential decays.

The comparison of the linear-scale response $f(t)$, the semi-log response $F(x)$, the semi-log plot derivatives $-F'(x)$, and the corresponding log-scale decay spectrum $G(u)$ for the generated transient responses are plotted in Fig. 4.6. In Fig. 4.6(a), all decay responses look similar as they all obey Eq. (4.1). Transient responses with distributed time constants (Gaussian spectrum and stretched exponential) show faster decay at short time scales and slower decay at long time scales compared to the simple exponential response. In Fig. 4.6(b), simple exponential clearly shows the steepest decay on the semi-log plot. Any transient response with distributed time constants would have a more gradual decay on the semi-log plot than a simple exponential. Consequently, on the semi-log derivative plot Fig. 4.6(c), simple exponential decay shows the highest peak height with the narrowest peak width. The Gaussian spectrum decay shows a derivative peak that is almost symmetric while the stretched exponential decay shows a peak with heavier tail on the short time side. When deconvoluted to the log-scale decay spectra in Fig. 4.6(d), the Gaussian spectrum is perfectly symmetric while stretched exponential spectrum has a heavier tail with small time constants. The simple exponential decay spectrum is just a delta function, which has the narrowest possible spectrum width 0. The visually identified features of the semi-log derivative peaks and the log-scale decay spectra, namely the peak (mode) position, peak height, and the full-width at half-maximum (FWHM) width

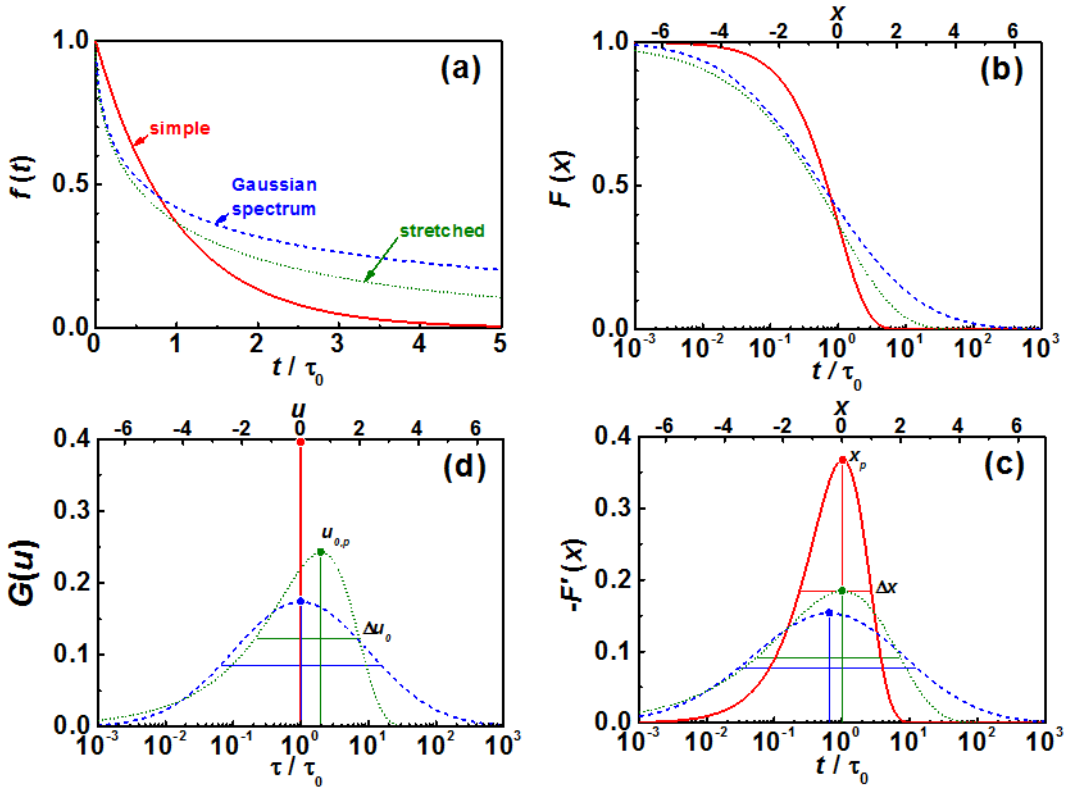

Figure 4.6. (a) Transient responses $f(t)$ following simple exponential (red solid line), Gaussian distributed multi-exponential (blue dashed line), and stretched exponential (green dotted line) in linear time scale t. (b) Transient responses $F(x)$ in (a) plotted in log-time $x = \ln(t/\tau_0)$. (c) The derivative $-F'(x)$ with respect to log-time x. Inflection points x_p in the original semi-log plot appear as maxima in the derivatives in panel (c) and are indicated with solid circles and vertical lines. Full width at half-maximum Δx are indicated with horizontal lines. (d) Time constant distribution spectrum $G(u)$ in log time-constant scale $u = \ln(\tau/\tau_0)$ for transient responses in panels (a) and (b). The solid circles and vertical lines in panel (d) indicate the maxima $u_{0,p}$ in the decay spectra, and the horizontal lines indicate the half-maximum width Δu_0 of the each spectrum.

of each curve, are labeled in Fig. 4.6(c) and (d). The features of the semi-log derivative correspond to analogous features of the log-scale decay spectrum since the derivative

peak $-F'(x)$ is just the convolution of the decay spectrum $G(u)$ with the unimodal impulse function $-H'(x)$. Section 4.4 will exploit this correlation to directly construct an estimated decay spectrum $G(u)$ using those visually identified features of the semi-log derivative peak $-F'(x)$.

Just as with the example transients in Fig. 4.6(b), a general log-scale transient $F(x)$ always has at least one inflection point with $d^2F(x)/dx^2 = 0$. For any transient response $f(t)$ relaxing from a starting value f_0 to an asymptotic value f_∞, the log-scale response $F(x)$ has asymptotic values for $x \to \pm\infty$, as $\lim_{x\to-\infty} F(x) = f_0$ and $\lim_{x\to+\infty} F(x) = f_\infty$. Therefore the derivative $-F'(x)$ also has asymptotic values $\lim_{x\to\pm\infty} -F'(x) = 0$. For a decay transient, $-F'(x) > 0$, thus $-F'(x)$ has at least one maximum, corresponding to an inflection point for $F(x)$. Consequently, since $-F'(x)$ is the convolution of the decay spectrum $G(u)$ and the unimodal impulse response $-H'(x)$, as shown in Eq. (4.16), the log-scale decay spectrum $G(u)$ would also have at least one maximum with asymptotic behavior $\lim_{u\to\pm\infty} G(u) = 0$. Most time constant distributions $G(u)$ reported in literature have a unimodal structure with only one maximum. [**91**] Thus the following discussions will only consider the cases with unimodal $G(u)$ spectra.

The inflection point on the semi-log plot defines the minimum measurement duration needed to give a reliable characterization of a non-exponential transient response. Here we define the log-scale inflection point position as x_p and the corresponding linear time $t_p = \tau^* e^{x_p}$. With measurement duration shorter than t_p, one cannot reliably extrapolate the inflection point position x_p and the derivative at $x > x_p$ without knowing the decay spectrum shape *a priori*. As demonstrated in the section 4.2.5, lack of long term transient

data would cause spurious artifacts in the extracted decay spectrum when using descriptive methods. In contrast, with measurement duration far beyond the inflection point t_p, the large time-scale side of the derivative peak $-F'(x)$ can be more reliably extrapolated from the measured segment of the peak without reaching the asymptotic value f_∞.

Therefore, the best way to represent a non-exponential transient response is on a semi-log plot that plots data as amplitude vs. log t. Many previous reports showed the transient data on linear plots [**20**, **86**, **100**, **101**], log-log plots [**20**, **100**], or log-linear plots with amplitude on log-scale and t on linear scale [**71**]. Those representations of the data make it difficult to identify the inflection point t_p and the spread of time constant distribution Δx, which can result in insufficient data collection and misinterpretation of the transient behavior. On the other hand, the semi-log plots, such as used by Kakalios *et al.*, allow one to identify the dominant time constant τ and the decay spectrum line width Δu dependence on temperature T in a-Si:H thin films. [**89**]

4.4. Introducing the skew normal: Best estimation of time constant distribution

In this section, we propose a new fit function, the skew-normal or skew-Gaussian lineshape, which is more powerful that the Gaussian or stretched exponential alone, and can, in fact, interpolate reasonably well between these two lineshapes with the help of one additional fit parameter to control skewness. Fig. 4.6 and Eq. (4.16) show that the structure of the derivative peak $-F'(x)$ can be correlated with key features of the decay spectrum $G(u)$. Therefore, it is possible to estimate $G(u)$ directly from $-F'(x)$ without

doing data fitting. This section will develop a set of empirical equations to construct an estimated decay spectrum $G(u)$ from a few key visual features of $-F'(x)$.

Several attempts have been made by other authors to estimate the decay spectrum $G(u)$ without using the fitting methods we introduced in Section 4.2. By approximating the convolution impulse function $-H'(x)$ as a delta function, Jackson *et al.* proposed to use $-F'(x)$ directly as a rough estimation of the decay spectrum $G(u)$. [**102**] This method provides a good approximation only when the width Δu of the decay spectrum is significantly wider than the width Δx_H of the impulse function $-H'(x)$, i.e. $\Delta u \gg \Delta x_H$, and the estimated decay spectrum can only achieve a time resolution of order Δx_H. The decay spectrum $G(u)$ was subsequently connected to the log-scale derivative $-F'(x)$ through their moments in log-time by Zorn. [**91**] Using the properties of the convolution integral, Zorn showed that the first, second, and third central moments of the derivative peak $-F'(x)$ in log-time can each be expressed as the sum of the moments of the decay spectrum $G(u)$ added to the corresponding moments of the impulse function $-H'(x)$. Therefore, the moments of the decay spectrum $G(u)$ can be calculated from those of the measured derivative $-F'(x)$, and the decay spectrum can be constructed from the moments. However, calculating the moments of $-F'(x)$ requires a complete measurement of the response from $x = -\infty$ to $+\infty$, corresponding to linear-scale time from $t = 0$ to ∞. In a real experiment, the measurement resolution may not be able to cover the initial response at short times, or the entire tail of the response at long times. Thus the restricted range of any experimentally accessible set of data makes Zorn's method difficult to implement in practice.

Instead, in this section, we propose a more robust way to visually identify four key features to characterize the semi-log derivative $-F'(x)$ and thereby estimate the 4 paramters of the skew-normal distribution. The first feature is the characteristic time scale of the response, characterized by the inflection point position x_p. The second feature is the amplitude of the response, characterized by the height B at the inflection point. The spread of time constant distribution is characterized by the full width at half-maximum Δx of the derivative peak, constituting the third feature. And the asymmetry $1 < \epsilon < 1$ is quantified using the half width Δx^- and Δx^+ of the derivative peak at half-maximum point to the left of x_p and to the right of x_p, respectively, defining the unitless asymmetry $\epsilon = (\Delta x^+ - \Delta x^-)/\Delta x$ as the fourth and final feature needed to characterize the derivative peak $-F'(x)$. With a measurement duration sufficient to estimate the right half-maximum slope point on the semi-log plot, the values for all four features can be identified with an incomplete dataset achieving significant advantage over the method of Zorn.

The skew normal distribution function $G_{SN}(u)$ is defined in Eq. (4.17), with the four parameters A, α, u_0, and s.

$$G_{SN}(u) = \frac{A}{\sqrt{2\pi}} \mathrm{e}^{-\frac{(u-u_0)^2}{2s^2}} \left[1 + \mathrm{erf}\left(\alpha \cdot \frac{u - u_0}{\sqrt{2}s}\right)\right] \tag{4.17}$$

The skew normal distribution function is chosen to estimate the decay spectrum because it has two independent parameters s and α to describe the distribution line width and asymmetry respectively, allowing a single function to approximate most experimentally observed decay spectra which are unimodal (single-peak). Empirical functions that have

been used to fit the decay spectrum or the transient response previously have not included an adjustable asymmetry parameter. [**91**] For example, the Gaussian distribution fit function Eq. (4.12) assumes the spectrum to be symmetric, and the stretched exponential fit Eq. (4.14) assumes a correlation between spectrum width and asymmetry. On the other hand, for the skew normal distribution, spectral line-width is mainly determined by the parameter s, and asymmetry is mainly determined by the parameter α. Other asymmetric distribution functions with four parameters, such as the split normal distribution, [**103**] can also be used to fit the peak shape. However, without introducing more shape parameters, those functions do not necessarily apply to a wider range of decay spectra. [**104**]

What remains, then, is to identify an empirical relation that defines the four skew normal parameters A, α, u_0, and s in terms of the four lineshape measures of the experimental data B, ϵ, x_p, and Δx. For the skew normal distribution function $G_{SN}(u)$, its first $u_{SN,1}$ and second $u_{SN,2}$ central moments can be calculated analytically as shown in Eq. (4.18).

$$u_{SN,1} = \langle u \rangle = u_0 + s\delta\sqrt{\frac{2}{\pi}}, \text{ where } \delta = \frac{\alpha}{\sqrt{1+\alpha^2}} \tag{4.18a}$$

$$u_{SN,2} = \left\langle u^2 \right\rangle - \langle u \rangle^2 = s^2\left(1 - \frac{2\delta^2}{\pi}\right) \tag{4.18b}$$

Combining the moments of the skew normal distribution $G_{SN}(u)$ with the relationship between the moments of the decay spectrum $G(u)$ and log-scale derivative $-F'(x)$ shown by Zorn, here we developed a set of empirical equations to find the skew normal fitting parameters of the decay spectrum from the derivative peak features, Eqs. (4.19), where

$-\mathrm{Eu} \approx -0.5772$ is mean position of the impulse response $-H'(x)$, and $\epsilon_H \approx -0.192$ is the asymmetry of the impulse response $-H'(x)$.

$$\delta(\epsilon, \Delta x) = \left\{ \left[(\epsilon - \epsilon_H) \frac{\Delta x^2}{\Delta x^2 - \Delta x_H^2} + \epsilon_H \right] / 0.173 \right\}^{1/5} \tag{4.19a}$$

$$\alpha(\epsilon, \Delta x) = \delta(\epsilon, \Delta x) / \sqrt{1 - \delta(\epsilon, \Delta x)^2} \tag{4.19b}$$

$$s(\epsilon, \Delta x) = \sqrt{\frac{\Delta x^2 - \Delta x_H^2}{8 \ln 2 [1 - 2\delta(\epsilon, \Delta) x^2 / \pi]}} \tag{4.19c}$$

$$u_0(x_p, \epsilon, \Delta x) = x_p + \mathrm{Eu} \cdot \frac{\Delta x^2 - \Delta x_H^2}{\Delta x^2} - \sqrt{\frac{2}{\pi}} s \cdot \mathrm{erf}\left[\delta(\epsilon, \Delta x) \frac{\sqrt{\pi}}{2} \right] \tag{4.19d}$$

$$A(B, \Delta x) = B \cdot \Delta x / 0.93 \tag{4.19e}$$

The above equations have been empirically identified as described below. The asymmetry parameter δ and therefore α of $G_{SN}(u)$ is directly estimated from ϵ and Δx in the log-scale derivative $-F'(x)$ with Eq. (4.19b). For very wide spectra, $-F'(x)$ has almost the same asymmetry as $G_{SN}(u)$; and for very narrow spectra, $-F'(x)$ has almost the same asymmetry as $-H'(x)$. This justifies the weighting factor $\frac{\Delta x^2}{\Delta x^2 - \Delta x_H^2}$ that is multiplied to ϵ in Eq. (4.19a). The width parameter s of $G_{SN}(u)$ increases with the width of $-F'(x)$ following the empirical Eq. (4.19c), where the factor $\sqrt{8 \ln 2}$ is the ratio between FWHM and standard deviation in Gaussian distribution, and the factor $\sqrt{1 - 2\delta^2/\pi}$ in the denominator of Eq. (4.19c) is the ratio between the standard deviation and the width parameter s in skew normal distribution in Eq.(4.18b). The position parameter u_0 of $G_{SN}(u)$ in Eq. (4.19d) is estimated from the mean position (first central moment $u_{SN,1}$ in Eq.(4.18a)) of $G_{SN}(u)$ and the mean position difference Eu between $G_{SN}(u)$ and $-F'(x)$. As shown by Eq.(4.20), the integrated amplitude A of $G_{SN}(u)$ equals to the integrated

amplitude of $-F'(x)$, which is approximated by the product of mode height B and FWHM width Δx of $-F'(x)$, giving the empirical Eq. (4.19e).

$$\int_{-\infty}^{\infty} -F'(x)dx = \int_{-\infty}^{\infty} G_{SN}(u)du \int_{-\infty}^{\infty} -H'(x)dx = \int_{-\infty}^{\infty} G_{SN}(u)du = A \tag{4.20}$$

The empirical Eqs. (4.19) have been tested with datasets assuming the Gaussian spectrum as well as the stretched exponential function. Several different values for the width parameter s in the Gaussian spectra and the stretched exponent β in the stretched exponential transients are used to generate model spectra with different widths and shapes. Fig. 4.7 shows comparison of the approximated skew normal spectra (gray lines) using the empirical Eq. (4.19) with the model spectra (blue and green lines) used to generate the test transient responses. For all model spectra assuming a Gaussian shape, Eq. (4.19) constructs skew normal spectra that have over 90 % overlapped area with the model spectra. The same level of accuracy is also achieved for model spectra assuming a stretched exponential transient except when $\beta \to 1$. As $\beta \to 1$, the spectrum width $\Delta u \to 0$, thus the structure of the derivative peak $-F'(x)$ is mainly determined by $-H'(x)$ instead of $G(u)$, making it hard to accurately estimate the $G(u)$ structure from $-H'(x)$. Nevertheless, for all model spectra shapes, the estimated skew normal spectra have less than 3 % error for the integrated spectral amplitudes.

4.5. Analysis of long term transient photoresponse in a-IGZO

The data analysis methods developed in the previous section will be applied to analyze the long-term transient photoresponse measured in a-IGZO thin film samples. The 5 mTorr capped sample is used here as a example.

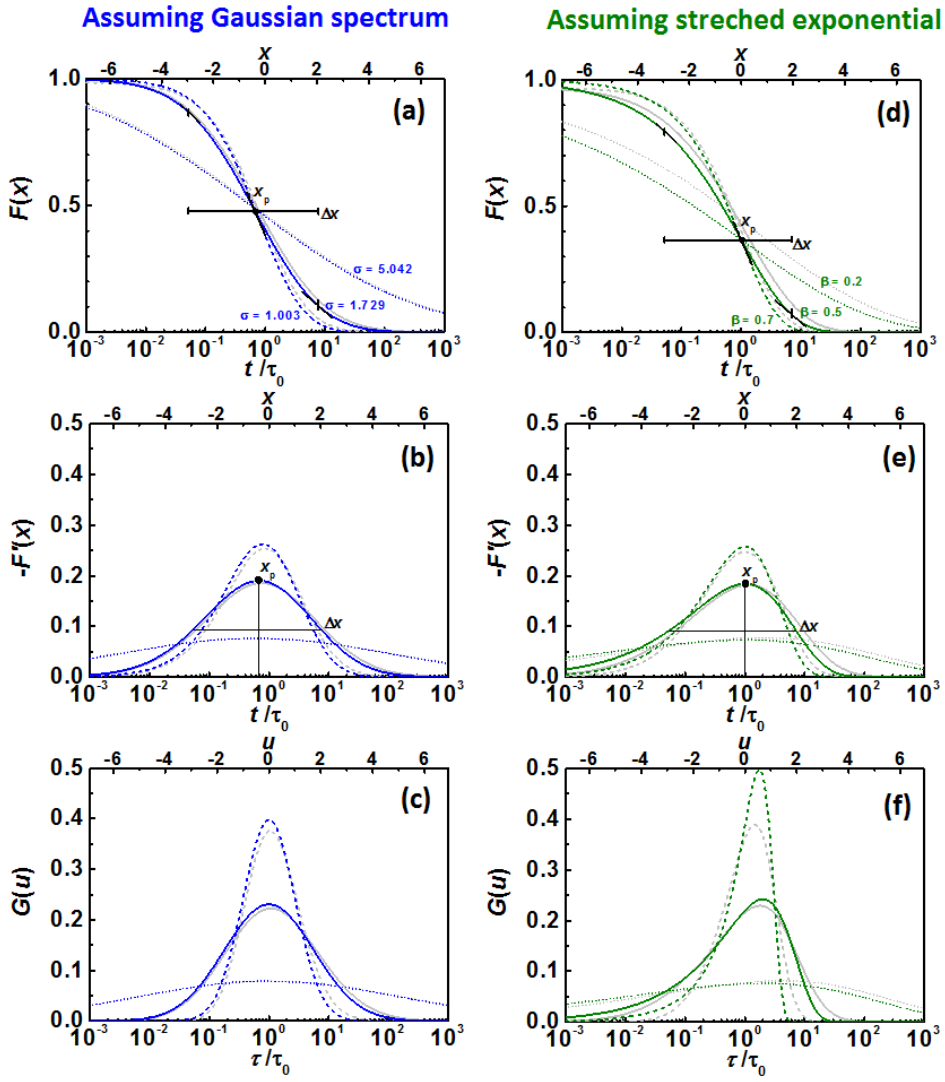

Figure 4.7. (a-c) Comparison of the skew normal (SN) distribution spectra with the Gaussian distributed spectra with the width parameter $s = 1.003$, 1.729, and 5.042 respectively. (d-f) Comparison of the skew normal (SN) distribution spectra with the Gaussian distribution spectra with the SE shape parameter $\beta = 0.7$, 0.5, and 0.2 respectively. The semi-log response $F(x)$, semi-log derivative $-F'(x)$, and log-scale spectrum $G(u)$ of the model Gaussian spectrum transients are plotted as the blue lines, and those of the model stretched exponential transients are plotted as the green lines. All corresponding skew normal fits are plotted as the light gray lines and in general show the ability to provide excellent fits to both the Gaussian and stretched exponential lineshapes.

Fig. 4.8(a) and (b) shows the transient responses of photo-excitation and dark relaxation on semi-log plots. Even though the transients seems to be approaching their asymptotic value when plotted as a function of linear-scale time in Fig. 4.1, the semi-log plots clearly indicate that both transients are still far from the steady state values. Fig. 4.8(c) and (d) shows the semi-log derivative of photo-excitation and dark relaxation as the red lines. The dark relaxation is yet to reach the inflection point, while the photo-excitation has clearly passed the inflection point x_p, but not yet the right half-maximum point. The right half width Δx^+ can still be estimated by extrapolating the semi-log derivative plot. From Fig. 4.8(c), the visual features of the derivative peak are $x_p = 12.97$, $B = 24.55$ S/cm, $\Delta x^- = 1.8$, and $\Delta x^+ = 2.82$. Therefore, $\Delta x = \Delta x^- + \Delta x^+ = 4.62$, and $\epsilon = (\Delta x^+ - \Delta x^-)/\Delta x = 0.22$. The fact that $\Delta x > \Delta x_H = 2.45$ clearly indicates the existence of distributed time constants.

By putting the values of the visual features into Eq. (4.19), parameters of the skew normal distribution spectrum can be calculated as $\alpha = 4$, $s = 2.63$, $u_0 = 11.95$, and $A = 122$ S/cm. Fig. 4.8(e) shows the log-scale decay spectrum estimated assuming a skew normal distribution. An asymmetry spectrum with a heavier tail on the large time constant side and mode time constant around 5×10^5 s is expected. From the skew normal spectrum, the asymptotic steady state conductivity under illumination is estimated as 256 S/cm. Transient photoconductivity and its log-scale derivative following the estimated skew normal spectrum are plotted in Fig. 4.8(a) and (c) as the orange lines. Note there is a small bump in the measured log-scale derivative at around 3×10^3 s in Fig. 4.8(c). This bump does not affect the main peak position nor width, thus is not

reconstructed in the skew normal spectrum. However, it causes an underestimated skew normal photoconductivity as shown in Fig. 4.8(a).

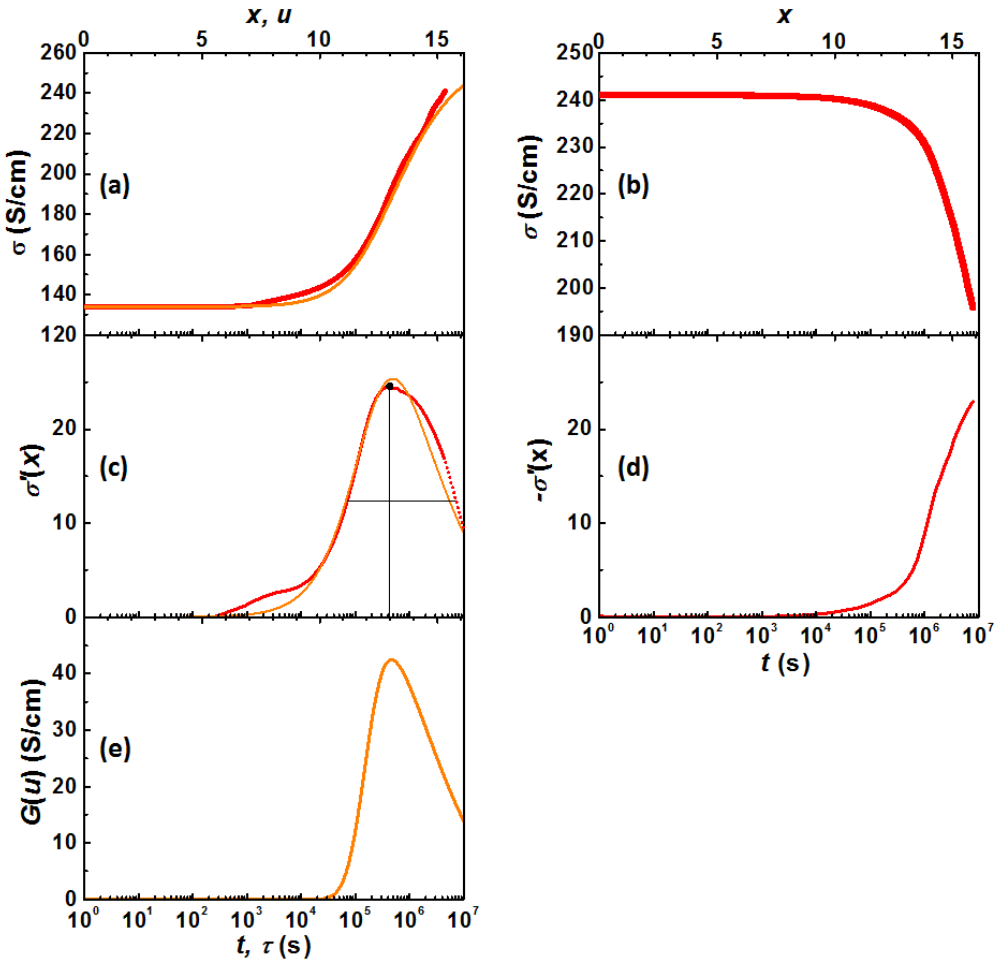

Figure 4.8. (a) Semi-log plot of measured transient photoconductivity of the 5 mTorr capped sample during photo-illumination (thick red line) and the transient photoconductivity corresponding to the estimated skew normal decay spectrum (thin orange line). (b) Semi-log plot of transient photoconductivity of the 5 mTorr capped sample during dark relaxation. (c) Derivative of the semi-log photo-excitation transient plots in (a). Both the measured derivative (thick red line) and the derivative from the estimated skew normal decay spectrum (thin orange line) are plotted. The maximum derivative point in the measured derivative is indicated by the solid circle and the vertical line. The half-maximum derivative points are indicated by the horizontal line. (d) Derivative of the semi-log dark relaxation transient plot in (b). (e) Skew normal decay spectrum of the photo-excitation transient plot in (a), estimated using the empirical Eq. (4.19).

CHAPTER 5

Physical Mechanisms for Transient Photoresponse in a-IGZO

This chapter discusses how the stretched exponential function empirically fits the measured photoresponse, and which physical mechanisms possibly lead to the stretched exponential response. Section 5.1 introduces the stretched exponential function, which describes both the short-term and long-term transient photoresponse in a-IGZO in a single function. Section 5.2 analyzes the stretched exponential transients using the distributed time constant method discussed in Chapter 4. Section 5.3 and 5.4 introduce two contrasting physical models that can explain the experimentally observed stretched exponential responses, the first assuming distributed activation energies and the second a continuous-time random walk process, respectively. Section 5.5 reviews microscopic mechanisms for the a-IGZO photoresponse proposed in literature, and discusses why they may not explain the observed stretched exponential transients. Based on molecular dynamics simulation results and the continuous-time random walk model, a possible microscopic mechanism is then proposed to explain the stretched exponential photoresponse in a-IGZO.

5.1. Stretched exponential fit for transient photoresponse in a-IGZO

The stretched exponential function is given by

$$f(t) = f_\infty + A\mathrm{e}^{-(t/\tau_0)^\beta}, \tag{5.1}$$

where $f(t)$ evolves towards an equilibrium asymptotic value f_∞ in response to a sudden change of the excitation.

On the semi-log plot, the log-scale equation for the stretched exponential function is given by

$$F(x) = f_\infty + A \cdot H[\beta(x - u_0)], \tag{5.2}$$

where $x = \ln(t/\tau^*)$ is log-scale time with unit time scale defined as τ^*, $u_0 = \ln(\tau_0/\tau^*)$ is the characteristic log-scale time constant, and $H(x) = \mathrm{e}^{-e^x}$ is the simple exponential function $\exp(-t/\tau^*)$ plotted with respect to log-scale time x.

There are three fit parameters in the stretched exponential function. Parameter A is the total response amplitude, which is also the integrated decay spectrum density when analyzed as distributed time constants. The asymptotic value f_∞ is determined from A using the initial value f_0 at $t = 0$.

$$f_0 = f(t = 0) = f_\infty + A \tag{5.3}$$

Parameter τ_0 is the characteristic time constant, which is also the inflection point of the transient when plotted on a semi-log plot versus $\log t$. However, it is not the average time constant of the decay spectrum, nor the most probable time constant. [**90**] Parameter β is the stretching exponent, constrained to be $0 < \beta \leq 1$. When $\beta = 1$, the stretched exponential reverts to the simple exponential.

To understand the parameter dependence of the stretched exponentials, transient responses with various β values simulated and compared. Stretched exponential responses can be normalized to have unit amplitude. Transients with different characteristic time

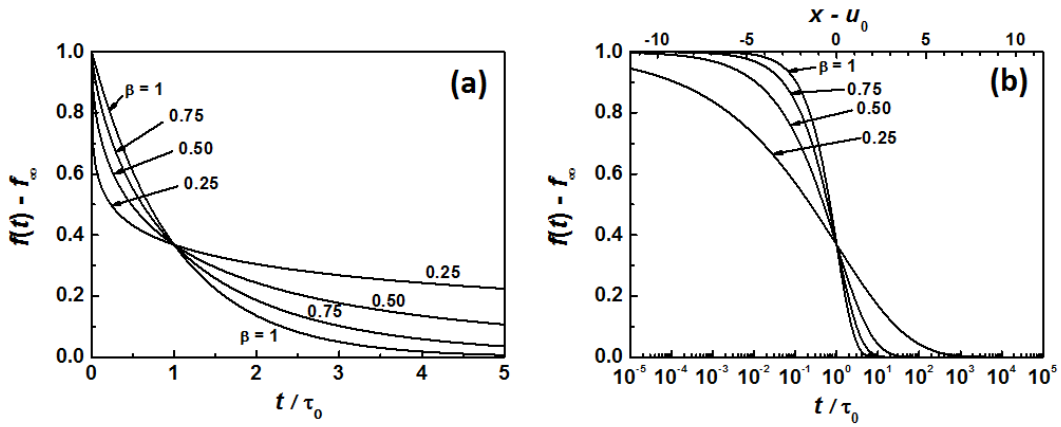

Figure 5.1. The stretched exponential responses for $\beta = 1$, 0.75, 0.50, and 0.25, respectively. The transient responses are plotted versus linear time t in (a) and log-scale time x in (b). Note that the stretched exponential curves in (b) have the same shape as the simple exponential curve with $\beta = 0$, except linearly stretched by a factor of $1/\beta$.

constant τ_0 can also be normalized on the time axis to have unit characteristic time constant, which is equivalent to a horizontal translation on the semi-log plot versus log t. Thus all simulated responses assume a unit response amplitude $A = 1$, and the characteristic time constant τ_0 is used as a reference on the time axes. The stretching exponent β is the only remaining shape parameter for the transient response curve and the decay spectrum.

Fig. 5.1 plots the simulated transient responses as a function of linear time t and log time $x = \ln(t/\tau^*)$. All stretched exponential transients relax to $1/e$ of the initial amplitude at the characteristic time constant τ_0. Smaller β values would make the transient faster at all time scales smaller than τ_0, and slower at all time scales larger than τ_0. By calculating the derivative of the linear-scale transient $f(t)$, it is clear that the stretched exponential has infinite derivative at $t = 0$ for all $\beta < 1$. Comparing the stretched exponential transients with $0 < \beta < 1$ to the simple exponential transient with $\beta = 1$, it is clear from

Eq. (5.1) that the scaling factor β within the argument of H results in the semi-log plots with different β being the same as a simple exponential decay scaled or "stretched" by a factor of $1/\beta$ around u_0.

The stretched exponential function has been widely used to describe many non-exponential transient responses. The first application can be dated back to 1854 when R. Kohlrausch applied it to describe the charge decay of a capacitor. [**105**] His son F. Kohlrausch later applied the same function to describe mechanical relaxation in glass fibers. [**106**] In 1970, Williams and Watts rediscovered the stretched exponential function to empirically fit the time evolution of dielectric relaxation, which was previously analyzed in the frequency-domain by assuming a dielectric constant with real and the imaginary frequency dependencies. [**107**] Thus the stretched exponential function is also referred to as the Kohlrausch function or the Kohlrausch-Williams-Watts function in literature. [**108**] Since then, the stretched exponential function has been adapted to empirically fit non-exponential transients in many different systems. For example, the structural relaxation in glassy materials, [**109**] the defect generation and relaxation in a-Si, [**89**,**110**] the threshold voltage drift in amorphous oxide thin film transistors, [**60**,**111**] the photoconductivity in amorphous oxide thin films, [**71**,**86**] and even the survival probability evolution in stock market [**112**] are all found to follow the stretched exponential function.

The stretched exponential function can also be applied to fit the transient photoconductivity measured in a-IGZO thin films. Fig. 5.2 shows the fit results for the capped 50 nm a-IGZO thin film sample deposited at $P_{O_2} = 5$ mTorr. For both the photo-excitation and dark relaxation transients, the stretched exponential function shows a good fit over

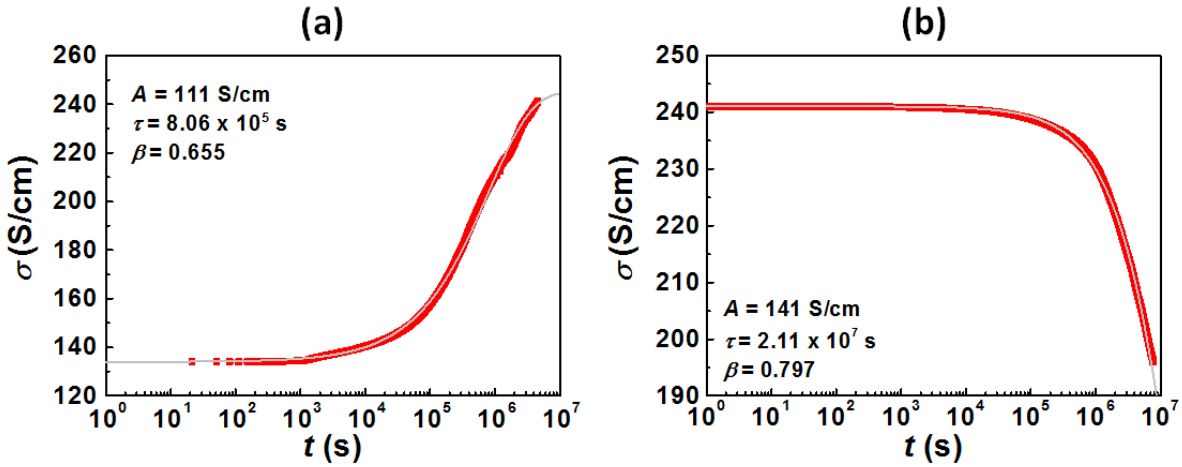

Figure 5.2. Stretched exponential fit for transient responses measured in the 50 nm capped 5 mTorr sample. Panel (a) shows the photo-excitation transient, and panel (b) shows the dark relaxation transient. The measured transient photoconductivities are plotted as the red squares, and the stretched exponential fittings are plotted as the gray lines.

time scales of almost 7 orders of magnitude, ranging from $t < 1$ s to 7×10^6 s (around four months), using only three fit parameters.

5.2. Time constant distribution of the stretched exponential transients

Transient responses following the stretched exponential function satisfy Eq. (4.1), thus can be analyzed using the distributed time constant method introduced in Chapter 4. With the analytical expression for the transient response $f(t)$ as in Eq. (5.1), the time constant distribution $g(\tau)$ and $G(u)$ can be directly calculated through numerical inverse Laplace transformation of Eq. (5.1). [**98**]

The semi-log decay spectra $G(u)$ for stretched exponentials with different β values are compared in Fig. 5.3(a), and an empirical relation is proposed to relate the linewidth Δu to the exponent β. When $\beta = 1$, the spectrum is simply a delta function with all spectral

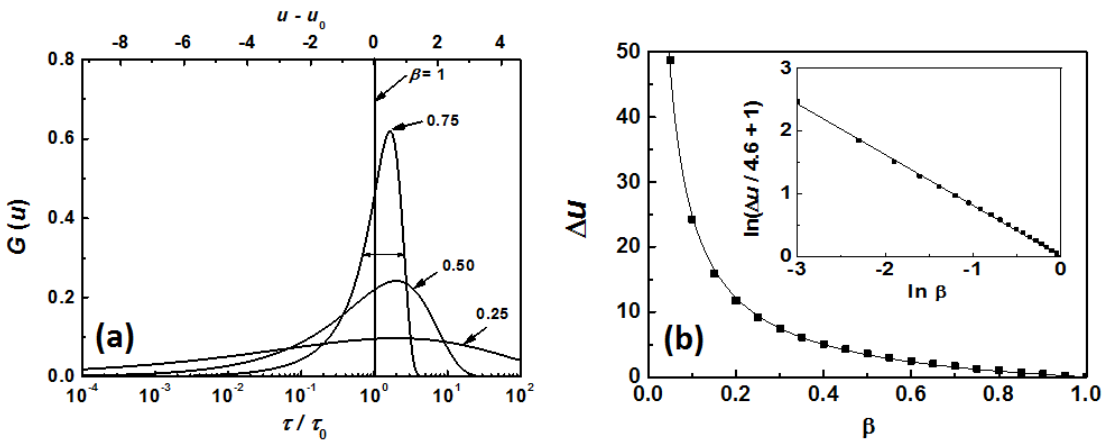

Figure 5.3. (a) Log-scale time constant distribution $G(u)$ corresponding to stretched exponential responses with different β values. The left-right arrow indicates the full-width at half-maximum linewidth Δu. (b) Dependence of Δu on the β values for stretched exponential responses. Squares are calculated directly using inverse Laplace transform and the solid line is the empirical relation in Eq. (5.4). The inset shows how well the empirical fit matches the calculated spectrum linewidths on a log-log scale.

density concentrated at $u_0 = \ln(\tau_0/\tau^*)$. When β decreases, the spectrum expands to have a wider distribution. All $\beta < 1$ distributions show an asymmetric shape with a longer tail on the short time constant side. The spread of the time constant distribution can be characterized by the full-width at half maximum (FWHM) Δu of the decay spectrum. As plotted in Fig. 5.3(b), Δu decreases monotonically with increasing β. Thus Δu and β for a stretched exponential can be directly estimated from each other. The correlation between β and Δu can be approximated by a simple empirical equation as Eq. (5.4), which has error within 8% for any β in the range $0.05 < \beta \leq 1$. The log-log inset to Fig. 5.3(b) illustrates the accuracy of Eq. (5.4).

$$\Delta u = 4.6\left(\beta^{-0.81} - 1\right) \tag{5.4}$$

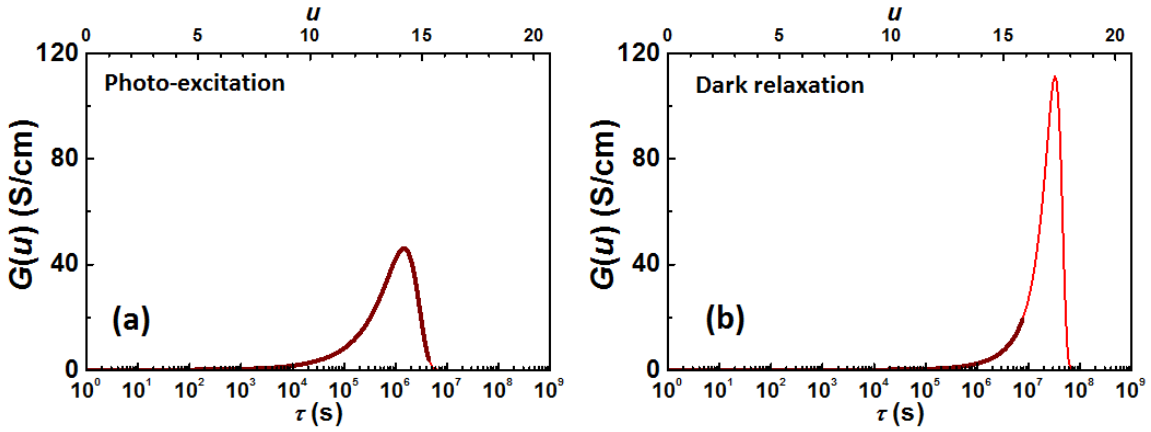

Figure 5.4. Log-scale decay spectra $G(u)$ for the stretched exponential fittings to transient photoconductivity during (a) photo-excitation and (b) dark relaxation in the 50 nm capped 5 mTorr a-IGZO sample. The decay spectra are deduced from inverse Laplace transforms of stretched exponential fittings. The dark red segments of the curves correspond to the time scales with directly measured responses, and the red segments correspond to an extrapolation following the stretched exponential function beyond the measured time scales.

Note that although the characteristic time constant τ_0 is the inflection point for the semi-log transient, it cannot be directly identified from the visual features of the decay spectrum.

The distributed time constant analysis is also applied to the stretched exponential fits to the photoresponse in the capped 5 mTorr a-IGZO thin film sample, as shown in Fig. 5.4. The segments with dark red color indicate the time scales that are directly measured, while the segments at larger time scales are extrapolated using the stretched exponential function. Note that for the dark relaxation transient, the directly measured time range only covers a small portion of the total spectrum, but nonetheless the stretched exponential function provides a reasonable extrapolation, and predicts a smooth spectral shape with the most probable time constant much larger than the measurement duration.

The stretched exponential fit allows extrapolation of the photoresponse to longer time scales. The original experimental data were taken between $t_{\min} = 30$ ms and $t_{\max} \approx 7 \times 10^6$ s (3 months), while the stretched exponential fit predicts decay components with time scale up to 6×10^7 s (2 years) as shown in Fig. 5.4. The advantage of the stretched exponential fit is that it has been verified up to month-long time scale in amorphous systems. [**89**, **95**, **110**] Thus, photoresponse at times shorter than $t_{\min}$ or longer than $t_{\max}$ can be extrapolated by at least an order of magnitude. One can therefore estimate the time constant distribution over a broader range than that is directly measurable. Extrapolating further by orders of magnitude allows one to predict even the peak and the linewidth of the dark relaxation decay spectrum, though this result may be more speculative. Note that a direct measurement to the half maximum of the photo excitation spectrum on the large time constant side would have required 5 weeks, and a measurement of the same features of the dark relaxation spectrum would have required 18 months. Thus, the stretched exponential fit establishes a time-saving protocol for predicting the decay spectrum of transients with extremely slow time constant components in their distribution.

It is worth noting that an accurate decay spectrum requires proper estimation of the asymptotic value f_∞. Due to the extremely slow response of the photoconductivity, the asymptotic conductivity cannot be simply assumed to be the initial dark value as proposed previously, [**20**] since the as-grown samples may not be at equilibrium. The best way to assess the asymptotic value is with a time-dependent study and a stretched exponential line fit as described above. For a transient response with a large characteristic time constant τ_0, most of the spectral weight is found at time scales much longer than

the measurement duration. Underestimating the total response amplitude will cause the decay spectrum to be artificially cut off at time scales around the measurement duration.

5.3. Distributed activation energy model

The distributed time constants observed in non-exponential transients have been previously modeled by some groups as being physically the result of distributed activation energies. [**20**, **113**] IF one considers a thermally activated relaxation process to a state with a binding energy E, the relaxation time constant τ would have a one-to-one correspondence with the energy level E through the reciprocal of an activated rate equation shown in Eq. (5.5), in which ν is the attempt-to-escape frequency, assumed to be the same for all activation energies, k_B is Boltzmann's constant, and T is the temperature.

$$\tau = \frac{1}{\nu} \mathrm{e}^{E/k_B T} \tag{5.5}$$

Thus the log-scale decay constant u is thus linearly related to the activation energy E.

$$u = \ln \tau = E/k_B T - \ln \nu \tag{5.6}$$

With different assumptions for the ν value, the activation energy distributions $D(E)$ will shift to higher or lower energy levels, while the distribution shape, height, and linewidth will remain the same. In such a model, $D(E)$ will be directly proportional to the conductivity decay spectrum $G(u)$ according to Eq. (5.7), where μ is the carrier mobility.

$$D(E) = \frac{1}{k_B T} \frac{G[u(E)]}{\mu e} \tag{5.7}$$

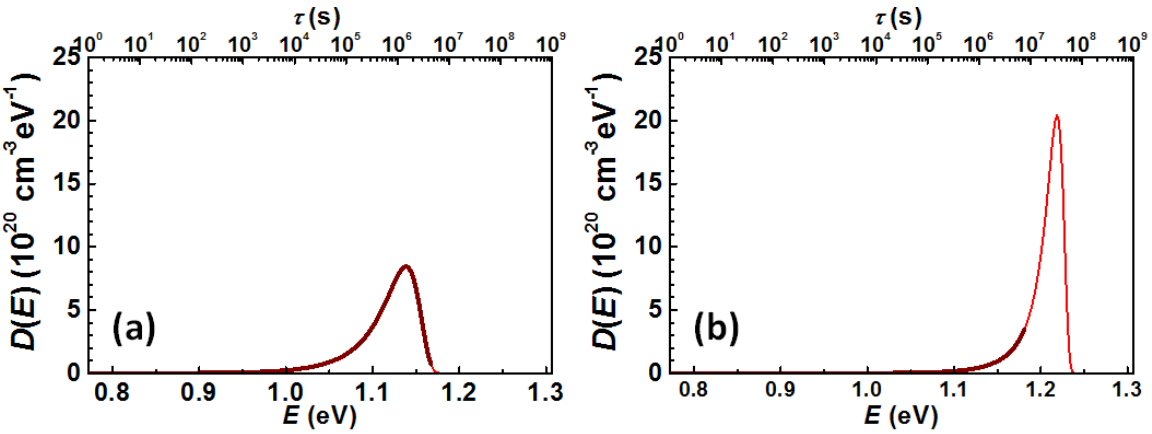

Figure 5.5. Assuming the distributed activation model, one can plot the density of state (DOS) distributions $D(E)$ for the stretched exponential fittings to the transient photoconductivities in the capped $P_{O_2} = 5$ mTorr sample. E indicates binding energy below the mobility gap, such that states to the right would be more deeply bound. Panel (a) shows the DOS for photo-excitation and panel (b) for dark relaxation. The segments with dark red color indicate energy ranges with time constants that were directly measured. The DOS distributions are derived assuming the attempt-to-escape frequency $\nu = 10^{13}$ Hz.

Following the distributed activation energy model, DOS distributions for the transient photoconductivities in the 5 mTorr capped a-IGZO sample can be calculated. Fig. 5.5 shows the DOS for photo-excitation and dark relaxation calculated using their stretched exponential fittings. Here we assume the attempt-to-escape frequency to be $\nu = 10^{13}$ Hz, the same as the phonon frequency, [**86**, **87**] and consistent with a previous report on a-IGZO TFTs that also suggested ν to be between 10^{12} and 10^{13} Hz. [**96**] The DOS distributions are calculated with en electron mobility $\mu = 17$ cm^2/Vs, which is the average Hall mobility we measured in PLD-grown a-IGZO thin films deposited at $P_{O_2} = 5$ mTorr.

The stretched exponential fits in Fig. 5.4 are inverse-Laplace transformed here instead of using the directly measured transients so that the DOS distributions at large energy

levels can be extrapolated. Because of the linear correlation between the log-scale decay spectrum $G(u)$ and DOS distribution $D(E)$, extending the density of states $D(E)$ by a larger energy interval requires measuring the transient response spectrum $G(u)$ for exponentially longer time scales. For activation energies lower than the critical level, reasonable DOS distribution $D(E)$ can be obtained directly from measure data, while for activation energies higher than that, $D(E)$ can only be obtained through extrapolation. Energy ranges are indicated by the dark red segments in Fig. 5.5 where the $D(E)$ energy scale is supported by the measured data log-time scale $G(u)$. At higher energies, the light red segment indicates extrapolation assuming the validity of the stretched exponential fit. Under this model, the DOS related to the photo-excitation would have a wide peak around 1.13 eV, while the DOS related to the dark relaxation would have a narrow peak around 1.21 eV. Other reports on a-IGZO photoresponse assuming the same model also arrived at activation energies distributed between 0.9 eV and 1.2 eV. [**20**, **96**]

The distributed activation energy model has been applied in previous reports to explain the non-exponential transient responses in the a-Si system. Stutzman *et al.* measured the photo-induced defect density transients and related the transients to the distributed activation energies. With a proper choice of the attempt-to-escape frequency ν value, transients measured at different temperatures can be explained by the same activation energy distribution, as shown in Fig. 5.6. [**113**] Deane *et al.* applied the same analysis to the bias-induced threshold voltage shift measured in a-Si TFTs, and argued that one activation energy distribution could explain the data measured over a wide range of time scales ($1 < t < 10^5$ s) and temperatures ($303 < T < 403$ K). [**114**]

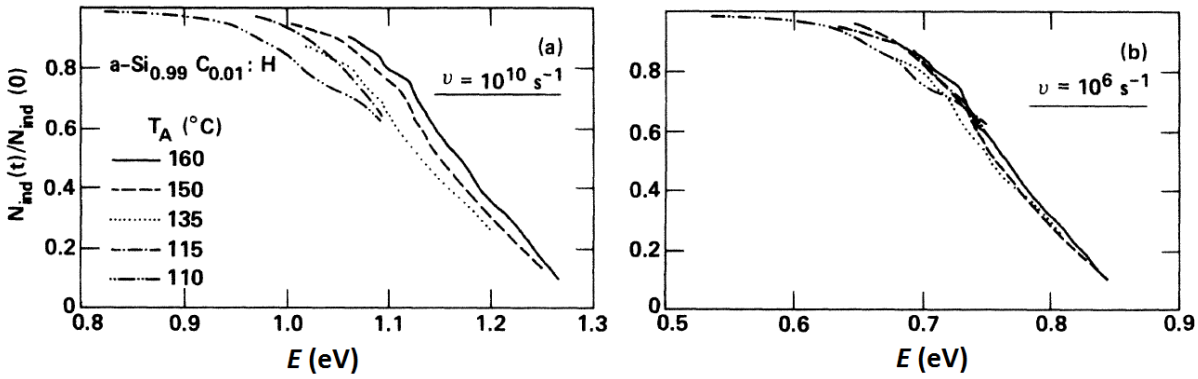

Figure 5.6. Normalized decay curves for photo-induced defect density in a carbon-doped a-Si:H sample at various annealing temperatures T_A as measured by Stutzman *et al.* [**113**] Following the distributed activation energy model, the decay curves are plotted as a function of activation energy E assuming the attempt-to-escape frequency to be (a) $\nu = 10^{10}$ s^{-1}, and (b) $\nu = 10^{6}$ s^{-1}. On those plots, the activation energy distributions $D(E)$ are the derivatives of the decay curves with respect to E. With $\nu = 10^{6}$ s^{-1}, all annealing temperatures yield the same decay curve, indicating a correct choice of frequency scale ν.

The distributed activation energy model can be applied to any transient response with distributed time constants. But it does not give any insights to the origin of the states with such activation energies, other than to indicate what their energetic distribution would be. Strikingly, however, for the commonly observed stretched exponential transients, the distributed activation energy model always predicts asymmetric DOS distributions with longer tails on the low energy side and a more abrupt cut-off on the high energy side. There is no obvious physical reason for why such an energetically asymmetric distribution should be universally observed in so many disordered systems. In an amorphous system, one would have expected a statistically broadened Gaussian lineshape to the DOS instead. The lack of a physical explanation for this asymmetric lineshape presents the principle argument *against* the distributed activation energy model, requiring further exploration

as to fundamental physical mechanisms that might give rise to a stretched exponential time response. We are not the only authors to reach this verdict against the likelihood of an activated DOS model, quoting Kakalios, *et al.* [**89**]

> This [activation energy model] yields an asymmetric distribution in E... However, there is no obvious reason why this distribution of relaxation times results in a stretched-exponential decay of electronic properties, nor does it give any insight into the [physics]... Moreover,... there is no universal or natural connection [underlying] this distribution of relaxation times...

The next section will review the continuous-time random walk model which can provide a physical basis for the stretched exponential transients assuming a more physically reasonable exponential tail of trap states.

5.4. Continuous-time random walk model

The continuous-time random walk (CTRW) model reviewed here was originally used by Shlesinger and Montroll to explain the stretched exponential dielectric relaxation observed in polymer systems and glasses, [**115**] based on original work by Montroll and Weiss which laid out the mathematics of the CTRW theory in 1965. [**116**] They considered a system with electric dipoles locked at fixed positions in the presence of mobile defects randomly diffusing in the lattice. When an electrical field is applied, the dipoles experience a torque to align in the direction of the externally applied field. But the dipole can only rotate to minimize its energy when the otherwise locked dipole is visited by a mobile defect for the first time. Thus the relaxation process is limited by defect diffusion, which can be modeled as a random walk in a lattice of allowed sites. For simplicity, a periodic

lattice is assumed with each step having equal probability to "walk" in any direction to a nearest neighboring site, as shown in Fig. 5.7(a).

Under the conditions of a standard "random walk," each step would take place at an equal time interval τ. However, the "continuous time" aspect of the walk arises if the time interval between steps itself follows a distribution function. Then remarkably different diffusion kinetics can arise depending on the distribution of waiting times t on each site before the defect steps in a random direction to a neighboring site. The waiting time distribution $\psi(t)$ is defined as the probability $\psi(t)dt$ that the wait time on a given site will be between t and $t + dt$, and is assumed to be a continuous distribution.

When the functional form of $\psi(t)$ is known, the relaxation transient $N(t)$ of polarized dipole density can be calculated with the CTRW model. For a $\psi(t)$ distribution with a finite average waiting time $\langle t\rangle = \int_0^\infty t\psi\left(t\right)dt/\int_0^\infty \psi\left(t\right)dt$, such as the exponential distribution $\psi\left(t\right) = \lambda\exp\left(-\lambda t\right)$, where $\langle t\rangle = 1/\lambda$, Bordewijk showed that the relaxation with time will follow a simple exponential decay when the defects are allowed to diffuse in 3 dimensions. [**119**]

$$N(t) = N(0)\exp(-ct), \text{ when } \langle t\rangle \text{ exists.} \tag{5.8}$$

Shlesinger and Montroll later considered the case of a waiting time distribution with an inverse power-law tail as Eq. (5.9).

$$\psi\left(t\right) \sim t^{-1-\alpha} \quad (0 < \alpha < 1) \tag{5.9}$$

For such a $\psi\left(t\right)$ distribution, the average waiting time $\langle t\rangle$ is undefined and approaches infinity. The resulting relaxation transient $N(t)$ has the form of a stretched exponential

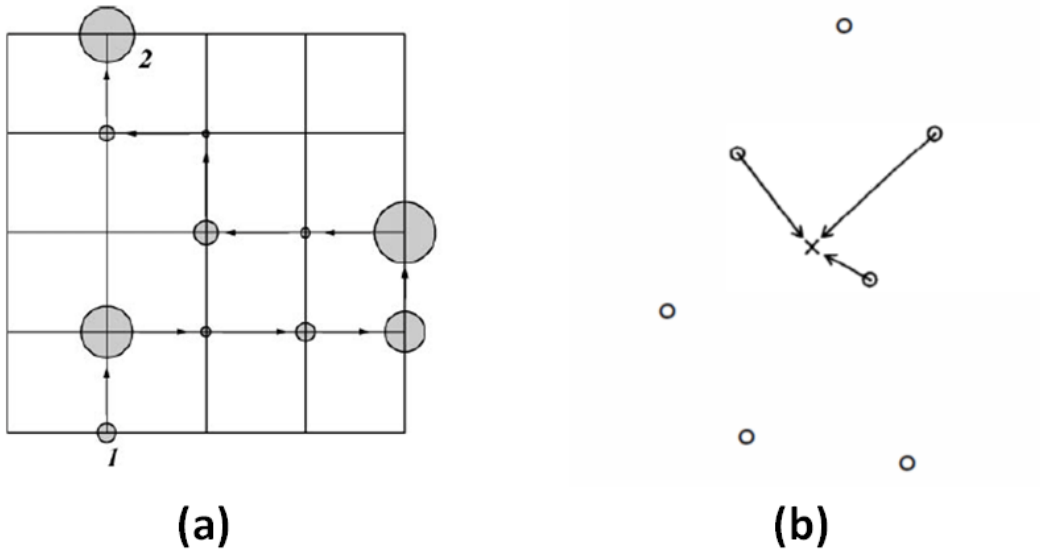

Figure 5.7. Schematics of the continuous-time random walk process. (a) Illustration of the random walk path of a mobile defect moving from position 1 to position 2 on a two-dimensional lattice from the work of Metzler. [**117**] The defect has equal probability to "walk" to a nearest neighboring site in each step. The circle diameters at each visited site symbolizes the waiting time t that the defect stays in the site before making the next step. (b) Illustration of a frozen dipole waiting to be relaxed by mobile defects from the work of Shlesinger. [**118**] The X in the center represents the dipole. The circle represent neighboring defects. The relaxation happens when any one of the defects visits the dipole for the first time.

function, with stretching exponent $\beta = \alpha$ for 3D diffusion. [**115**]

$$N(t) = N(0)\exp(-ct^{\alpha}) \tag{5.10}$$

As pointed out by Shlesinger in a subsequent review article, [**118**] when $\psi(t)$ has an infinite expected value for the wait time between steps $\langle t \rangle$, the asymptotic form of the relaxation transient will always be a stretched exponential. This may explain why stretched exponential responses are observed universally in so many different systems.

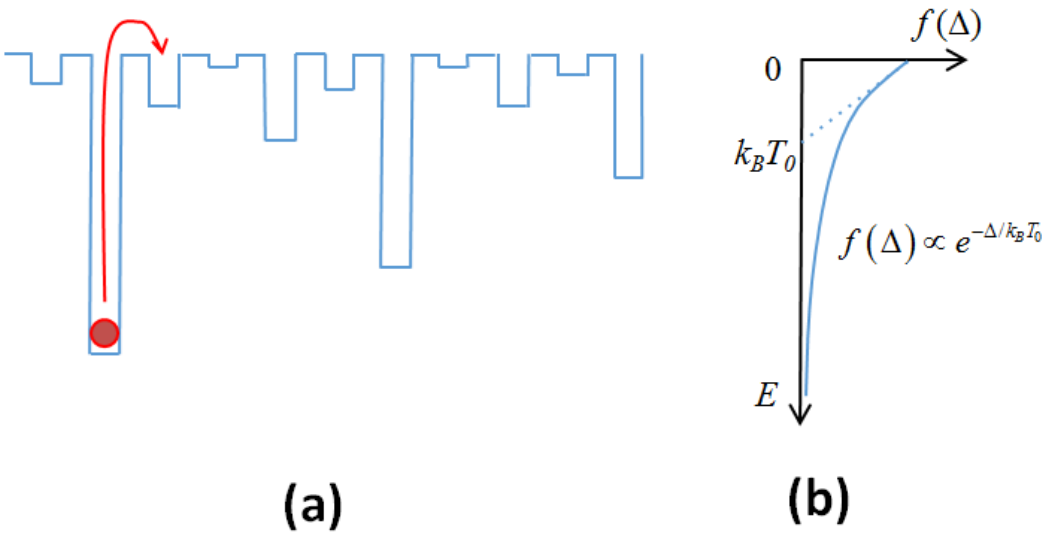

Figure 5.8. (a) Schematic illustrations of a defect diffusing through a 1-D lattice with distributed activation energies, where a deeply bound activation energy well Δ corresponds to a longer expected waiting time t at the site, and vise-versa. (b) An exponential tail distribution $f(\Delta) \propto \exp(-\Delta/k_B T_0)$ for the activation energies Δ. The characteristic energy scale (average energetic distribution width) for the exponential tail is $k_B T_0$. Such an exponential activation energy distribution $f(\Delta)$ will result in a power-law waiting time distribution $\psi(t) \sim t^{-1-\frac{T}{T_0}}$ provided that $T < T_0$.

The power-law waiting time distribution in Eq. (5.9) will arise in disordered media whenever there is activated behavior from an exponential tail of trap states. We follow the derivation below of Bendler and Shlesinger. [**120**] Diffusion through distributed activation energies is illustrated in Fig. 5.8. Assume the diffusion of a defect to the neighboring site is a thermally activated jump over a given activation energy barrier Δ with attempt-to-escape frequency ν as shown with the red arrow in Fig. 5.8(a), and assume the jumping is a Poisson process. Then the expected waiting time distribution to exit this particular

trap before taking the next step in the random walk is

$$\psi(t) = \lambda \exp(-\lambda t), \text{ where } \lambda = \nu \exp(-\Delta/k_B T), \tag{5.11}$$

where λ is the characteristic Poisson rate for escaping that defect. Because the next trap will have a different binding energy, one must consider the likelihood of the wait time for the next step from the distribution of barrier heights $f(\Delta)$. The ensemble average of traps will result in the following wait time distribution, whereby Eq. (5.11) is replaced by

$$\psi(t) = \int_0^\infty \lambda \mathrm{e}^{-\lambda t} \rho(\lambda) d\lambda. \tag{5.12}$$

Here the probability density of Poissonian rates is $\rho(\lambda) = f(\Delta) \left| \frac{d\Delta}{d\lambda} \right|$, derived following the chain rule. When the activation energies themselves have an exponential distribution

$$f(\Delta) \propto \exp(-\Delta/k_B T_0) \tag{5.13}$$

with average energetic width $k_B T_0$, the waiting time distribution determined from Eqs. (5.11) and (5.12) and shows the anticipated inverse power-law form:

$$\psi(t) \sim t^{-1-\frac{T}{T_0}} \text{ as } t \to \infty. \tag{5.14}$$

Note that if $T \geq T_0$, the average waiting time $\langle t \rangle$ has a finite value, and a simple exponential decay with characteristic time constant $\tau = \langle t \rangle$ will result. If, on the other hand, $T < T_0$, the average waiting time $\langle t \rangle$ is infinity, leading to a stretched exponential decay with stretching exponent $\beta = T/T_0$. [**115**, **118**] The exponentially distributed activation energy tail of Eq.(5.13) is expected to occur below the conduction band mobility edge for

many disordered systems and has been observed in many amorphous materials. [**12**, **121**] Therefore, it becomes clear why the stretched exponential behavior is so universally observed in amorphous media.

Though the original CTRW model was developed by Shlesinger and Montroll in the context of dielectric relaxation, the CTRW model can be adapted to other general relaxation processes in amorphous systems. To this end, Table 5.1 is introduced which shows the essence of the CTRW model along with various physical realizations thereof that demonstrate stretched-exponential behavior. In order to be mapped to the CTRW model, the system should have non-equilibrium metastable sites, randomly diffusing mobile "walkers" in the lattice, and a relaxation process triggered when a metastable site is visited by a mobile walker for the first time. These essential elements for a generic CTRW model are listed in the first column of Table 5.1. The second column summarizes the previously introduced model for dielectric relaxation whereby the frozen dipoles represent the metastable sites; the mobile defects represent the walkers; and the reorientation of the frozen dipole when it is visited by the defect for the first time represents the relaxation process for the model. Thus, according to the CTRW model, the dipole relaxation kinetics is entirely determined by the diffusion of the defects with characteristic energy scale $kT_0 = kT/\beta$. The stretched exponential relaxation observed in amorphous or glassy dielectrics can be explained by defects diffusing among trap states with an exponential-tail distribution in energy.

Table 5.1. Comparison of different stretched-exponential systems with the generic CTRW model.

Generic CTRW model	Dielectric relaxation	a-Si:H relaxation	a-IGZO relaxation
$\phi(t) = \phi \exp[(t/\tau)^{\beta}]$	$\epsilon(t) = \Delta\epsilon \exp[(t/\tau)^{\beta}] + \epsilon_{\infty}$	$n_{BT}(t) = \Delta n_{BT} \exp[(t/\tau)^{\beta}] + n_{BT,\infty}$	$\sigma(t) = \Delta\sigma \exp[(t/\tau)^{\beta}] + \sigma_{\infty}$
Metastable sites	Frozen dipoles	Shallow occupied band-tail states	Oxygen-coordinated In-In bond
Mobile walkers	Mobile defects	Hydrogen atoms	Migrating M-M metallic bonds where M = (In, Ga, Zn); also known as "oxygen vacancies"
Relaxed sites	Relaxed dipoles	Dangling bonds created through bond switching	In-In deep bonds
Montroll & Weiss [116] and Schlesinger & Montroll [115]	Kohlrausch [**105**] and Williams & Watts [**107**]	Kakalios *et al.* [**89**]	This work

5.5. Microscopic CTRW mechanism for a-Si:H band tail electron relaxation: Hydrogen diffusion

Kakalios *et al.* adapted the CTRW model to explain experimental results in hydrogenated amorphous silicon (a-Si:H), whereby a stretched exponential decay was observed for the density of shallow occupied band-tail states n_{BT}. [**89**] In their experiments, the a-Si:H samples were annealed at 210 ℃ for 10 minutes and rapidly cooled to freeze the electrons in the shallow occupied states. Each metastable state effectively was matched with one electron that was donated to the concentration of shallow occupied states. As the metastable states relaxed to form deep traps N_{DT} for the electrons, the concentration of electrons in the shallow band-tail states would decrease, $\Delta N_{DT} = -\Delta n_{BT}$. As shown in Fig. 5.9(a), the relaxation transients of n_{BT} at temperatures ranging from 22 ℃ to 125 ℃ all showed stretched exponential behavior. And the fitted β values increased linearly with increasing temperature T, as shown by the closed circles in Fig. 5.9(b), where $T_0 \approx 600$ K. This linear temperature dependence of β fits Bendler and Shlesinger's prediction for stretched exponential decay arising from exponentially distributed activation energies since $T < T_0$.

Kakalios *et al.* further identified that the mobile walkers in the CTRW model for a-Si:H were the hydrogen atoms, themselves. They measured the time-evolution of the hydrogen diffusion coefficient $D_H(t)$, and observed a power-law decrease of the diffusion coefficients over time as $D_H(t) \propto t^{-\alpha}$. By defining a decay rate $\nu(t) = -\frac{d\Delta n_{BT}/dt}{\Delta n_{BT}}$ for the relaxation of the overall change in the number of band-tail states Δn_{BT}, a stretched exponential decay $\Delta n_{BT} \propto \exp[-(t/\tau)^{\beta}]$ yields $\nu(t) \propto t^{\beta-1}$. If the power-law decay of $\nu(t)$ has the same underlying cause as the power-law decay of the hydrogen diffusion coefficient

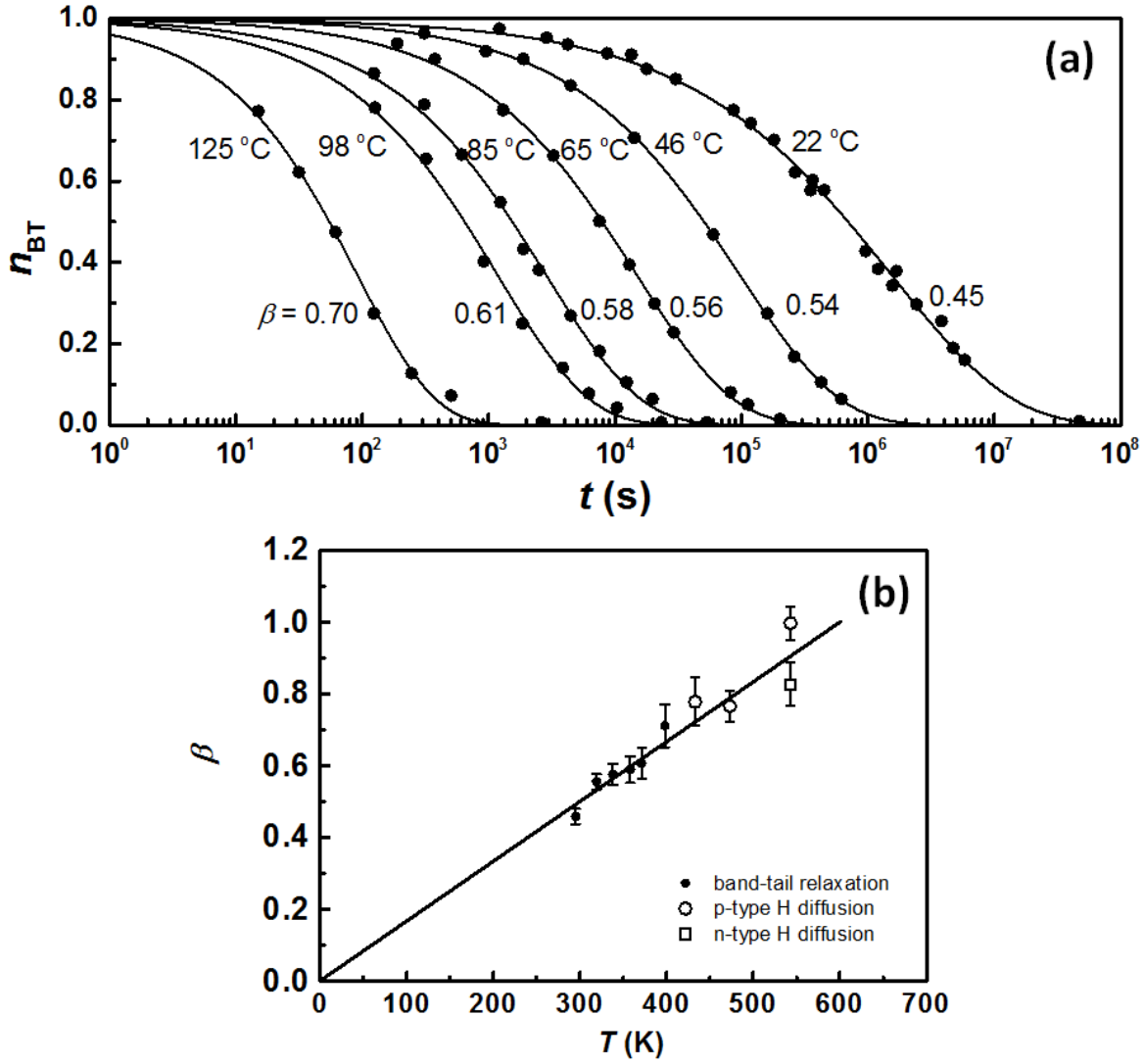

Figure 5.9. Illustration of stretched exponential relaxations and temperature dependence in the a-Si:H system as measured by Kakalios *et al.* [**89**] (a) Time dependence for the shallow occupied band-tail state density n_{BT} plotted versus log-time. The solid circles are the experimental results, and the solid lines are the stretched exponential fitting results determining the β values at each temperature. (b) Temperature dependence of exponent β. The solid circles are obtained from the stretched exponential fitting in (a) to the n_{BT} relaxation. The open circles are obtained from the power-law fitting to hydrogen diffusion coefficient transient (not shown) in p-type samples, and the open square from the n-type samples. The β values obtained from different experiments and different samples follow the same linear temperature dependence, as indicated by the line.

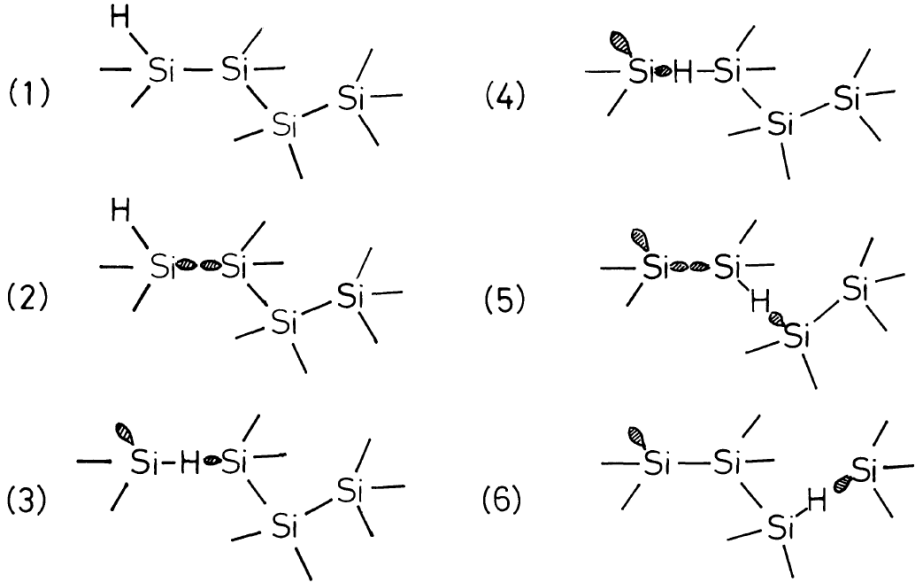

Figure 5.10. Successive steps illustrating a microscopic model for dangling bonds created by hydrogen diffusion in a-Si:H from the work of Morigaki. [**122**] At step (1) there are no dangling bonds. A spontaneous thermally generated anti-bonding of a pair of neighboring Si atoms is shown in step (2). Steps (3) to (5) show the Si-H bond switching associated with H diffusion. In the final step (6), two separate dangling bonds are created.

$D_H(t)$, they should have the same exponent. The plot of the power-law exponents β and $1-\alpha$ as the filled circles and open symbols, respectively, shows the expected relation that $\beta = 1-\alpha$ in Fig. 5.9(b). Therefore they suggested that the stretched exponential conductivity relaxation arises from the diffusion of the hydrogen dopants.

A possible microscopic model for the hydrogen-assisted relaxation process in the a-Si:H system was later proposed by Morigaki. [**122**] According to this model, hydrogen atoms passivating a dangling bond as shown in Fig. 5.10 step (1) can weaken the Si-Si bonds in the amorphous structure, allowing two dangling bonds to be created, as step (2) in Fig. 5.10. When a hydrogen dopant diffuses to the bond site, the Si-H bond switches positions with dangling bonds through steps (3-5) in Fig. 5.10. Through bond

switching, the two dangling bonds are separated and can no longer recombine with each other spontaneously. This process increases the density of deep dangling bonds, trapping electrons and thereby decreasing the density of shallow occupied band-tails states.

Combining the work of Kakalios *et al.* with the molecular model of Morigaki, each ingredient of the stretched exponential relaxation in a-Si:H can be mapped to the CTRW model, as shown in the third column of Table 5.1. What remains is to identify a mapping between the stretched exponential relaxation in a-IGZO to the CTRW model, as discussed in the next section.

5.6. Candidate mechanisms for photoconductivity in a-IGZO

In the last two sections, the dynamics of the transient photoresponse was discussed with the distributed activation energy model and the CTRW model. The CTRW model fits more naturally with the observed stretched exponential transients, but the species playing the role of the metastable sites and the mobile walkers have not been identified. Understanding the possible microscopic mechanisms at the molecular level will help to identify the ones that are compatible with CTRW model. In this section, I will briefly review previously proposed candidate microscopic mechanisms for photoresponse in the a-IGZO system, and discuss how they are consistent or inconsistent with our experimental observations. Then based on the molecular dynamics simulation results, a possible mapping of the a-IGZO system to the continuous-time random walk model will be proposed.

Based on the location where illumination-induced effects happen in the thin film structure, all microscopic mechanisms for electron doping can be classified as either interfacial effects or bulk effects. For samples directly exposed to the ambient without encapsulation

or passivation, the IGZO/ambient gas interface plays an important role in carrier density instability. The oxygen species can be adsorbed to and desorbed from the a-IGZO surface. The ambient oxygen, adsorbed oxygen, and free electrons maintain a dynamic equilibrium through Eq. (5.15), where the adsorbed oxygen species may exist in various forms such as O^{2-}, O^{-}, or O_2^{-}. [**30**]

$$O_2(\text{gas}) + e^- \leftrightarrows O_2^-(\text{solid}) \tag{5.15}$$

Those weakly adsorbed oxygen species can be desorbed during illumination, releasing free electrons to the bulk material. During dark relaxation, the adsorbed oxygen species is proposed to act as an electron trap at the IGZO/ambient interface, causing a slow conductivity decay. [**123**] Besides oxygen, moisture in the air was also found to accelerate the photo-induced instability response. [**124**]

In our measurements of transient photoconductivity in a-IGZO thin films, encapsulation was used on some samples to isolate them from ambient oxygen or moisture. The encapsulated samples showed simple monotonic transients with decreasing relaxation rates, while the uncapped samples showed step-like responses after sufficiently long dark relaxation, as shown in Fig. 5.11. The step-like behavior observed here might be caused by a structural change such as spontaneous crystallization of domains induced by oxygen and moisture accumulated at the IGZO/ambient interface. Regardless of the cause, it is clear that encapsulation or passivation in necessary for all a-IGZO based devices. However, ambient gas effects alone cannot account for the widely observed photoresponse in a-IGZO, as the capped samples also showed significant photoresponse in Fig. 5.11. Also, Adler *et al.* observed that the conductivity transient in a-IGZO thin films that was caused by an

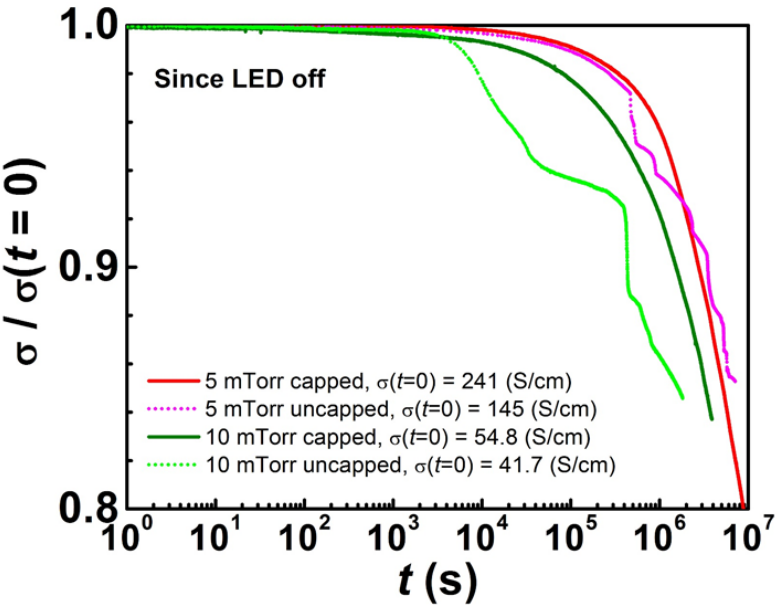

Figure 5.11. Transient photoconductivity after steady UV illumination in capped (dark red, dark green) and uncapped (light red, light green) a-IGZO samples. Results for 50 nm PLD-grown samples deposited at 5 mTorr and 10 mTorr are shown. Both capped samples showed the conductivity decreasing monotonically with decreasing rate, while both uncapped samples showed irregular step-like conductivity change at long time scales.

ambient oxygen pressure change at 200 ℃ had two discrete time constants, inferring both surface and bulk reactions with oxygen affecting the thin film conductivity. [**19**]

Another important interface to consider is the one between the a-IGZO thin film and the underlying dielectric layer. For TFT applications, the a-IGZO channel layer is typically deposited on top of a dielectric gate insulator layer, and then covered by the top passivation layer, forming two IGZO/dielectric interfaces. Ji *et al.* showed that the a-IGZO TFTs using SiO_2 as gate insulator had improved stability under illumination compared with those using SiN_x. [**33**] This was explained by the band alignment between IGZO and the dielectric material. As shown in Fig. 5.12, since SiN_x has bandgap significantly lower

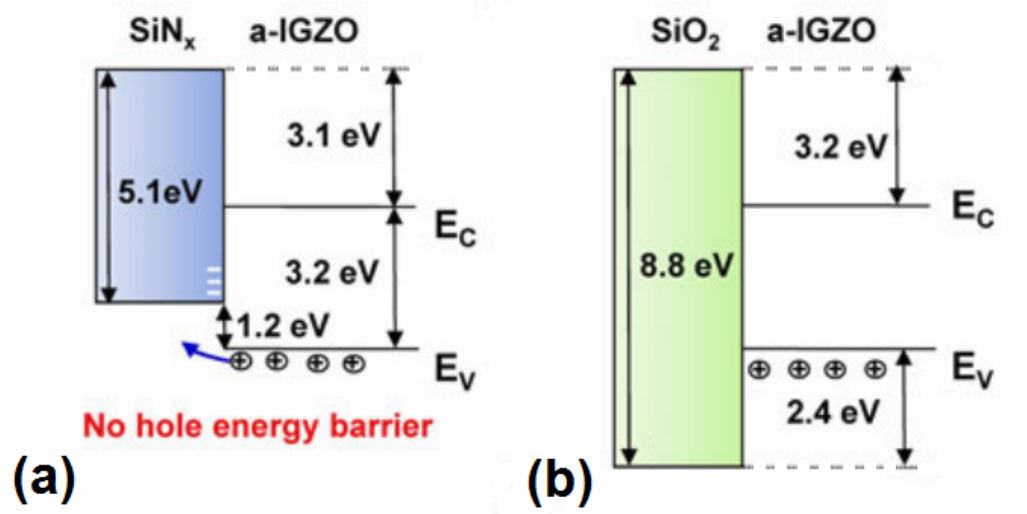

Figure 5.12. Schematic band diagrams showing the likelihood of hole trapping at the IGZO/dielectric interfaces adapted from the work of Jeong. [**24**] (a) Band diagram of the IGZO/SiN_x interface. The valence band maximum of the SiN_x layer is higher than that of the a-IGZO layer, so holes can be trapped at the IGZO/SiN_x interface, causing device instability. (b) Band diagram of the IGZO/SiO_2 interface. The valence band maximum of the SiO_2 layer is much lower than that of the a-IGZO layer. The large hole energy barrier prevents holes from being trapped at the interface.

than SiO_2, the IGZO/SiN_x interface has no hole barrier, while the IGZO/SiO_2 interface has a significant one $\sim$ 2.4 eV. [**125**] Therefore, holes generated during illumination were more easily trapped by the defects at the IGZO/SiN_x interface, causing increased instability for the devices that used a SiN_x gate dielectric compared to those using SiO_2. Other dielectric materials, such as Y_2O_3, [**35**] Al_2O_3, [**56**], and HfO_2 [**126**] *etc.*, have been used to improve illumination stability for a-IGZO TFTs. In all our experiments, SiO_2 (fused quartz) or SiO_2 coated Si wafers were used as substrates. Because the energy difference between the conduction band minimum of a-IGZO and the valence band maximum of SiO_2 is much larger than the photon energy for illumination (3.22 eV for the 385 nm UV LEDs), hole traps at the IGZO/SiO_2 interface are not likely to be the main reason for the

large illumination-induced responses. The instability in the capped samples can instead be attributed principally to the bulk effects for a-IGZO.

Previous studies of the bulk effect focused on the ionization of oxygen species. If one were to assume the distributed activation energy model, transient photoresponses in a-IGZO would typically have activation energies around 1 eV. Thus many reports have attempted to identify the chemical reaction that releases or consumes free electrons while having an activation energy $\sim$ 1 eV. Nahm *et al.* [**54**] showed that the ionization of the stable oxide state O^{2-} to the metastable peroxide state O_2^{2-} would release free electrons through process

$$O^{2-} + O^{2-} + 2h^+ + 2e^- \rightarrow O_2^{2-} + 2e^-, \tag{5.16}$$

and the metastable O_2^{2-} would relax in the dark through

$$O_2^{2-} + 2e^- \rightarrow O^{2-} + O^{2-}. \tag{5.17}$$

Using theoretical simulation with the hybrid density functional theory, they showed that the relaxation process had an activation energy of 0.97 eV, consistent to the expected value of $\sim$ 1 eV. Instead of bulk oxygen, Robertson *et al.* considered the relaxation of photo-ionized interstitial oxygen I_O^{2-} to the charge neutral state I_O, and arrived at similar activation energy $\sim$ 0.9 eV. [**32**] As suggested by Migliorato *et al.*, the $\sim$ 1 eV activation energy may also be explained by the ionization of the oxygen vacancies $[V_O]$, which forms shallow singly ionized $[V_O^+]$ and deep doubly ionized $[V_O^{2+}]$ under illumination. [**26**] However, all the above photo-ionization models only considered the activation energy height. For the widely observed stretched exponential responses, the asymmetric activation energy

distribution corresponding to the distributed activation energy model has not been either observed or justified. Instead, illumination-induced response may be better explained by other microscopic mechanisms which might prove compatible with the continuous-time random walk model.

5.7. Microscopic CTRW mechanism for a-IGZO photoconductivity relaxation: Introducing the metallic bond diffusion model

In analogy to the hydrogen diffusion model in the a-Si:H system, here we propose a possible mapping of the a-IGZO system to the CTRW system, which we call the "metallic bond-diffusion model".

Using molecular dynamics simulation combined with density function theory calculations, our collaborator Medvedeva identified that there are under-coordinated metallic bonds in the amorphous structure. [**127**] Upon examination of Fig. 5.13 panels (a) and (b), it is clear that these M-M bonds between cations M = { In, Ga, Zn } have the following signatures: 1) there is an enhanced electron density between the two bonded metal atoms; 2) the M-M bond has a shorter bond length than the typical intercation distance when no bond is present; 3) the binding energy of the M-M bond tends to be in the 0.8 eV-1.2 eV range. The In-In bond in particular seems to be the deepest binding energy ∼1.2 eV) compared to the In-Zn with ∼0.8 eV. It also has a higher localized e^- density with around 1.06 electrons between the In-In bonded atoms compared with 0.66 electrons in the In-Zn bond. Ga-Zn, Ga-Ga, and Zn-Zn under-coordinated metallic bonds would be expected to have even shallower binding energies, thought there is not yet simulation data to support this conjecture.

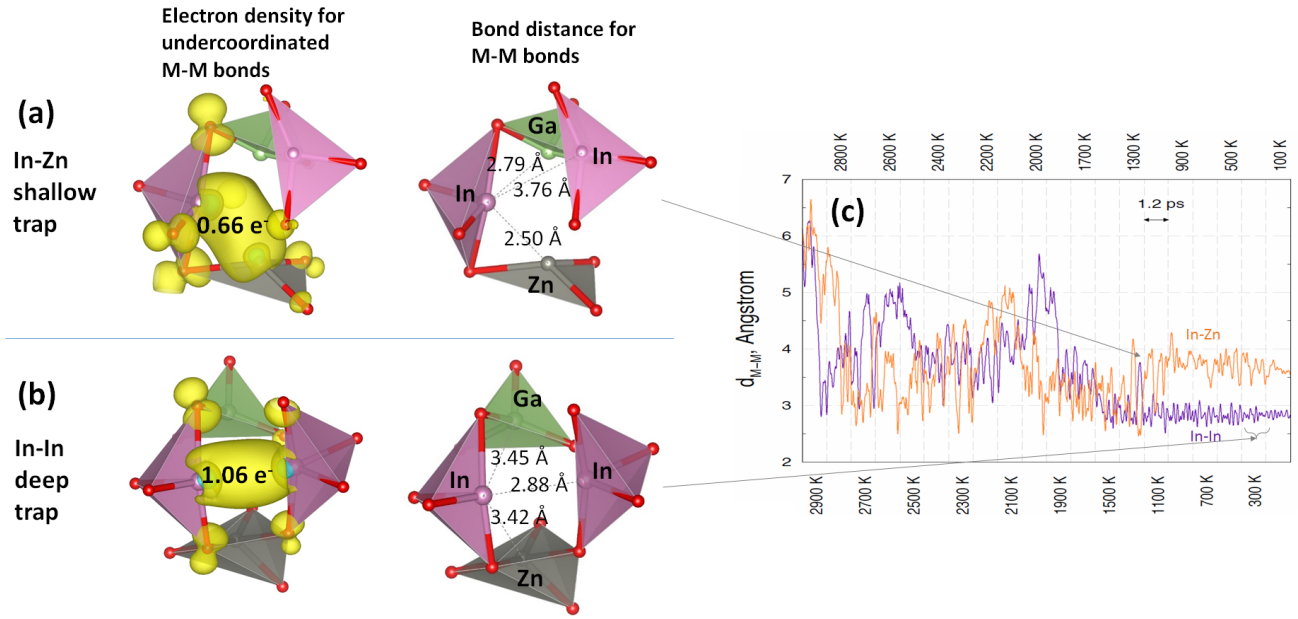

Figure 5.13. Molecular dynamics simulation results from Medvedeva showing the metastable under-coordinated metallic bonds M-M where M = {In,Ga,Zn}. [**127**] Such bonds fit the description of an "oxygen vacancies" since the local coordination number with oxygen atoms is reduced. (a) Local structure surrounding an under-coordinated In-Zn metallic bond with In atoms pink, Zn atoms gray, Ga atoms green, and O atoms red. The areas with yellow color indicate high electron probability densities. (b) The same region of the sample but now the local structure reveals an undercoordinated In-In metallic bond. Note that when transitioning from the In-Zn bond to the In-In bond, there is also a change in oxygen positions. The binding energy of the In-Zn bond is shallower ($\sim$ 0.8 eV; lower local electron density 0.66 e$^-$) than the binding energy of the In-In bond ($\sim$ 1.2 eV; higher local electron density 1.06 e$^-$). (c) The metal-metal distance d_{M-M} between neighboring cations, showing the In-In pair (purple trace) and a neighboring In-Zn pair (orange trace) during the molecular dynamics quench from high temperature (left) to low (right). At high temperatures, higher-energy configurations of the under-coordinated cations such as the In-Zn metallic bond can be identified, such as the In-Zn bond that was observed at 1300 K when the In-Zn bond distance showed a dip and the In-In bond distance simultaneously showed a peak.

Panel (c) shows the molecular dynamics simulation of the quench process which achieved this amorphous state calculation. During the simulation, a crystalline structure is used as the initial state. To remove the memory of the atomic arrangement, the initial structure is melted computationally at 3000 K. Next, the melt is cooled to 1700 K at the rate of 100 K/1.2 ps, and then rapidly quenched to 100K using a faster quench rate of 200 K/1.2 ps. [**128**] The final structure is equilibrated at 300 K. Under-coordinated metallic bonds can be identified in the final amorphous structure as seen in panels (a) and (b) of Fig. 5.13. In particular, the simulations at high temperature show a greater fluctuation of the bond length and are therefore sampling higher energy configurations. One can therefore use the high temperature simulations to identify various alternate configurations of the local atoms which have ever higher energies. Although these high energy states do not arise at room temperature during the $\sim$ 50 ps simulation, they most certainly could occur at room temperature given enough time. Thus one can think of the under-coordinated M-M metallic bond as a defect that can hop through the amorphous matrix from site-to-sit. In terms that the a-IGZO community would be more familiar with, this work identifies the molecular nature of the "oxygen vacancy" that can diffuse through the structure.

The migration of the M-M bond from the In-Zn site to the In-In bond site can be considered within the context of the CTRW model as a mobile defect. The stretched exponential transients in a-IGZO could then be explained as follows. During illumination, non-equilibrium states such as the under-coordinated In-Zn bonds are formed and their weaker binding energy allows electrons to be donated to the large density of states at higher energies above the mobility gap. Upon stop of illumination, those bonds will slowly

relax to the stable In-In bonds, trapping more electrons in these deep In-In bonds, and thereby decreasing the electron concentration and reducing the conductivity. To complete the final column of Table 5.1, the non-equilibrium In-Zn bonds existing with oxygen-coordinated In-In bonds can be mapped to the metastable states, the M-M migrating bonds ("oxygen vacancies") can be mapped to the mobile "walkers", and the stable In-In bonds can be mapped to the relaxed sites.

Following this mapping to the CTRW model, the long-standing problem of persistent photoresponse in a-IGZO may be eventually solved. Firstly, the temperature dependence of the stretching exponent β describing the photoconductivity transients should be measured. If β is proportional to temperature T, then the stretched exponential behavior can be truly associated with an exponential tail of activation energies, as in the a-Si:H system. If there is no temperature dependence, then the non-exponential transient may still give rise to a CTRW mechanism, but through a tunneling process. [**89**] In the case of $\beta \propto T$, the exponential tail of activation energies would characterize the average distribution width $k_B T_0$. The empirical treatments previously reported to reduce photoresponse, such as annealing, can now be studied with respect to the change of activation energy distribution by measuring the stretching exponent β before and after the treatment. If annealing, or any other treatment, can make T_0 small enough that $T > T_0$ at room temperature, then the transient photoresponse reduces to a simple exponential decay. The photoresponse will no longer be "persistent" and would instead decay in a well-behaved manner with a characteristic decay time $\langle t \rangle$. All the large time constant components in the long term response will be eliminated, improving the long-term stability of a-IGZO based devices.

References

[1] Toshio Kamiya, Kenji Nomura, and Hideo Hosono. Present status of amorphous InGaZnO thin-film transistors. *Science and Technology of Advanced Materials*, 11(4):044305, aug 2010.

[2] Hideo Hosono, Masahiro Yasukawa, and Hiroshi Kawazoe. Novel oxide amorphous semiconductors: transparent conducting amorphous oxides. *Journal of Non-Crystalline Solids*, 203:334–344, aug 1996.

[3] Hideo Hosono, Naoto Kikuchi, Naoyuki Ueda, and Hiroshi Kawazoe. Working hypothesis to explore novel wide band gap electrically conducting amorphous oxides and examples. *Journal of Non-Crystalline Solids*, 198-200(PART 1):165–169, may 1996.

[4] Kenji Nomura, Hiromichi Ohta, Akihiro Takagi, Toshio Kamiya, Masahiro Hirano, and Hideo Hosono. Room-temperature fabrication of transparent flexible thin-film transistors using amorphous oxide semiconductors. *Nature*, 432(7016):488–492, nov 2004.

[5] M. Orita, H. Ohta, M. Hirano, S. Narushima, and H. Hosono. Amorphous transparent conductive oxide InGaO 3 (ZnO) m (m 4): a Zn4s conductor. *Philosophical Magazine Part B*, 81(5):501–515, may 2001.

[6] Kenji Nomura, Toshio Kamiya, Hiromichi Ohta, Kazushige Ueda, Masahiro Hirano, and Hideo Hosono. Carrier transport in transparent oxide semiconductor with intrinsic structural randomness probed using single-crystalline InGaO[sub 3](ZnO)[sub 5] films. *Applied Physics Letters*, 85(11):1993, 2004.

[7] E Fortunato, P Barquinha, and R Martins. Oxide semiconductor thin-film transistors: a review of recent advances. *Advanced materials (Deerfield Beach, Fla.)*, 24(22):2945–86, jun 2012.

[8] Joon Seok Park, Wan-Joo Maeng, Hyun-Suk Kim, and Jin-Seong Park. Review of recent developments in amorphous oxide semiconductor thin-film transistor devices. *Thin Solid Films*, 520(6):1679–1693, jan 2012.

[9] Thomas Riedl, Patrick Gorrn, and Wolfgang Kowalsky. Transparent Electronics for See-Through AMOLED Displays. *Journal of Display Technology*, 5(12):501–508, dec 2009.

[10] Toshio Kamiya and Hideo Hosono. Material characteristics and applications of transparent amorphous oxide semiconductors. *NPG Asia Materials*, 2(1):15–22, jan 2010.

[11] Jae Kyeong Jeong, Jong Han Jeong, Hui Won Yang, Tae Kyung Ahn, Minkyu Kim, Kwang Suk Kim, Bon Seog Gu, Hyun-joong Chung, Jin-Seong Park, Yeon-Gon Mo, Hye Dong Kim, and Ho Kyoon Chung. 12.1-in. WXGA AMOLED display driven by InGaZnO thin-film transistors. *Journal of the Society for Information Display*, 17(2):95, 2009.

[12] J Singh and K Shimakawa. *Advances in amorphous semiconductors*. 2003.

[13] Kenji Nomura, Toshio Kamiya, Hiroshi Yanagi, Eiji Ikenaga, Ke Yang, Keisuke Kobayashi, Masahiro Hirano, and Hideo Hosono. Subgap states in transparent amorphous oxide semiconductor, InGaZnO, observed by bulk sensitive x-ray photoelectron spectroscopy. *Applied Physics Letters*, 92(20):202117, 2008.

[14] T. Kamiya, K. Nomura, and H. Hosono. Origins of High Mobility and Low Operation Voltage of Amorphous Oxide TFTs: Electronic Structure, Electron Transport, Defects and Doping. *Journal of Display Technology*, 5(7):273–288, jul 2009.

[15] Mutsumi Kimura, Takashi Nakanishi, Kenji Nomura, Toshio Kamiya, and Hideo Hosono. Trap densities in amorphous-InGaZnO[sub 4] thin-film transistors. *Applied Physics Letters*, 92(13):133512, 2008.

[16] Franz Urbach. The Long-Wavelength Edge of Photographic Sensitivity and of the Electronic Absorption of Solids. *Physical Review*, 92(5):1324–1324, dec 1953.

[17] Toshio Kamiya, Kenji Nomura, and Hideo Hosono. Electronic structure of the amorphous oxide semiconductor a-InGaZnO4- x : Tauc-Lorentz optical model and origins of subgap states. *Physica Status Solidi (a)*, 206(5):860–867, may 2009.

[18] P. Stallinga and H.L. Gomes. Thin-film field-effect transistors: The effects of traps on the bias and temperature dependence of field-effect mobility, including the MeyerNeldel rule. *Organic Electronics*, 7(6):592–599, dec 2006.

[19] Alexander U. Adler, Ted C. Yeh, D. Bruce Buchholz, Robert P. H. Chang, and Thomas O. Mason. Quasi-reversible point defect relaxation in amorphous In-Ga-Zn-O thin films by in situ electrical measurements. *Applied Physics Letters*, 102(12):122103, 2013.

[20] Dong Hee Lee, Ken-ichi Kawamura, Kenji Nomura, Toshio Kamiya, and Hideo Hosono. Large Photoresponse in Amorphous InGaZnO and Origin of Reversible and Slow Decay. *Electrochemical and Solid-State Letters*, 13(9):H324, 2010.

[21] Hideo Hosono. Ionic amorphous oxide semiconductors: Material design, carrier transport, and device application. *Journal of Non-Crystalline Solids*, 352(9-20):851–858, jun 2006.

[22] Hideo Hosono. Current status and future challenge of oxide semiconductors. *Active-Matrix Flatpanel Displays and Devices (AM-FPD), 2012 19th International Workshop on*, pages 1–4, 2012.

[23] T.-Y. Hsieh, T.-C. Chang, T.-C. Chen, and M.-Y. Tsai. Review of Present Reliability Challenges in Amorphous In-Ga-Zn-O Thin Film Transistors. *ECS Journal of Solid State Science and Technology*, 3(9):Q3058–Q3070, aug 2014.

[24] Jae Kyeong Jeong. Photo-bias instability of metal oxide thin film transistors for advanced active matrix displays. *Journal of Materials Research*, 28(16):2071–2084, aug 2013.

[25] Chang-Hoon Han, Sang-Sub Kim, Kwang-Ryul Kim, Do-Hyun Baek, Sang-Soo Kim, and Byoung-Deog Choi. Effects of electron trapping and interface state generation on bias stress induced in indiumgalliumzinc oxide thin-film transistors. *Japanese Journal of Applied Physics*, 53(8S3):08NG04, aug 2014.

[26] Piero Migliorato, Md Delwar Hossain Chowdhury, Jae Gwang Um, Manju Seok, and Jin Jang. Light/negative bias stress instabilities in indium gallium zinc oxide thin film transistors explained by creation of a double donor. *Applied Physics Letters*, 101(12):123502, 2012.

[27] Hideya Kumomi. Advances in Oxide Semiconductors for Transistors. *Hybrid Electronic & Photonic Materials and Phenomena, Gordon Research Conference*, 2016.

[28] David Redfield and Richard H. Bube. Reinterpretation of degradation kinetics of amorphous silicon. *Applied Physics Letters*, 54(11):1037, 1989.

[29] Y. Ueoka, Y. Ishikawa, J. P. Bermundo, H. Yamazaki, S. Urakawa, M. Fujii, M. Horita, and Y. Uraoka. Density of States in Amorphous In-Ga-Zn-O Thin-Film

Transistor under Negative Bias Illumination Stress. *ECS Journal of Solid State Science and Technology*, 3(9):Q3001–Q3004, apr 2014.

[30] Jae Kyeong Jeong, Hui Won Yang, Jong Han Jeong, Yeon-Gon Mo, and Hye Dong Kim. Origin of threshold voltage instability in indium-gallium-zinc oxide thin film transistors. *Applied Physics Letters*, 93(12):123508, 2008.

[31] Sang Yun Sung, Jun Hyuk Choi, Un Bin Han, Ki Chang Lee, Joon Hyung Lee, Jeong Joo Kim, Wantae Lim, S. J. Pearton, D. P. Norton, and Young Woo Heo. Effects of ambient atmosphere on the transfer characteristics and gate-bias stress stability of amorphous indium-gallium-zinc oxide thin-film transistors. *Applied Physics Letters*, 96(10), 2010.

[32] John Robertson and Yuzheng Guo. Light induced instability mechanism in amorphous InGaZn oxide semiconductors. *Applied Physics Letters*, 104(16):162102, apr 2014.

[33] Kwang Hwan Ji, Ji In Kim, Yeon Gon Mo, Jong Han Jeong, Shinhyuk Yang, Chi Sun Hwang, Sang Hee Ko Park, Myung Kwan Ryu, Sang Yoon Lee, and Jae Kyeong Jeong. Comparative study on light-induced bias stress instability of igzo transistors with SiNx and SiO2 gate dielectrics. *IEEE Electron Device Letters*, 31(12):1404–1406, 2010.

[34] Kyoung Seok Son, Joon Seok Park, Tae Sang Kim, Hyun Suk Kim, Seok Jun Seo, Sun Jae Kim, Jong Baek Seon, Kwang Hwan Ji, Jae Kyeong Jeong, Myung Kwan Ryu, and Sangyoon Lee. Improvement of photo-induced negative bias stability of oxide thin film transistors by reducing the density of sub-gap states related to oxygen vacancies. *Applied Physics Letters*, 102(12), 2013.

[35] Kenji Nomura, Toshio Kamiya, and Hideo Hosono. Highly stable amorphous In-Ga-Zn-O thin-film transistors produced by eliminating deep subgap defects. *Applied Physics Letters*, 99(5):10–13, 2011.

[36] Jeong Hwan Kim, Un Ki Kim, Yoon Jang Chung, and Cheol Seong Hwang. Improvement in the negative bias illumination temperature stress instability of In-Ga-Zn-O thin film transistors using an Al2O3 buffer layer. *Physica Status Solidi - Rapid Research Letters*, 5(5-6):178–180, 2011.

[37] Longyan Yuan, Guojia Fang, Xiao Zou, Huihui Huang, Hai Zou, Xiangyun Han, Yihua Gao, Sheng Xu, and Xingzhong Zhao. Optical and electrical characterization of α-InGaZnO thin film fabricated by pulsed laser deposition for thin film transistor applications. *Journal of Physics D: Applied Physics*, 42(21):215301, 2009.

[38] Q. Zhu, Q. Ma, D. B. Buchholz, R. P H Chang, M. J. Bedzyk, and T. O. Mason. Structural and physical properties of transparent conducting, amorphous Zn-doped SnO2 films. *Journal of Applied Physics*, 115(3):033512, jan 2014.

[39] T.C. Yeh, Q. Zhu, D.B. Buchholz, A.B. Martinson, R.P.H. Chang, and T.O. Mason. Amorphous transparent conducting oxides in context: Work function survey, trends, and facile modification. *Applied Surface Science*, 330:405–410, mar 2015.

[40] D Bruce Buchholz, Qing Ma, Diego Alducin, Arturo Ponce, Miguel Jose-Yacaman, Rabi Khanal, Julia E Medvedeva, and Robert P H Chang. The Structure and Properties of Amorphous Indium Oxide. *Chemistry of Materials*, 26(18):5401–5411, sep 2014.

[41] Hisato Yabuta, Masafumi Sano, Katsumi Abe, Toshiaki Aiba, Tohru Den, Hideya Kumomi, Kenji Nomura, Toshio Kamiya, and Hideo Hosono. High-mobility thin-film transistor with amorphous InGaZnO[sub 4] channel fabricated by room temperature rf-magnetron sputtering. *Applied Physics Letters*, 89(11):112123, 2006.

[42] Wantae Lim, SeonHoo Kim, Yu-Lin Wang, J. W. Lee, D. P. Norton, S. J. Pearton, F. Ren, and I. I. Kravchenko. High-Performance Indium Gallium Zinc Oxide Transparent Thin-Film Transistors Fabricated by Radio-Frequency Sputtering. *Journal of The Electrochemical Society*, 155(6):H383, 2008.

[43] Yeon-Keon Moon, Sih Lee, Do-Hyun Kim, Dong-Hoon Lee, Chang-Oh Jeong, and Jong-Wan Park. Application of DC Magnetron Sputtering to Deposition of InGaZnO Films for Thin Film Transistor Devices. *Japanese Journal of Applied Physics*, 48(3):031301, mar 2009.

[44] P.J J Kelly and R.D D Arnell. Magnetron sputtering: a review of recent developments and applications. *Vacuum*, 56(3):159–172, 2000.

[45] Kenji Nomura, Akihiro Takagi, Toshio Kamiya, Hiromichi Ohta, Masahiro Hirano, and Hideo Hosono. Amorphous Oxide Semiconductors for High-Performance Flexible Thin-Film Transistors. *Japanese Journal of Applied Physics*, 45(5B):4303–4308, may 2006.

[46] Ji-Hoon Shin. Effect of Oxygen on the Optical and the Electrical Properties of Amorphous InGaZnO Thin Films Prepared by RF Magnetron Sputtering. *Journal of the Korean Physical Society*, 53(4):2019–2023, 2008.

[47] Hyun Sung Kim, Paul D Byrne, Antonio Facchetti, and Tobin J. Marks. High Performance Solution-Processed Indium Oxide Thin-Film Transistors. *Journal of the American Chemical Society*, 130(38):12580–12581, 2008.

[48] Myung-Gil Kim, Mercouri G Kanatzidis, Antonio Facchetti, and Tobin J Marks. Low-temperature fabrication of high-performance metal oxide thin-film electronics via combustion processing. *Nature materials*, 10(5):382–8, may 2011.

[49] Xinge Yu, Jeremy Smith, Nanjia Zhou, Li Zeng, Peijun Guo, Yu Xia, Ana Alvarez, Stefano Aghion, Hui Lin, Junsheng Yu, Robert P H Chang, Michael J Bedzyk, Rafael Ferragut, Tobin J Marks, and Antonio Facchetti. Spray-combustion synthesis: Efficient solution route to high-performance oxide transistors. *Proceedings of the National Academy of Sciences*, 112(11):3217–3222, mar 2015.

[50] Hiromichi Godo, Daisuke Kawae, Shuhei Yoshitomi, Toshinari Sasaki, Shunichi Ito, Hiroki Ohara, Hideyuki Kishida, Masahiro Takahashi, Akiharu Miyanaga, and Shunpei Yamazaki. Temperature Dependence of Transistor Characteristics and Electronic Structure for Amorphous InGaZn-Oxide Thin Film Transistor. *Japanese Journal of Applied Physics*, 49(3):03CB04, mar 2010.

[51] Tze Ching Fung, Chiao Shun Chuang, Charlene Chen, Katsumi Abe, Robert Cottle, Mark Townsend, Hideya Kumomi, and Jerzy Kanicki. Two-dimensional numerical simulation of radio frequency sputter amorphous In-Ga-Zn-O thin-film transistors. *Journal of Applied Physics*, 106(8):1–10, 2009.

[52] Jong H. Na, M. Kitamura, and Y. Arakawa. High field-effect mobility amorphous InGaZnO transistors with aluminum electrodes. *Applied Physics Letters*, 93(6):063501, 2008.

[53] LJ van der PAUW. A method of measuring specific resistivity and Hall effect of discs of arbitrary shape. *Philips research ...*, pages 1–9, 1958.

[54] Ho-Hyun Nahm, Yong-Sung Kim, and Dae Hwan Kim. Instability of amorphous oxide semiconductors via carrier-mediated structural transition between disorder and peroxide state. *Physica Status Solidi (B)*, 249(6):1277–1281, jun 2012.

[55] Yongsik Kim, Sungchul Kim, Woojoon Kim, Minkyung Bae, Hyun Kwang Jeong, Dongsik Kong, Sunwoong Choi, Dong Myong Kim, and Dae Hwan Kim. Amorphous InGaZnO Thin-Film TransistorsPart II: Modeling and Simulation of Negative Bias Illumination Stress-Induced Instability. *IEEE Transactions on Electron Devices*, 59(10):2699–2706, oct 2012.

[56] Jeong-Min Lee, In-Tak Cho, Jong-Ho Lee, Woo-Seok Cheong, Chi-Sun Hwang, and Hyuck-In Kwon. Comparative study of electrical instabilities in top-gate InGaZnO thin film transistors with Al[sub 2]O[sub 3] and Al[sub 2]O[sub 3]/SiN[sub x] gate dielectrics. *Applied Physics Letters*, 94(22):222112, 2009.

[57] Sunghwan Lee, Brian Bierig, and David C. Paine. Amorphous structure and electrical performance of low-temperature annealed amorphous indium zinc oxide transparent thin film transistors. *Thin Solid Films*, 520(10):3764–3768, mar 2012.

[58] Tze Ching Fung, Chiao Shun Chuang, Kenji Nomura, Han Ping David Shieh, Hideo Hosono, and Jerzy Kanicki. Photofield effect in amorphous In-Ga-Zn-O (a-IGZO) thin film transistors. *Journal of Information Display*, 9(4):21–29, dec 2008.

[59] K Moazzami, T E Murphy, J D Phillips, M C-K Cheung, and a N Cartwright. Subbandgap photoconductivity in ZnO epilayers and extraction of trap density spectra. *Semiconductor Science and Technology*, 21(6):717–723, jun 2006.

[60] Kenji Nomura, Toshio Kamiya, Masahiro Hirano, and Hideo Hosono. Origins of threshold voltage shifts in room-temperature deposited and annealed a-In-Ga-Zn-O thin-film transistors. *Applied Physics Letters*, 95(1):2014–2017, 2009.

[61] Kenji Nomura, Toshio Kamiya, and Hideo Hosono. Stability and high-frequency operation of amorphous In-Ga-Zn-O thin-film transistors with various passivation layers. *Thin Solid Films*, 520(10):3778–3782, 2012.

[62] T. Mudgal, N. Walsh, R. G. Manley, and K. D. Hirschman. Impact of Annealing on Contact Formation and Stability of IGZO TFTs. *ECS Journal of Solid State Science and Technology*, 3(9):Q3032–Q3034, jul 2014.

[63] Kenji Nomura, Toshio Kamiya, Eiji Ikenaga, Hiroshi Yanagi, Keisuke Kobayashi, and Hideo Hosono. Depth analysis of subgap electronic states in amorphous oxide semiconductor, a-In-Ga-Zn-O, studied by hard x-ray photoelectron spectroscopy. *Journal of Applied Physics*, 109(7):073726, 2011.

[64] G. T. Kim, J. G. Park, Y. W. Park, C. Muller-Schwanneke, M. Wagenhals, and S. Roth. Nonswitching van der Pauw technique using two different modulating frequencies. *Review of Scientific Instruments*, 70(4):2177, 1999.

[65] Model SR830 DSP Lock-In Amplifier User's Manual. Technical Report 408, Stanford Research Systems, 2011.

[66] D ALMOND, G DUNCAN, and A WEST. The determination of hopping rates and carrier concentrations in ionic conductors by a new analysis of ac conductivity. *Solid State Ionics*, 8(2):159–164, apr 1983.

[67] Lars Onsager. Reciprocal relations in irreversible processes. I. *Physical Review*, 37(4):405–426, 1931.

[68] H. B G Casimir. On Onsager's principle of microscopic reversibility. *Reviews of Modern Physics*, 17(2-3):343–350, 1945.

[69] H. H. Sample, W. J. Bruno, S. B. Sample, and E. K. Sichel. Reverse-field reciprocity for conducting specimens in magnetic fields. *Journal of Applied Physics*, 61(3):1079, 1987.

[70] M. Buttiker. Symmetry of electrical conduction. *IBM Journal of Research and Development*, 32(3):317–334, 1988.

[71] Khashayar Ghaffarzadeh, Arokia Nathan, John Robertson, Sangwook Kim, Sanghun Jeon, Changjung Kim, U-In Chung, and Je-Hun Lee. Persistent photoconductivity in HfInZnO thin film transistors. *Applied Physics Letters*, 97(14):143510, 2010.

[72] Dong Hee Lee, Ken-ichi Kawamura, Kenji Nomura, Hiroshi Yanagi, Toshio Kamiya, Masahiro Hirano, and Hideo Hosono. Steady-state photoconductivity of amorphous InGaZnO. *Thin Solid Films*, 518(11):3000–3003, mar 2010.

[73] H. Rzewuski and Z. Werner. Differential method for Hall-coefficient measurements in an a.c. magnetic field. *Electronics Letters*, 1(4):86, 1965.

[74] J C Male. Hall effect measurement in semiconducting chalcogenide glasses and liquids. *British Journal of Applied Physics*, 18(11):1543–1549, nov 1967.

[75] Oki Gunawan, Yudistira Virgus, and Kong Fai Tai. A parallel dipole line system. *Applied Physics Letters*, 106(6), 2015.

[76] Jeffrey Lindemuth and Shin-Ichiro Mizuta. Hall measurements on low-mobility materials and high resistivity materials. In Louay A. Eldada, editor, *SPIE Solar Energy + Technology*, volume 8110, page 81100I, sep 2011.

[77] Blake L. Stevens, Cathleen A. Hoel, Carolyn Swanborg, Yang Tang, Chuanle Zhou, Matthew Grayson, Kenneth R. Poeppelmeier, and Scott a. Barnett. DC reactive magnetron sputtering, annealing, and characterization of CuAlO2 thin films. *Journal of Vacuum Science & Technology A: Vacuum, Surfaces, and Films*, 29(1):011018, 2011.

[78] John B. Goodenough and Kyu Sung Park. The Li-ion rechargeable battery: A perspective. *Journal of the American Chemical Society*, 135(4):1167–1176, 2013.

[79] Neelima Mahato, Amitava Banerjee, Alka Gupta, Shobit Omar, and Kantesh Balani. Progress in material selection for solid oxide fuel cell technology: A review. *Progress in Materials Science*, 72(February 2015):141–337, jul 2015.

[80] T. Kaneda and E. Mizuki. Hall Effect of Silver Ions in RbAg4I5 Single Crystals. *Physical Review Letters*, 29(14):937–939, oct 1972.

[81] Stephan D. Kim, Jiajun Luo, D. Bruce Buchholz, R. P. H. Chang, and M. Grayson. Modular time division multiplexer: Efficient simultaneous characterization of fast and slow transients in multiple samples. *Review of Scientific Instruments*, 2016.

[82] David Redfield and Richard H Bube. *Photoinduced Defects in Semiconductors*. Cambridge University Press, 1996.

[83] W. Shockley and W. T. Read. Statistics of the Recombinations of Holes and Electrons. *Physical Review*, 87(5):835–842, sep 1952.

[84] C Eiche, D Maier, M Schneider, D Sinerius, J Weese, K W Benz, and J Honerkamp. Analysis of photoinduced current transient spectroscopy (PICTS) data by a regularization method. *Journal of Physics: Condensed Matter*, 4(28):6131–6140, jul 1992.

[85] X Mathew. Photo-induced current transient spectroscopic study of the traps in CdTe. *Solar Energy Materials and Solar Cells*, 76(3):225–242, mar 2003.

[86] Jiajun Luo, Alexander U. Adler, Thomas O. Mason, D. Bruce Buchholz, R. P. H. Chang, and M. Grayson. Transient photoresponse in amorphous In-Ga-Zn-O thin films under stretched exponential analysis. *Journal of Applied Physics*, 113(15):153709, 2013.

[87] S. A. Studenikin, Nickolay Golego, and Michael Cocivera. Optical and electrical properties of undoped ZnO films grown by spray pyrolysis of zinc nitrate solution. *Journal of Applied Physics*, 83(4):2104, 1998.

[88] Takashi Nagase, Ko-hei Kishimoto, and Hiroyoshi Naito. High resolution measurement of localized-state distributions from transient photoconductivity in amorphous and polymeric semiconductors. *Journal of Applied Physics*, 86(9):5026, 1999.

[89] J. Kakalios, R. A. Street, and W. B. Jackson. Stretched-exponential relaxation arising from dispersive diffusion of hydrogen in amorphous silicon. *Physical Review Letters*, 59(9):1037–1040, aug 1987.

[90] D. C. Johnston. Stretched exponential relaxation arising from a continuous sum of exponential decays. *Physical Review B - Condensed Matter and Materials Physics*, 74(18):1–7, 2006.

[91] Reiner Zorn. Logarithmic moments of relaxation time distributions. *Journal of Chemical Physics*, 116(8):3204–3209, 2002.

[92] Jiajun Luo and Matthew Grayson. Continuous Multi-exponential Method for Analyzing Transient Photoconductivity in Amorphous Oxide Semiconductors. *MRS Proceedings*, 1731:mrsf14–1731–o08–04, apr 2015.

[93] A. Tsormpatzoglou, N. a. Hastas, M. K. Hatalis, and C. a. Dimitriadis. Analytical unified drain current model of amorphous IGZO thin film transistors considering a Gaussian distribution of tail states. In *2014 29th International Conference on Microelectronics Proceedings - MIEL 2014*, number Miel, pages 269–272. IEEE, may 2014.

[94] S. A. Studenikin, N Golego, and M Cocivera. Improved Laplace transform method to determine trap densities from transients: application to ZnO and films. *Semiconductor science and technology*, 13:1383, 1998.

[95] H. R. Park, J. Z. Liu, and S. Wagner. Saturation of the light-induced defect density in hydrogenated amorphous silicon. *Applied Physics Letters*, 55(25):2658, 1989.

[96] Md Delwar Hossain Chowdhury, Piero Migliorato, and Jin Jang. Temperature dependence of negative bias under illumination stress and recovery in amorphous indium gallium zinc oxide thin film transistors. *Applied Physics Letters*, 102(14):143506, 2013.

[97] A. J. Flewitt and M. J. Powell. A thermalization energy analysis of the threshold voltage shift in amorphous indium gallium zinc oxide thin film transistors under simultaneous negative gate bias and illumination. *Journal of Applied Physics*, 115(13):134501, 2014.

[98] K. J. Hollenbeck. INVLAP.M: A matlab function for numerical inversion of Laplace transforms by the de Hoog algorithm, 1998.

[99] Jiajun Luo and Matthew Grayson. Predictive and Descriptive Models for Transient Photoconductivity in Amorphous Oxide Semiconductors. *MRS Advances*, 2016.

[100] M. Stutzmann, W. B. Jackson, and C. C. Tsai. Light-induced metastable defects. *Physical Review B: Condensed Matter and Materials Physics*, 32(1):23–47, 1985.

[101] Te Chih Chen, Ting Chang Chang, Chih Tsung Tsai, Tien Yu Hsieh, Shih Ching Chen, Chia Sheng Lin, Ming Chin Hung, Chun Hao Tu, Jiun Jye Chang, and Po Lun Chen. Behaviors of InGaZnO thin film transistor under illuminated positive gate-bias stress. *Applied Physics Letters*, 97(2010), 2010.

[102] W. B. Jackson, M. Stutzmann, and C. C. Tsai. Electron-spin-resonance-transient spectroscopy. *Physical Review B*, 34(1):54–62, jul 1986.

[103] Kenneth F. Wallis. The Two-Piece Normal, Binormal, or Double Gaussian Distribution: Its Origin and Rediscoveries. *Statistical Science*, 29(1):106–112, feb 2014.

[104] M. C. Jones and M. J. Faddy. A skew extension of the t-distribution, with applications. *Journal of the Royal Statistical Society: Series B (Statistical Methodology)*, 65(1):159–174, feb 2003.

[105] R Kohlrausch. Theorie des elektrischen Rückstandes in der Leidener Flasche. *Annalen der Physik und Chemie*, 167(2):179–214, 1854.

[106] F Kohlrausch. Ueber die elastische Nachwirkung bei der Torsion. *Annalen der Physik*, 195(7):337–368, 1863.

[107] Graham Williams and David C. Watts. Non-symmetrical dielectric relaxation behaviour arising from a simple empirical decay function. *Transactions of the Faraday Society*, 66(1):80, 1970.

[108] M. Berberan-Santos, E. N. Bodunov, and B. Valeur. History of the Kohlrausch (stretched exponential) function: Pioneering work in luminescence. *Annalen der Physik (Leipzig)*, 17(7):460–461, 2008.

[109] R. G. Palmer, D. L. Stein, E. Abrahams, and P. W. Anderson. Models of Hierarchically Constrained Dynamics for Glassy Relaxation. *Physical Review Letters*, 53(10):958–961, sep 1984.

[110] Richard H. Bube, Lisa Echeverria, and David Redfield. Evidence for a stretched-exponential description of optical defect generation in hydrogenated amorphous silicon. *Applied Physics Letters*, 57(1):79, 1990.

[111] Jeong-Min Lee, In-Tak Cho, Jong-Ho Lee, and Hyuck-In Kwon. Bias-stress-induced stretched-exponential time dependence of threshold voltage shift in InGaZnO thin film transistors. *Applied Physics Letters*, 93(9):093504, 2008.

[112] Marco Raberto, Enrico Scalas, and Francesco Mainardi. Waiting-times and returns in high-frequency financial data: An empirical study. *Physica A: Statistical Mechanics and its Applications*, 314(1-4):749–755, 2002.

[113] M. Stutzmann, W. B. Jackson, and C. C. Tsai. Annealing of metastable defects in hydrogenated amorphous silicon. *Physical Review B*, 34(1):63–72, jul 1986.

[114] S. Deane, R. Wehrspohn, and M. Powell. Unification of the time and temperature dependence of dangling-bond-defect creation and removal in amorphous-silicon thin-film transistors. *Physical Review B*, 58(19):12625–12628, 1998.

[115] M F Shlesinger and E W Montroll. On the Williams-Watts function of dielectric relaxation. *Proceedings of the National Academy of Sciences of the United States of America*, 81(4):1280–3, 1984.

[116] EW Montroll and GH Weiss. Random walks on lattices. II. *Journal of Mathematical Physics*, 6(May 2016):167, 1965.

[117] Ralf Metzler and Joseph Klafter. The random walk's guide to anomalous diffusion: a fractional dynamics approach. *Physics Reports*, 339(1):1–77, dec 2000.

[118] Michael F Shlesinger. Fractal Time in Condensed Matter. *Annual Review of Physical Chemistry*, 39(1):269–290, oct 1988.

[119] P. Bordewijk. Defect-diffusion models of dielectric relaxation. *Chemical Physics Letters*, 32(3):592–596, 1975.

[120] John T. Bendler and Michael F. Shlesinger. Defect-diffusion models of relaxation. *Journal of Molecular Liquids*, 36(C):37–46, sep 1987.

[121] Stephen Richard Elliott. *Physics of amorphous materials*. Longman Scientific & Technical, 1984.

[122] Kazuo Morigaki. Microscopic Mechanism for the Photo-Creation of Dangling Bonds in a-Si:H. *Japanese Journal of Applied Physics*, 27(Part 1, No. 2):163–168, feb 1988.

[123] Shinhyuk Yang, Doo-Hee Cho, Min Ki Ryu, Sang-Hee Ko Park, Chi-Sun Hwang, Jin Jang, and Jae Kyeong Jeong. Improvement in the photon-induced bias stability of AlSnZnInO thin film transistors by adopting AlO[sub x] passivation layer. *Applied Physics Letters*, 96(21):213511, 2010.

[124] Kwang Hee Lee, Ji Sim Jung, Kyoung Seok Son, Joon Seok Park, Tae Sang Kim, Rino Choi, Jae Kyeong Jeong, Jang Yeon Kwon, Bonwon Koo, and Sangyun Lee.

The effect of moisture on the photon-enhanced negative bias thermal instability in Ga-In-Zn-O thin film transistors. *Applied Physics Letters*, 95(23), 2009.

[125] Yoon Jang Chung, Jeong Hwan Kim, Un Ki Kim, Deok-Yong Cho, Hyung Suk Jung, Jae Kyeong Jeong, and Cheol Seong Hwang. Direct Observation of Hole Current in Amorphous Oxide Semiconductors under Illumination. *Electrochemical and Solid-State Letters*, 14(6):G35, 2011.

[126] Byungki Ryu, Hyeon-Kyun Noh, Eun-Ae Choi, and K. J. Chang. O-vacancy as the origin of negative bias illumination stress instability in amorphous InGaZnO thin film transistors. *Applied Physics Letters*, 97(2):022108, 2010.

[127] Julia Medvedeva. unpublished work, 2016.

[128] Rabi Khanal, D. Bruce Buchholz, Robert P. H. Chang, and Julia E. Medvedeva. Composition-dependent structural and transport properties of amorphous transparent conducting oxides. *Physical Review B*, 91(20):205203, may 2015.

APPENDIX A

Circuit schematic of a MTDM unit

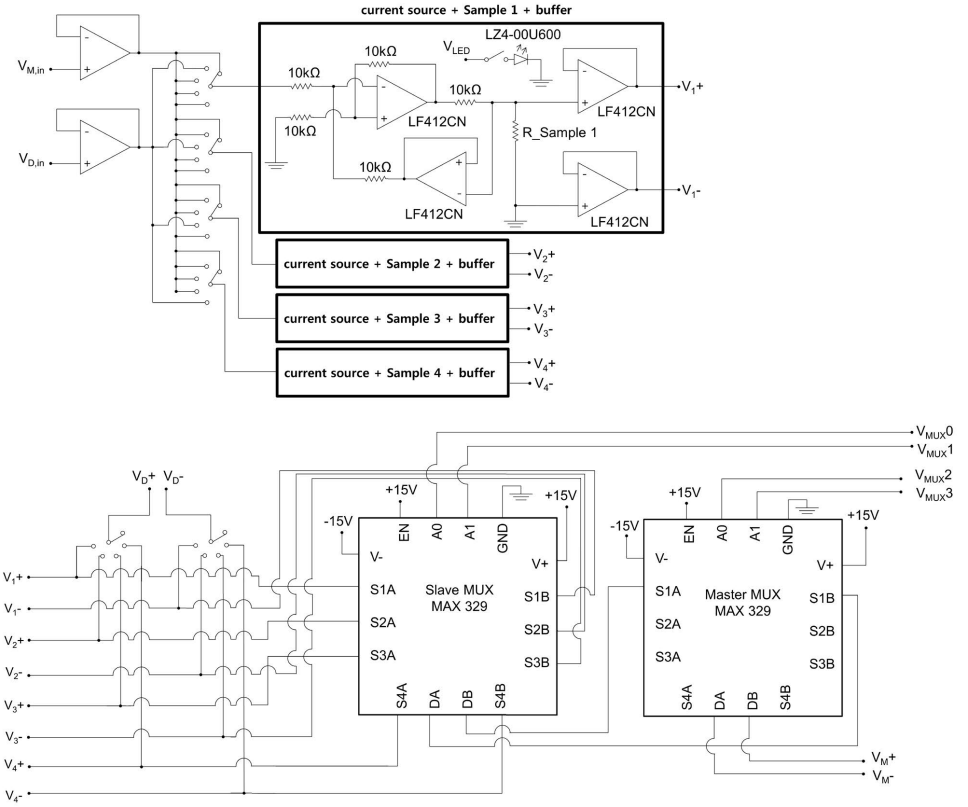

Figure A.1. The circuit schematic of a MTDM unit for measuring the transient photoconductivity of a-IGZO samples. $V_{D;in}$ and $V_{M;in}$ are voltage inputs to the current sources for the dedicated mode and the multiplexed mode, respectively. The difference between V_D+ and V_D- is the four-point voltage across the sample that is being measured in the dedicated mode. The difference between V_M+ and V_M- is the voltage across the sample in the multiplexed mode that is indexed by the two multiplexers. A computer program written in Python indexes the multiplexers using pins $V_{\mathrm{MUX}}0$ through $V_{\mathrm{MUX}}3$.

Vita

NAME: Jiajun Luo

BORN: Xi'an, Shaanxi, China

EDUCATION:

- Ph.D. in Electrical Engineering, Dept. of EECS, Northwestern University, Evanston, IL. Dec, 2016
- Bachelor of Science, Dept. of Microelectronics, Peking University, Beijing, China. July, 2009

PUBLICATIONS:

(1) M. Grayson and J. Luo, "System and Method for Electrical Characterization", US Patent pending

(2) J. Luo and M. Grayson, "Predictive and Descriptive Models for Transient Photoconductivity in Amorphous Oxide Semiconductors", *MRS Advances* (2016)

(3) S.D. Kim, J. Luo, D.B. Buchholz, R.P.H. Chang, and M. Grayson, "Modular time division multiplexer: Efficient simultaneous characterization of fast and slow transients in multiple samples", *Review of Scientific Instruments* 87, 093904 (2016)

(4) J. Luo and M. Grayson, "Continuous Multi-exponential Method for Analyzing Transient Photoconductivity in Amorphous Oxide Semiconductors", *MRS Proceedings* 1731 (2015)

(5) J. Luo, A.U. Adler, T.O. Mason, D.B. Buchholz, R.P.H. Chang, and M. Grayson, "Transient photoresponse in amorphous In-Ga-Zn-O thin films under stretched exponential analysis", *Journal of Applied Physics* 113, 153709 (2013)

(6) D.J. Late, B. Liu, J. Luo, A. Yan, H.S.S.R. Matte, M. Grayson, C.N.R. Rao, and V.P. Dravid, "GaS and GaSe ultrathin layer transistors", *Advanced Materials* 24, 3549 (2012)

(7) J. Luo, D. Late, I. Wu, K. Biswas, M. Kanatzidis, and M. Grayson, "Preparation of Exfoliated Bi_2Te_3 Thin Films", *AIP Conf. Proc.* 1416, 135 (2011)